

Ocean Breath: Origin, Transport and Fate of Anthropogenic Carbon and Oxygen in the Ocean

Xabier Dávila Rodríguez

Thesis for the degree of Philosophiae Doctor (PhD)
University of Bergen, Norway
2023

UNIVERSITY OF BERGEN



Ocean Breath: Origin, Transport and Fate of Anthropogenic Carbon and Oxygen in the Ocean

Xabier Dávila Rodríguez



Thesis for the degree of Philosophiae Doctor (PhD)
at the University of Bergen

Date of defense: 25.08.2023

© Copyright Xabier Dávila Rodríguez

The material in this publication is covered by the provisions of the Copyright Act.

Year: 2023

Title: Ocean Breath: Origin, Transport and Fate of Anthropogenic Carbon and Oxygen in the Ocean

Name: Xabier Dávila Rodríguez

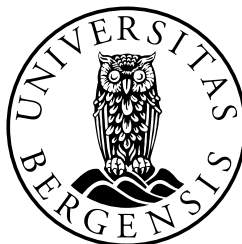
Print: Skipnes Kommunikasjon / University of Bergen

Preface

This study is carried out at the Geophysical Institute, University of Bergen, where I have been part of the Biogeochemistry group. Additionally, I have been affiliated with the Carbon research group at the Bjerknes Centre for Climate Research. A part of the work presented here has been carried out at Woods Hole Oceanographic Institution (WHOI) where Dr. Geoffrey (Jake) Gebbie kindly hosted me for several short visits. These visits were supported by the Ocean Outlook Bergen-WHOI collaboration and by the Meltzer Research Fund. I also had the opportunity to participate in an oceanographic cruise in May 2019 on board RV "Johan Hjort" which provided me with relevant insights into transient tracer data collection. I have been enrolled in the Research School on Changing Climates in the Coupled Earth System (CHESS), which provided a valuable experience and network through many relevant and exciting short courses, meetings and summer schools. Some of the invaluable experiences through my Ph.D. are the Advanced Climate Dynamics Course (ACDC) on the "Anthropocene" in Yosemite in 2019, the Climate Action field course on board the Statsraad Lehmkuhl tall ship across the Caribbean Sea in 2021, the Bornö Summer School (BOSS) on Ocean Biogeochemistry on "Grand Challenges in a Warming World" at Bornö Marine Research Station in 2022, and the Surface Ocean Lower Atmosphere Study (SOLAS) Summer School in Cape Verde in 2023. Prior to my Ph.D., many of these experiences were more fantasy than reality.



Research school on changing climates in the coupled earth system



Acknowledgements

I am deeply grateful to everyone who collaborated to make this thesis possible. First and foremost, I would like to thank my main supervisor, Are. Thank you for your patience, confidence, and the freedom you provided me to pursue my own ideas that shaped me as a researcher. Your guidance and mentorship have been invaluable, and I am grateful for what I have learned under your supervision. I am also thankful that you let me attend every summer school I could find. I thoroughly enjoyed this journey.

I would also like to extend my gratitude to my co-supervisors. Siv, thank you for your support, insightful feedback, and for actively introducing me to your network and colleagues at the Ocean Sciences meeting in San Diego. Jake, I am truly grateful for your hospitality during my time at WHOI, for patience in guiding me through the maths involved in the TMI, and for answering all my questions, even the silly ones. Elaine, thank you for your valuable suggestions and insights during this journey. I am looking forward to embarking on our next project. I would also like to acknowledge my co-authors for their invaluable feedback and collaborative efforts, with a special mention to Ailin. Thank you for helping me get started with the TMI and for sharing the enthusiasm (and frustrations) regarding this method.

My gratitude extends to the extraordinary research and PhD community at GFI and Bjerkens Centre. To all the wonderful friends I have made during these past four years, who have transformed Bergen into a place I call home, I am eternally thankful. Jakob, Anais, Laura, Artem, Sonja, Ines, Etienne, Helene, Elina, Vår, Morven, Filippa, Rike, Paul, Kristine, Johanne, Danielle, Anna, Karita, and many others - thank you for being a constant source of inspiration, support, and joy. Last but certainly not least, I would like to express my deepest appreciation to my family. Ama, Aita, and Izaskun, thank you for your unconditional love and support in my pursuit of a career, even when it meant being far from home. *Zuengatik, zuentzat.*

Xabier Dávila Rodríguez
Bergen, May 2023

*Open your mouth wide
A universal sigh
And while the ocean blooms
It's what keeps me alive*

Bloom; Radiohead

Abstract

Ongoing climate change is changing the way that the atmosphere and the ocean exchange energy and properties by reducing ocean ventilation. Changes in ventilation are expected to have important feedbacks in the climate system by reducing the uptake of anthropogenic carbon (C_{ant}) and by decreasing the oxygen supply to the interior ocean, which will impact important biogeochemical processes in regions already depleted of oxygen. In this dissertation, the Total Matrix Inter-comparison (TMI) observation-based transport matrix is used to show how ocean circulation shapes the interior distribution of C_{ant} and oxygen. Specifically, the TMI is used to investigate the mixed layer origin, transport along pathways, and fate of C_{ant} and oxygen in the ocean. The results presented highlight the importance of high latitude mode and deep waters, with a special focus on the Nordic Seas, and are distributed in three papers.

Paper I investigates how the ocean is filled with C_{ant} , which is the carbon that has been added to the ocean as a result of human activities. While the size of this reservoir is well constrained by different methods, the fluxes across the mixed layer that result in such a reservoir are not, despite being the bottleneck for the uptake. The paper estimates the fluxes of C_{ant} across the mixed layer using the global version of the TMI transport matrix. Here, the TMI is combined with an already published time-evolving boundary condition of C_{ant} to reproduce and trace back the current inventory to the region of subduction in the mixed layer. The results show that most of the C_{ant} stored below the mixed layer is injected in the subtropics and the Southern Ocean, while the largest fluxes occur in the Sub-polar North Atlantic. The paper emphasizes the important role of a few oceanic regions for filling the ocean C_{ant} reservoir.

Paper II investigates the origins of open ocean Oxygen Minimum Zones (OMZs). OMZs are regions depleted in oxygen, and are projected to expand under the current ocean deoxygenation, thus threatening marine life and affecting carbon and nitrogen cycles. The paper benefits from the information implicit in the TMI, to determine the origins of OMZs in terms of OMZ volume, oxygen that survives remineralization and oxygenates OMZs, and oxygen utilization in the interior ocean that contributes to the oxygen-deficit in the OMZs. The results show that OMZs are mostly filled with waters from high-latitudes at millennial timescales, but these waters contribute little to the oxygenation of the OMZs, as most of the oxygen has been utilized upon arrival. Instead, oxygen is mostly supplied by tropical, subtropical and intermediate waters originating from adjacent

regions. This study also determines where the utilization of oxygen occurs along the pathways from water mass formation regions to the OMZs, which we refer to as oxygen "remineralization pathways". These pathways show that less than a third of the oxygen-deficit accumulated in OMZs originates within the OMZs. The paper suggests that, in steady-state, OMZs are primarily set by ocean circulation pathways that bring deep and old waters with relatively low oxygen, from high latitudes into the OMZs.

Paper III investigates the ventilation timescales of the Nordic Seas, which is a key region for ocean circulation and climate. In this paper, water mass mean ages derived from observations of CFC-12 are assimilated into an existing high-resolution version of the TMI for the Nordic Seas. The results show that the upper and intermediate Nordic Seas are ventilated on very short timescales, with half of the mixed layer waters being fluxed out of the Nordic Seas after 5 years. The deeper parts of the Nordic Seas, however, are isolated from the mixed-layer waters, indicating that the deep waters in the Nordic Seas are not ventilated in the Nordic Seas. The paper provides a new method to investigate the ventilation of the Nordic Seas, which will eventually allow to estimate the ocean uptake of heat, carbon, and oxygen.

Combined, the three papers highlight the global connection of the world ocean through the transformation and transport of water masses and their biogeochemical properties at different spatial and temporal timescales. They show the importance of ocean circulation and high latitude mode and deep water formation regions for the uptake and distribution of C_{ant} and oxygen. In addition, a step forward is taken in the use of regional data-based transport matrices to provide a more detailed representation of those processes that exert a global impact on climate.

Sammendrag

Menneskeskapte klimaendringer endrer måten atmosfæren og havet utveksler energi og egenskaper på ved å redusere havventilasjonen. Endringer i ventilasjonen antas å være en viktig tilbakekoblingsmekanisme i klimasystemet ved å redusere opptaket av antropogen karbon (C_{ant}) eller ved å redusere oksygentilførselen til dyphavet, noe som vil påvirke biogeokjemiske prosesser i områder som allerede er utarmet for oksygen. I denne avhandlingen brukes en Total Matrix Intercomparison (TMI) observasjonsbasert transportmatrise for å vise hvordan havsirkulasjonen påvirker fordelingen av C_{ant} og oksygen i havet. TMI-metoden blir brukt til å undersøke blandalagets opprinnelse samt transport av C_{ant} og oksygen i havet. Resultatene presenteres i tre artikler, og fremhever betydningen av dypvannsdannelse på høye breddegrader med spesielt fokus på Norskehavet.

Artikkel I undersøker hvordan havet fylles opp med C_{ant} , som er karbonet som ender opp i havet som et resultat av CO_2 -utslipp fra menneskelig aktivitet. Mens størrelsen på dette reservoaret er godt kjent fra forskjellige metoder, er fluksene gjennom blandalagsdypet som resulterer i et slikt reservoar dårligere forstått. Artikkelen beregner fluksene av C_{ant} gjennom blandalaget ved hjelp av den globale versjonen av TMI-matrisen, kombinert med en tidligere publisert tidsserie av C_{ant} i overflatehavet. Dermed er det mulig å spore C_{ant} -innholdet i havet tilbake til blandalaget i regioner med konveksjon og/eller dypvannsdannelse. Resultatene viser at det meste av C_{ant} som lagres under blandalaget blir injisert i subtropene og i Sørishavet, mens de største fluksene forekommer i subpolare strøk i Nord-Atlanteren. Artikkelen viser at bidragene fra noen få havregioner fyller mesteparten av havets C_{ant} -reservoar.

Artikkel II undersøker opprinnelsen til oksygenminimumsonene (OMZ) i åpent hav som allerede er utarmet for oksygen, og som under nåværende deoksygenering av havet vil true marint liv og påvirke karbon- og nitrogen-syklusene. Artikkelen drar nytte av informasjonen som ligger implisitt i TMI for å bestemme opprinnelsen til OMZ i form av volum, oksygen som overlever remineralisering og oksygenerer OMZ, og oksygenbruk i dyphavet som bidrar til oksygenunderskuddet i OMZ. Resultatene viser at OMZ for det meste fylles av vann som stammer fra høye breddegrader over lange tidsskalaer, men disse vannmassene bidrar lite til oksygenering av OMZ da det meste av oksygenet er brukt opp ved ankomst. I stedet blir oksygen hovedsakelig levert av tropiske, subtropiske, og intermediære vannmasser som stammer fra tilstøtende regioner. Artikkelen viser også hvor oksygenet brukes på veien fra områder med vannmassetransformasjon til OMZ.

Vi refererer til dette som "remineraliseringsbaner". Disse banene viser at mindre enn en tredjedel av oksygenunderskuddet har opprinnelse innenfor OMZene. Artikkelen antyder at OMZ i en stabil tilstand i hovedsak blir satt av havsirkulasjonen som bringer dypt og gammelt vann med relativt lavt oksygen fra høye breddegrader inn i OMZ.

Artikkel III undersøker ventilasjonstidsrammene i De nordiske hav, som er en nøkkelregion for havsirkulasjon og klima. Artikkelen assimilerer gjennomsnittsalderen til vannmassene - utledet fra observasjoner av CFC-12 - inn i en eksisterende regional versjon av TMI for De nordiske hav som har mye høyere romlig oppløsning enn den globale versjonen. Resultatene viser at øvre og intermedieære deler av De nordiske hav ventileres på svært korte tidsskalaer, der halvparten av vannmassene i blandalaget strømmer ut av regionen etter 5 år. De dypere delene av De nordiske hav er derimot isolert fra vannmassene i blandalaget, noe som indikerer at de dype vannmassene i regionen ventileres langt unna. Artikkelen er et eksempel på en ny metode for å undersøke ventilasjonen i De nordiske hav på. Metoden vil også kunne brukes til å bestemme opptak og fordeling av varme, karbon, og oksygen i regionen.

Samlet fremhever de tre artikkene den globale forbindelsen i verdenshavene gjennom transport av vannmasser på forskjellige romlige og tidsmessige skalaer. De viser betydningen av havsirkulasjon, og spesielt områder hvor dypvann dannes, for opptak og fordeling av *Ca* og oksygen. I tillegg tas det et skritt videre i bruken av regionale data-baserte transportmatriser for å gi en mer detaljert representasjon av lokale og regionale prosesser som utøver en global påvirkning på klimaet.

Outline

This thesis consists of an introductory part and three scientific papers. Chapter 1 presents the motivation and objectives behind the realization of this thesis. Chapter 2 gives an introduction to the scientific background for the results presented and the data and methods are described in Chapter 3. Chapter 4 gives a summary of the scientific paper and a synthesis and some future perspectives are provided in Chapter 5. The scientific papers listed below are provided in Chapter 6.

List of papers

1. Xabier Davila, Geoffrey Gebbie, Ailin Brakstad, Siv K. Lauvset, Elaine L. McDonagh, Jörg Schwinger, and Are Olsen (2022) *How is the Ocean Anthropogenic Carbon Reservoir Filled?*, *Global Biogeochemical Cycles* **36**.
2. Xabier Davila, Are Olsen, Siv K. Lauvset, Elaine L. McDonagh, Ailin Brakstad and Geoffrey Gebbie (in review), *On the Origins of Open Ocean Oxygen Minimum Zones*, *Journal of Geophysical Research: Oceans*.
3. Xabier Davila, Geoffrey Gebbie, Ailin Brakstad, Siv K. Lauvset, Elaine L. McDonagh, Emil Jeansson and Are Olsen (in prep.), *Water-mass ages and ventilation timescales of the Nordic Seas inferred from transient tracers*.

Additional contributions not included in this thesis

- a) Elaine McDonagh, Nadine Goris, Agustin Kessler, Peter Brown, Xabier Davila, Yanchun He, Helene Langehaug, Emil Jeansson, Ulysses Ninnemann, Are Olsen, Richard Sanders, Jörg Schwinger and Jerry Tjiputra (in prep.), *AMOC constraint on North Atlantic Biogeochemistry*.

Contents

Preface	i
Acknowledgements	iii
Abstract	v
Sammendrag	vii
Outline	ix
1 Motivation	1
1.1 Objectives and scientific questions	4
2 Introduction	5
2.1 A brief history of water mass analysis	5
2.2 Ocean uptake of anthropogenic carbon	8
2.2.1 Seawater CO ₂ chemistry	9
2.2.2 Inventories, transport and fluxes	10
2.3 Ocean deoxygenation	12
2.3.1 Sources and sinks	12
2.3.2 Open ocean Oxygen Minimum Zones	15
3 Data and methods	19
3.1 Total Matrix Intercomparison (TMI)	19
3.2 Constraining ventilation rates in the Nordic Seas	21
3.2.1 Water-mass mean ages	22
4 Summary of the papers	25
5 Synthesis	29
5.1 Synergy between papers	29
5.2 Outlook	30
5.2.1 Challenges and opportunities	30
5.2.2 Long-term perspective	32
6 Scientific results	33
Paper I	35
Paper II	59
Paper III	97

Chapter 1

Motivation

As a result of the anthropogenic emissions from fossil fuel burning, cement production and land-use changes, the atmospheric CO₂ concentration increased from approximately 277 parts per million (ppm; *Joos and Spahni, 2008*) at the beginning of the industrial era to 414.71 ± 0.1 ppm in 2021 (*Friedlingstein et al., 2022*). The excess of CO₂ has changed the radiative properties of the atmosphere and resulted in a climate crisis. The Earth is warming, and its climate is changing. Many of the observed changes are unprecedented in thousands, if not hundreds of thousands of years, and are irreversible over hundreds or thousands of years. These changes in the climate system already have or are projected to have, profound global environmental, socio-economical, and political impacts (*IPCC, 2021*).

The ocean plays a critical role in regulating climate and has mitigated a large part of the warming by taking up a large part of the excess heat and CO₂ from the atmosphere. In particular, about 90% of the heat generated by the enhanced greenhouse effect has been taken up by the ocean (*Durack et al., 2018*) and about 25% of the excess CO₂ (*McNeil et al., 2003; Sabine et al., 2004; Khatiwala et al., 2009; DeVries, 2014*). This buffering of the climate crisis by the ocean, however, comes with a toll. The ocean is stratifying and losing breath. Ocean stratification is increasing as most of the heat uptake occurs in the upper ocean, which together with the increase in the freshwater input by melting glaciers and ice sheets, increases the density differences between the upper and interior ocean (*Yamaguchi and Suga, 2019; Durack et al., 2018; Li et al., 2020*). As a result, ocean ventilation, -i.e., the exchange between the surface and deep water masses, is reduced (*De Lavergne et al., 2014*). A reduction in ocean ventilation implies a weaker uptake of anthropogenic carbon, and a decrease in the interior ocean oxygen content (*Keeling et al., 2010*). Both of these processes have the potential to act as positive feedbacks on climate change and global warming. To which extent these processes will affect the climate system is to a large extent determined by the transport from the upper ocean to the interior ocean.

The transport of carbon from the surface ocean where it is absorbed, to the interior ocean where it is stored, is the rate-limiting step for the uptake of anthropogenic carbon by the ocean (*Sarmiento et al., 1992*). The volume and storage capacity of the mixed layer is small and it would quickly saturate with anthro-

pogenic carbon if there was no mixing. The subduction of waters from the mixed layer to the interior removes waters rich in anthropogenic carbon from the surface and replaces them with waters that have not been exposed to the current atmosphere and therefore with capacity for further anthropogenic carbon uptake. Therefore, the pathways that transport the carbon into and through the interior ocean define both the air-sea exchange and the interior distribution. While this transport is uncertain, both the air-sea exchange and interior distributions are relatively well constrained by high-quality observations from the past decades. The Surface Ocean CO₂ Atlas (SOCAT) network has provided observations of the surface ocean CO₂ partial pressure ([Bakker et al., 2016](#)), which have been used to constrain the ocean sink of atmospheric CO₂ ($2.9 \pm 0.4 \text{ Pg C yr}^{-1}$ for 2022), contributing to vital works such as the Global Carbon Budgets ([Friedlingstein et al., 2022](#)). While surface measurements are integrated by SOCAT, the interior ocean carbon measurements are integrated by the Global Ocean Data Analysis Project (GLODAP) which collects interior ocean observations from ship measurements of different biogeochemical variables ([Lauvset et al., 2022](#)). GLODAP has been extensively used to estimate the inventory and interior distribution of the carbon taken up by the ocean (e.g., [Lauvset et al., 2016](#); [Gruber et al., 2019](#)). Several studies and methods converge on a similar distribution and size of the inventory of anthropogenic carbon - i.e., the carbon that the ocean has taken up due to the anthropogenic emissions (Figure 1.1; [Sabine et al., 2004](#); [Khatiwala et al., 2009](#); [DeVries, 2014](#)), about $175 \pm 35 \text{ Pg C}$ for the year 2021 ([Friedlingstein et al., 2022](#)).

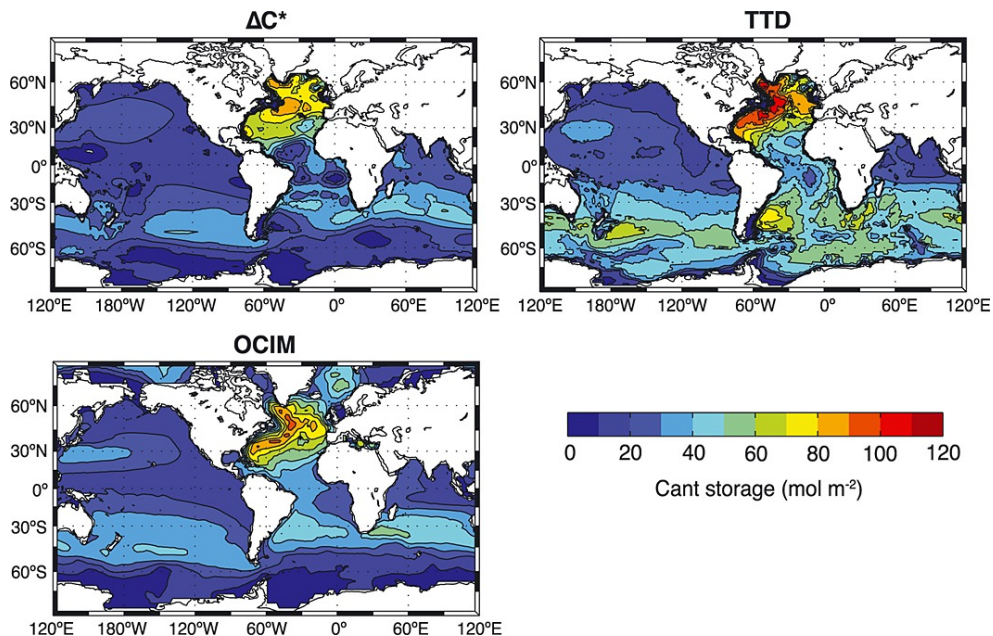


Figure 1.1: Anthropogenic carbon inventory constrained by different methods: The ΔC^* method by [Sabine et al. \(2004\)](#), the TTD method by [Waugh et al. \(2006\)](#) and the OCIM method by [DeVries \(2014\)](#). Figure from [DeVries \(2014\)](#).

Similarly, systematic dissolved oxygen measurements have allowed us to detect trends in the interior ocean oxygen content (Figure 1.2). The global oxygen content has declined by more than 2% since the 1960s (*Schmidtke et al., 2017*). Such trends are related to changes in oxygen solubility, supply, and demand. The solubility of oxygen is affected by temperature, the warmer the ocean, the less oxygen is dissolved into it. Only 15% of the observed deoxygenation, however, is explained by warming of the mixed-layer (*Helm et al., 2011*), therefore most of the deoxygenation is either driven by changes in ocean ventilation that supply oxygen to the interior or by changes in the demand, which is dictated by the remineralization of organic matter, or a combination of both (*Ito et al., 2016*). The Oxygen Minimum Zones (OMZs) are particularly sensitive to deoxygenation (Figure 1.2). These regions, already depleted in oxygen, are expanding (*Stramma et al., 2010; Zhou et al., 2022*). The oxygen concentration is so low in these regions that they are effectively "dead zones" for many higher trophic level animals such as fish and crustaceans (*Gray et al., 2002*). Additionally, OMZs are also a source of nitrous oxide, a powerful greenhouse gas (*Smethie, 1987*). At low oxygen concentrations, nitrate is the most thermodynamically favourable electron acceptor and is therefore reduced to nitrogen gas, a process called denitrification. Incomplete denitrification leads to the production and release of nitrous oxide. As such, The expansion of OMZs is a potential positive feedback for global warming (*Keeling et al., 2010*).

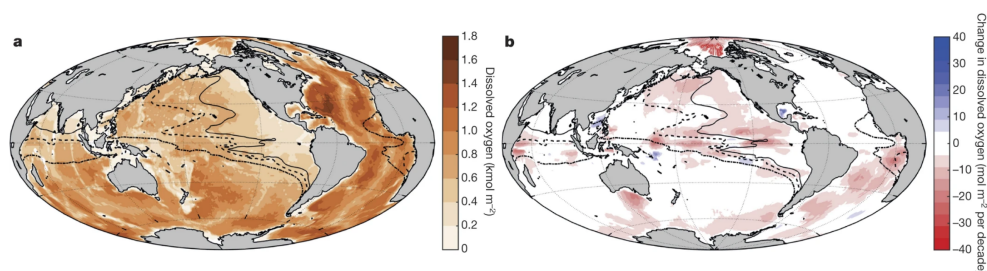


Figure 1.2: Amount of dissolved oxygen in the ocean and changes per decade since 1960. a) Global oxygen inventory (dissolved oxygen, colour coded). Lines indicate boundaries of Oxygen Minimum Zones (OMZs): dashed-dotted, regions with less than $80 \mu\text{mol kg}^{-1}$ oxygen anywhere within the water column; dashed lines and solid lines similarly represent regions with less than $40 \mu\text{mol kg}^{-1}$ oxygen and $20 \mu\text{mol kg}^{-1}$ oxygen, respectively. b) Change in dissolved oxygen per decade (colour coded). Lines show OMZs as in a). Figure from *Schmidtke et al. (2017)*.

The transport of oxygen and carbon from surface into and throughout the interior ocean is the key connection between the atmosphere and the ocean. High latitudes, such as the Southern Ocean and Subpolar North Atlantic, are the primary regions that ventilate the interior ocean (*Primeau et al., 2013; Keller et al., 2016; Holzer, 2022; Jeansson et al., 2011; Palter and Trossman, 2018*). These regions are therefore critical for the uptake, transport, and distribution of oxygen and anthropogenic carbon. However, neither the carbon and oxygen fluxes across the mixed layer nor the transport timescales throughout the interior oceans, are known. The main objective of this thesis is to constrain these.

1.1 Objectives and scientific questions

In this thesis, I determined the mixed-layer origin of anthropogenic carbon and oxygen in the world ocean, their fate in the interior ocean, and the associated transport timescales. Because high latitudes exert a global impact, I took a closer look into the ventilation timescales in the Nordic Seas. During the completion of this thesis, the following two main objectives and related research questions were raised:

1. Quantify the global anthropogenic carbon fluxes across the mixed layer.
 - a) What are the regions that contribute to the interior ocean inventory of anthropogenic carbon, and at what timescales?
 - b) What are the most efficient regions in taking up and transporting away anthropogenic carbon?
2. Determine the origin of the oxygen-deficit in open ocean Oxygen Minimum Zones.
 - a) What are the regions that contribute to the Oxygen Minimum Zone volume, oxygen and oxygen-deficit, and at what timescales?
 - b) How much of the oxygen-deficit in Oxygen Minimum Zones originates inside OMZs versus along the seawater pathways from the mixed layer?
3. Constrain the water-mass ages and ventilation timescales in the Nordic Seas.
 - a) What is the water mass age distribution in the Nordic Seas?
 - b) For how long does the mixed-layer water remain in the Nordic Seas?

Chapter 2

Introduction

The ocean plays a critical role in climate, absorbing a quarter of our emissions of carbon dioxide (CO_2) to the atmosphere as well as ninety per cent of the heat resulting from the greenhouse effect, thus buffering the warming effect of climate change. However, this service comes with a toll, the ocean is warming, acidifying, and deoxygenating. The exchange of heat and gas is not uniformly distributed across the ocean surface but is enhanced in water formation regions where large quantities of water are subducted from the mixed layer and into the interior ocean. This chapter introduces the dominant role of high latitude waters on climate and how the observation and analysis of ocean water-mass properties have historically helped to determine this role (Section 2.1), it also describes the processes that regulate the ocean uptake of carbon and its distribution (Section 2.2), as well as the processes that determine the ocean oxygen distribution and deoxygenation, with a special focus on open ocean Oxygen Minimum Zones (Section 2.3).

2.1 A brief history of water mass analysis

Modern oceanography is considered to have been conceived with the great British deep-sea expedition on board H.M.S *Challenger* in 1873-1876. Physico-chemical, bathymetric, geological and biological measurements were carried out across the Atlantic, Pacific and Indian Oceans under the scientific leadership of Sir Wyville Thomson, laying the foundations of our current knowledge of the oceans. Subsequently, in 1893-1896 Fridtjof Nansen set sail to the Arctic Ocean during the *Fram* expedition, observing the relatively warm and saline subsurface North Atlantic waters spreading into the great depths of the North Polar Basin ([Wüst, 1964](#)). During this period, F. Nansen and Bjørn Helland-Hansen emphasized the importance of accurate measurements of temperature and salinity, contributing to the design of essential instrumentation that constitutes the basis of today's oceanography, such as the Nansen Bottles and reversing thermometers. In 1916, due to the improvements in the accuracy of observations, B. Helland-Hansen presented a new method based on the correlation between temperature and salinity. This method would thereafter be known as T-S diagram. He argued that there is a relation between temperature and salinity, and by plotting them against each other, the T-S points generally fall on a well-defined curve. The deviations from a

T-S curve could then provide interesting information about the changes in temperature and salt concentration to which the water has been exposed. He suggested that maps of the distributions of such deviations can provide more valuable information about the formation and distribution of water masses than the usual hydrographic maps can provide (*Helland-Hansen, 1916*). This publication from B. Helland-Hansen makes him the pioneer of a method that thereafter would evolve and be known as water mass analysis.

The earliest recorded measurement of deep ocean temperature predates the *Challenger* and was made by trading ships, dating back to 1750. These measurements showed that colder waters exist below the warmer surface in tropical regions and inspired the idea that surface waters sink into the interior ocean while they retain their distinctive temperature. In 1798, *Rumford (1798)* who was born American, knighted by the British, and governor of Bavaria, postulated that such cold waters must originate in the north and south polar regions and spread through the sea bottom towards the equator, with surface currents flowing in the opposite direction (*Richardson, 2008*). This early conception of an overturning circulation, at that time mostly conceptual, matured in the 19th century as modern oceanography provided enough measurements for the first schematics of the meridional overturning circulation to be drawn (*Richardson, 2008*). A key example is Georg Wüst, who based on the *Meteor* expedition in 1925-1927, identified a tongue-like, southward flowing core of North Atlantic Deep Water (NADW) and a northward flowing core of Subantarctic Intermediate Water (and Antarctic Bottom Water; *Wüst, 1935*). Later, in 1957, Henry Stommel revolutionized the idea of the overturning circulation by presenting a series of illustrations showing that surface water sinking in the north (-i.e. NADW) is connected to the upwelling water in the south by deep and narrow western boundary currents (*Stommel, 1957*). Further, based on T-S diagrams and the high dissolved oxygen concentration below 3000 in the North Atlantic and the Weddell Sea, Stommel suggested that the deep ocean is filled by water forming in these regions (Figure 2.1; *Stommel, 1958*).

While temperature and salinity provided means to roughly trace interior waters to their formation regions, soon enough it became clear that these two properties alone do not provide sufficient constraints to decompose the world ocean water masses. *Jacobsen (1927)* and *Defant (1929)* used the T-S space to graphically calculate the mixing parameters by defining a "mixing triangle". This method offers a unique solution for a limited number $n = 3$ of water masses or sources, if more than 3 water masses are included, assumptions in mixing become critical, and results ambiguous (*Tomczak, 1981*). The use of nutrients to identify water masses did not bloom until *Redfield et al. (1963)* discovered how the nutrient concentrations are related to the oxygen concentration. Nutrients and oxygen were now tied together by the so-called Redfield ratio, which described their proportional concentrations in seawater. The idea of developing a conservative water-mass property from nutrients was later on refined by Wallace "Wally" Smith Broecker (*Broecker and Peng, 1982*). In light of the limitations of temperature and salinity, Broecker developed nearly conservative properties by correcting the nutrients measurements for remineralization using the Redfield ratios, the so-called "NO"

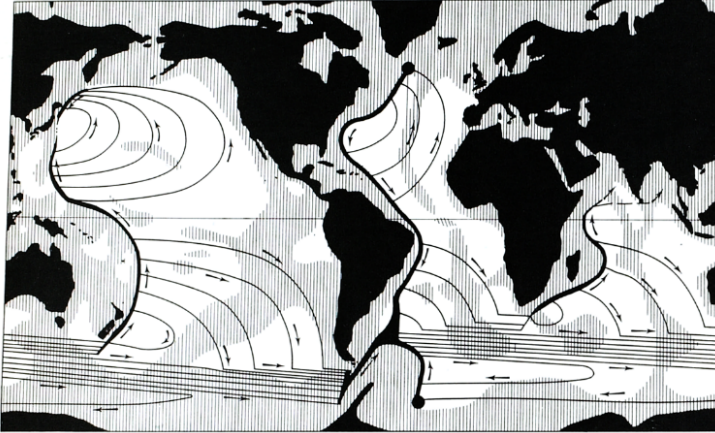


Figure 2.1: Representation of the abyssal circulation by [Stommel \(1958\)](#), where the North Atlantic and the Weddell Sea are the only two sources of deep waters. Thick streamlines represented the flow of sinking water as western boundary currents and narrow streamlines represent the return flow to the poles. Figure from [Stommel \(1958\)](#).

([Broecker, 1974](#)) and " PO_4^0 " tracers ([Broecker et al., 1985](#)). NO (calculated as $NO = 9NO_3 + O_2$) and PO_4^0 ($PO_4^0 = PO_4 + \frac{O_{2,eq} - O_2}{175}$) are closely related to the concept of preformed nutrients, - i.e, nutrients present at the time of subduction. Because Antarctic Waters have roughly twice as high preformed nutrients as waters from the North Atlantic, NO and PO_4^0 are powerful tools to distinguish waters of northern and southern origin. The analysis of water masses was further formalized by [Tomczak \(1981\)](#), who proposed a method where n water masses were quantified with $n - 1$ independent parameters, the Optimum Multiparameter Analysis (or OMP). OMP is an extension of the set of equations which form the basis of the mixing triangle derived from the T-S diagrams: Any water type can be expressed as the linear combination of the mixing of different sources. Thus, OMP consists of $n - 1$ linear tracer equations plus an extra equation to assure the conservation of mass. Nutrients, corrected for remineralization, were obvious candidates for those extra parameters, and the combination led to a very prolific method which revolutionized our knowledge of the world ocean's water masses and is still in use (e.g., [Tomczak and Large, 1989](#); [Karstensen and Tomczak, 1998](#); [Leffanue and Tomczak, 2004](#); [McKenna et al., 2016](#)).

One of the limitations of OMP, however, is that the water-mass source properties are subjectively defined. While these studies resolved as many water masses as their number of variables permitted, it is uncertain how many water masses are necessary to obtain an accurate and stable decomposition. Numerical model studies have shown that many different surface regions contribute to the interior ocean water-mass properties (e.g., [Haine and Hall, 2002](#); [Primeau, 2005](#); [Khatiwala, 2007](#)), and thus, there is the possibility that every region in the ocean exerts non-zero contribution to the interior ocean waters. [Gebbie and Huybers \(2010\)](#) proposed a new inverse method to overcome this issue, named Total Matrix In-

tercomparison (TMI). While the TMI is based on the same tracer conservation equations as the OMP, in this method all present-day surface property combinations are potential sources to the interior. As the ocean is discretized into multiple boxes, each box exchanges mass and properties with the neighbouring 6 boxes and these fluxes can be estimated via the tracer conservation equations (Chapter 3). Thus, the TMI provides steady-state mixing pathways from surface to any point in the ocean interior. This method provided an image of how the ocean is filled (Figure 2.2; *Gebbie and Huybers, 2011*), where most of the ocean has a non-negligible contribution to the ocean interior volume, adding more realism to Stommel’s vision of two main water masses formed at high latitudes.

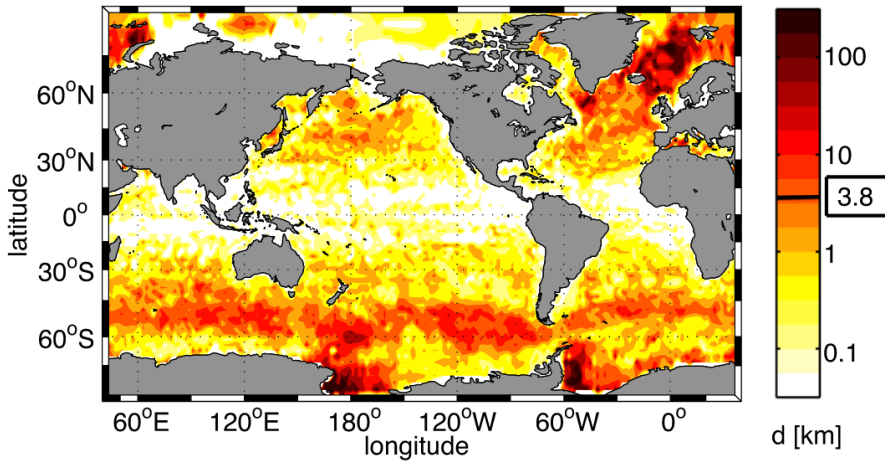


Figure 2.2: The sources of the global ocean waters. The colour scale represents the depth (in km) that each of the 2° by 2° surface grid cells would need to have, to store the ocean volume formed there. For reference, the colorbar includes the average depth of the ocean (3.8 km). From *Gebbie and Huybers (2011)*.

2.2 Ocean uptake of anthropogenic carbon

Anthropogenic carbon (C_{ant}) is defined as the surplus of Dissolved Inorganic Carbon (DIC) from its preindustrial concentrations (DIC_{pre}) caused by the invasion of man-made CO_2 , $C_{ant} = DIC - DIC_{pre}$. The inventory of C_{ant} corresponds to about 175 ± 35 PgC for 2021 (*Friedlingstein et al., 2022*; *Khatiwala et al., 2013*; *DeVries, 2014*), about a quarter of the anthropogenically emitted 670 ± 65 PgC. C_{ant} only corresponds to 0.45% of the total carbon present in the ocean 37.000 PgC (*Sarmiento and Gruber, 2002*; *Friedlingstein et al., 2022*).

The uptake of C_{ant} is regulated by an interaction of physical and chemical processes (*Maier-Reimer and Hasselmann, 1987*). The chemical processes control the mass of carbon that can be absorbed into the well-mixed upper ocean for a given

rise in atmospheric CO_2 before equilibrium is reached. Physical processes, on the other hand, control the extent to which waters enriched in C_{ant} are transported away from the upper ocean mixed layer into the deep ocean (*Graven et al., 2012; Sarmiento et al., 1992*) and replaced with older waters through upwelling. These older waters have not been exposed to the present atmosphere, and thus provide the surface ocean with capacity for further C_{ant} update. Thus, the ocean circulation ensures the ongoing uptake of atmospheric CO_2 by the subduction of carbon across the mixed layer.

2.2.1 Seawater CO_2 chemistry

Because of the increase in atmospheric CO_2 concentration, the ocean is typically undersaturated in CO_2 with respect to the atmosphere, which results in a flux of CO_2 into the ocean. As a result, and because emissions are steadily increasing, the ocean is a net sink of CO_2 . Once $\text{CO}_{2,atm}$ is dissolved in seawater, it enters the carbonate system where it forms H_2CO_3^* which is the sum of carbonic acid (H_2CO_3) and dissolved or aqueous CO_2 ($\text{CO}_{2,aq}$). H_2CO_3^* dissociates into bicarbonates (HCO_3^-) and carbonates (CO_3^{2-}) according to the set of equilibrium reactions for CO_2 in seawater:



where k_0 is Henry's constant for solubility, and k_1 and k_2 the first and second carbonate dissociation constants, respectively. The sum of the concentrations of all carbonate species is referred to as Dissolved Inorganic Carbon (DIC):

$$\text{DIC} = [\text{H}_2\text{CO}_3] + [\text{HCO}_3^-] + [\text{CO}_3^{2-}] \quad (2.4)$$

The capacity of the ocean to absorb atmospheric CO_2 or buffer capacity, is formally quantified as the Revelle factor, γ_{DIC} , and expressed as the sensitivity of CO_2 partial pressure ($p\text{CO}_2$) to changes in DIC (*Revelle and Suess, 1957; Middelburg et al., 2020*):

$$\gamma_{DIC} = \frac{\text{DIC}}{p\text{CO}_2} \frac{\partial p\text{CO}_2}{\partial \text{DIC}} \quad (2.5)$$

where:

$$p\text{CO}_2 = \frac{k_2}{k_0 \cdot k_1} \frac{[\text{HCO}_3^-]}{[\text{CO}_3^{2-}]} \quad (2.6)$$

Using typical values for DIC and $p\text{CO}_2$ for the surface ocean, the buffer factor yields values of about 12, meaning that 12% change in $p\text{CO}_2$ corresponds to a 1% change in DIC. The Revelle factor increases with increasing temperature through the solubility of CO_2 . Higher concentrations of CO_3^{2-} would enable the ocean

to absorb more CO_2 without increasing the $p\text{CO}_2$. The dissociation of CO_2 in seawater releases a hydrogen ion H^+ , which reacts with CO_3^{2-} to form HCO_3^- . These reactions maintain the $p\text{CO}_2$ levels and regulate the pH. Thus, the higher $[\text{CO}_3^{2-}]$, the higher the buffer capacity. In the ocean, CO_3^{2-} has originated from the weathering of continental calcium carbonate and silicate and subsequent transport by rivers over on millennial timescales, only affecting the buffer capacity on those timescales (Archer *et al.*, 1997).

2.2.2 Inventories, transport and fluxes

Because C_{ant} represents such a small perturbation with respect to the preindustrial background, it is not distinguishable by direct observations. Therefore, the separation between preindustrial and anthropogenic carbon relies on back-calculation methods that correct DIC for remineralization, or indirect methods that estimate ocean ventilation timescales.

Among the back-calculation methods, the most prominent example is the ΔC^* method, proposed by Gruber *et al.* (1996) and employed by Sabine *et al.* (2004) to provide the first global inventory of C_{ant} (Figure 1.1). This method relies on correcting the DIC concentration for remineralization, which is estimated from oxygen via stoichiometric ratios, assuming steady state circulation, alkalinity and biology to remain unchanged since the preindustrial. The main assumption is, however, that the air-sea CO_2 disequilibrium (ΔC_{dis}) has remained constant since the preindustrial era and along isopycnals. ΔC_{dis} is estimated from water parcels in the deep ocean that is far enough from the outcrop region to be contaminated with C_{ant} . Here, the air-sea disequilibrium matches the mean ΔC^* of the isopycnal surface interval. For the upper ocean where waters are already contaminated with C_{ant} , the age of the water parcel has to be determined from transient tracers, such as sulfur hexafluoride (SF_6) and chlorofluorocarbons (CFCs), which allows to scale the upper ocean CO_2 concentration with the known atmospheric concentration at the time of subduction.

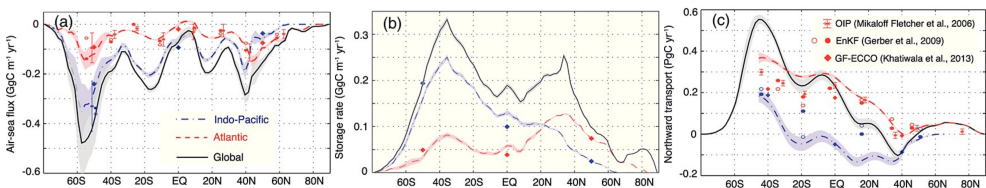


Figure 2.3: Zonally integrated (a) air-sea anthropogenic CO_2 flux, (b) anthropogenic CO_2 storage rate, and (c) northward anthropogenic CO_2 transport from the Ocean Circulation Inverse Model (OCIM) in the Atlantic (dashed red curves), Indo-Pacific (dot-dashed blue curves), and global oceans (solid black curves) for the year 2012. Shading represents the 1σ uncertainty envelope from the ensemble of OCIM runs. Figure from DeVries (2014).

The Transient Time Distribution (TTD) method is a development of the ΔC^* shortcut method of Gruber *et al.* (1996), which consists in directly estimating C_{ant}

from transient tracers. TTDs provide the distribution of times that it takes for mixed-layer waters to arrive to an interior point (*Holzer and Hall, 2000*). In order to constrain the TTDs, a given transient tracer must have an increasing atmospheric history, its time history at the surface ocean must be known, and it must be inert. CFC-12 has been the most common transient tracer used to constrain the TTDs. But, since the decline in its atmospheric concentrations from 2002, SF₆ is increasingly used. The TTD is approximated by an Inverse Gaussian distribution (*Hall et al., 2002*) by defining a specific ratio between the mean (Γ) and the width (Δ), then the concentration of transient tracers is used to determine the TTD (*Hall et al., 2002; Waugh et al., 2004, 2006*). Those TTDs can be then used to estimate the interior ocean C_{ant} content by assuming constant ΔC_{dis} , just like the ΔC^* method. The additional assumptions for the TTD method are the degree of saturation of the transient tracers in surface waters, and the shape of the TTD (Δ/Γ ratio).

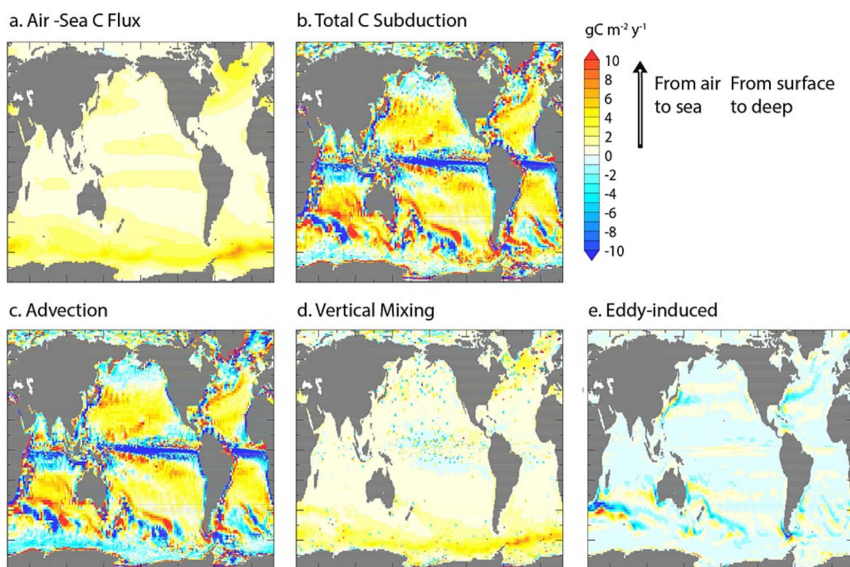


Figure 2.4: Spatial distribution of anthropogenic (a) carbon air-sea flux and (b) total anthropogenic carbon subduction from the NEMO-PISCES model. The subduction flux is then decomposed into (c) advection, (d) vertical mixing and (e) eddy-induced components. Fluxes, in $\text{mol C m}^{-2} \text{ yr}^{-1}$, averaged over 1998-2007, are counted positively when directed from the atmosphere to the ocean, and from the surface to the deep ocean. Figure from *Bopp et al. (2015)*.

The main limitation of the ΔC^* and TTD methods is that they only provide a snapshot of the C_{ant} inventory, where no temporal information can be derived. Transport matrices have been used to provide the first 3D estimates of C_{ant} distribution, as well as its storage rate, air-sea fluxes and transport (Figure 2.3; *Khatiwala et al., 2009, 2013; DeVries, 2014*). Such methods rely on constraining ocean circulation prior to the C_{ant} estimations, starting from a General Circulation Model that is optimized with observations of tracers, such as temperature, salinity, radiocarbons and CFCs. The evolution of C_{ant} is obtained by resolving

the air-sea disequilibrium and assuming C_{ant} behaves as a passive tracer. These methods have further depicted the role of high latitudes in the uptake and transport of C_{ant} , where the Southern Ocean uptake corresponds to about 30% of the global, which is then transported northwards. The results provided by these methods are part of the cornerstones of oceanic C_{ant} studies.

The fluxes across the base of the mixed layer remove carbon from the well-ventilated mixed layer into the interior ocean, representing the rate-limiting step of the ocean C_{ant} uptake. The only global estimates of the C_{ant} fluxes across the mixed layer are provided by [Bopp *et al.* \(2015\)](#), where they used a General Circulation Model to show that global subduction is dominated by the Southern Ocean and the subtropics (Figure 2.4). The subduction in the Southern Ocean was found to be a result of vertical mixing, while in the subtropics, it is a result of the interplay between the sloping mixed-layer base (horizontal mixed-layer base depth gradients) and lateral advection, including Ekman pumping. At high northern latitudes, vertical mixing was found to drive most of the subduction.

2.3 Ocean deoxygenation

Ocean deoxygenation results from the increasing demand for oxygen with respect to the supply. Part of the oxygen supply is determined by the concentration at surface, mainly controlled by the solubility; the warmer the water the smaller its solubility for oxygen. Similarly, the supply and demand of oxygen are tightly linked with changes in primary production through the production and remineralization of organic matter. Ocean circulation is also an important factor regarding supply and demand; the faster the ocean is ventilated the more oxygen would be supplied and the less time there is for remineralization of organic matter. Oppositely, the more sluggish circulation, the less oxygen would be supplied and the more time there is for remineralization. The myriad factors involved in the oxygen cycle make it a difficult task to disentangle the fine balance between the biogeochemical and physical processes that determine the supply and demand of oxygen.

2.3.1 Sources and sinks

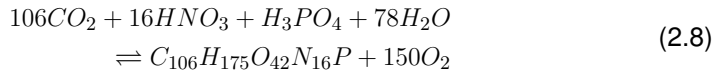
The oxygen concentration at equilibrium is given by Henry's law ([Henry, 1803](#)):

$$[O_2]_{eq} = S_{O_2} \cdot pO_2 \quad (2.7)$$

where $[O_2]_{eq}$ is the seawater concentration of oxygen at equilibrium, S_{O_2} its solubility and pO_2 is its partial pressure in the atmosphere. As for every gas, the solubility is primarily controlled by temperature (and to a lesser extent salinity). The lower the temperature is, the more soluble is oxygen. For this reason, surface waters in polar and subpolar are typically richer in oxygen than tropical and subtropical regions. However, the surface ocean is rarely in equilibrium with the atmospheric oxygen concentration, but rather oversaturated or undersaturated

because of primary production and the short residence time of waters at the surface.

Oxygen is a byproduct of the synthesis of organic matter by primary producers (*Anderson and Sarmiento, 1994*):



where nutrients (left-hand side) are the reactants of the reaction and organic matter ($C_{106}H_{175}O_{42}N_{16}P$) and O_2 are the products. The reverse reaction (from right to left) is the remineralization of organic matter and consumes oxygen to produce nutrients.

The production of organic matter can lead to regions that are oversaturated in oxygen with respect to its solubility concentration, these regions are located in the euphotic zone, where there is enough sunlight and nutrients for photosynthesis to occur. Conversely, the remineralization of organic matter consumes oxygen. This process occurs within the entire water column, but only the remineralization below the mixed layer will impact the interior oxygen concentrations, as these waters are not in contact with the atmosphere any longer. In addition, oxygen concentration can be undersaturated at surface, for example, as a result of vigorous ventilation that prevents oxygen to reach equilibrium with the atmosphere, or due to rapid heat loss that increases its solubility. For the global mixed layer, the equilibration time for oxygen is about one month, on average. If the residence time of the waters at surface is shorter than the equilibration time, that water parcel would be undersaturated.

The consumption of oxygen is commonly measured as the difference between the observed concentration $[O_2]_{obs}$ and $[O_2]_{eq}$. The resulting quantity is known as Apparent Oxygen Utilization (AOU):

$$AOU = [O_2]_{eq} - [O_2]_{obs} \quad (2.9)$$

AOU is a fairly trivial way to estimate oxygen utilization, however, it inherits the biases regarding the disequilibrium of oxygen at the ocean surface and translates them into a systematic overestimation of respiration in the interior ocean, especially in deep and cold waters (*Ito et al., 2004*). A more correct metric for oxygen utilization can be estimated from preformed oxygen ($[O_2]^0$) and is known as True Oxygen Utilization (TOU; *Broecker and Peng, 1982*):

$$TOU = [O_2]^0 - [O_2]_{obs} \quad (2.10)$$

For a water parcel in the mixed layer, $[O_2]^0$ is set at the time of subduction and is then transported into the interior ocean by circulation. The preformed properties are conservative properties with no ocean interior sinks and thus represent the mixed layer properties during winter. The differences between AOU

and TOU arise from the surface disequilibrium at the time of subduction and water mass formation, and from the mixing in the interior ocean combined with the nonlinearity in the temperature dependence of the solubility of oxygen (*Ito et al., 2004*). While TOU is advantageous compared to AOU, it is not possible to derive $[O_2]^0$ directly from observations. General Circulation Models and transport matrices, however, can be used to obtain the distribution of $[O_2]^0$ and therefore a more correct estimation of the ocean respiration (*Ito et al., 2004; Carter et al., 2021*).

AOU (and TOU) just provides the amount of oxygen that has been utilized since the water parcel was detrained from the mixed layer and not the rate at which the oxygen has been utilized. Oxygen Utilization Rate (OUR) was first estimated indirectly from the remineralization of Particulate Organic Carbon in sediment traps by *Martin et al. (1987)*, showing that most of the remineralization occurs in the upper water column, with particulate carbon fluxes following a power law distribution (Figure 2.5). OUR is, however, generally derived directly from oxygen, from isopycnal trends in AOU and water mass ages as determined from transient tracers (*Jenkins, 1998; Sonnerup et al., 2019*):

$$OUR = \frac{AOU}{age} \quad (2.11)$$

OUR provide valuable information regarding how the oxygen content would be affected by ventilation changes. However, several assumptions are involved in determining OURs from age. First, AOU and age trends are assumed to result from the ageing of the water mass with concomitant oxygen consumption, and not a result of mixing between waters of different ages with different AOU (*Sonnerup et al., 2019*). A second source of uncertainty is the age of the water. As for estimating C_{ant} , the age of the waters can be estimated from transient tracers such as CFCs by constraining the TTD. In this case, assumptions must be applied regarding the degree of saturation of surface waters and the shape of the TTD. These assumptions can yield significantly different OURs (Figure 2.5). More importantly, these estimates only provide a path integrated (from surface

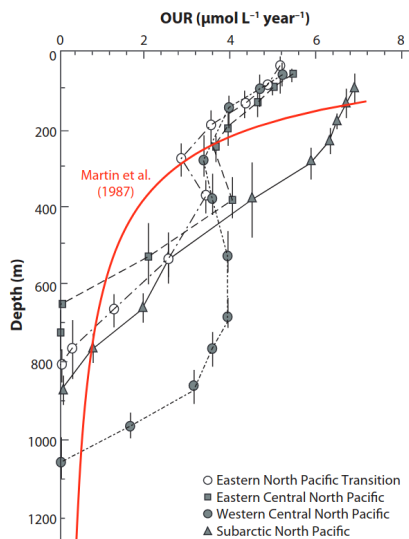


Figure 2.5: The Oxygen Utilization Rate (OUR) in $\mu\text{mol L}^{-1} \text{yr}^{-1}$ (thick red line) versus depth from the model of *Martin et al. (1987)* and from a recent compilation of profiles based on apparent oxygen utilization and CFC ages from *Feely et al. (2004)*. Figure from *Keeling et al. (2010)*.

to interior) estimate of oxygen utilization, representing a signal where both oxygen utilization and ocean circulation are combined (*Holzer, 2022*), and therefore do not inform about where the oxygen has been consumed. Disentangling the oxygen loss from the circulation signal is critical to understand how changes in ventilation and primary production will affect the interior ocean oxygen.

2.3.2 Open ocean Oxygen Minimum Zones

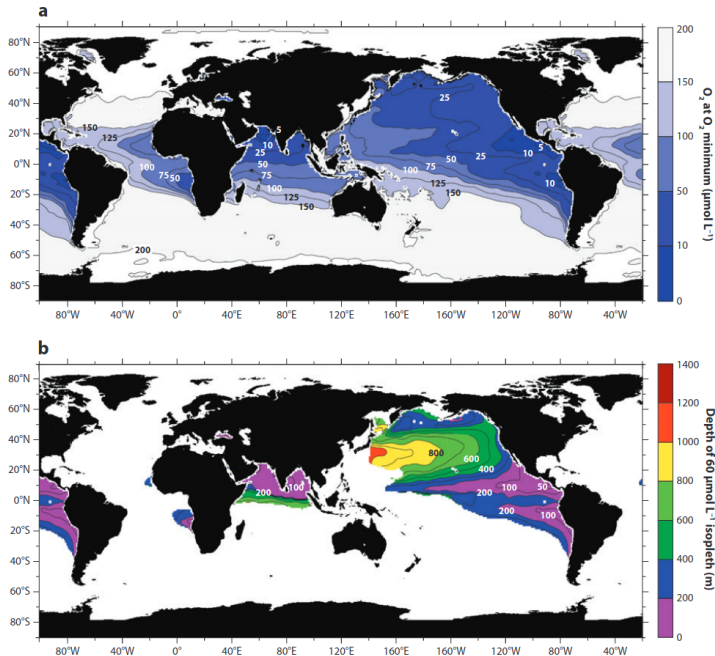


Figure 2.6: a) Oxygen concentrations at the depth of minimum oxygen. b) Depth of the $60 \mu\text{mol L}^{-1}$ isopleth in meters. Figure from *Keeling et al. (2010)*.

Because Oxygen Minimum Zones (OMZs) are regions in the ocean that are already deficient in oxygen, they are especially sensitive to further deoxygenation. OMZs are usually found in the tropics, at depths between 100 m and 900 m, and coinciding with upwelling regions and the so-called "shadow zones" of the thermocline ventilation (Figure 2.6). The oxygen concentration in these regions can be as low as $4.5 \mu\text{mol kg}^{-1}$ (*Karstensen et al., 2008*). The expansion of OMZs is a threat under the ubiquitous impacts of ocean deoxygenation. Regions already below $60 \mu\text{mol kg}^{-1}$ are effectively "dead zones" for many higher trophic level animals such as fish and crustaceans (*Gray et al., 2002*). Below $20 \mu\text{mol kg}^{-1}$, denitrification takes place (*Smethie, 1987*), leading to the production of nitrous oxide, which is a powerful greenhouse gas that amplifies global warming (*Keeling et al., 2010*). Thus, the expansion of OMZs would exert a positive feedback in the climate system (*Keeling and Garcia, 2002; Cabré et al., 2015*). Direct observations show that

this expansion is already taking place (*Stramma et al., 2010; Zhou et al., 2022*), but these changes are uncorrelated with the rising temperature during the last decade (*Stramma and Schmidtko, 2021*).

The sensitivity of OMZs to climate results from a fine balance between physical and biogeochemical processes that control the supply and demand of oxygen, respectively, as well as their timescales. There are three mechanisms that can contribute to the oxygen-deficit of OMZs: i) Typically, OMZs are located underneath high productivity upwelling areas (*Helly and Levin, 2004*), thus, export of copious amounts of organic material and its remineralization can generate the oxygen-deficit observed at OMZs; ii) the location of OMZs often coincide with the so-called "shadow zones" of thermocline ventilation pathways (*Luyten et al., 1983*) such that a combination of average oxygen consumption and sluggish circulation can lead to low oxygen; or iii) ample oxygen consumption can occur along the pathways as water circulates from the surface ocean to OMZs, such that the water masses that enter OMZs may be already low in oxygen. Current hydrographic observations indicate that the third mechanism, transport of low-oxygen waters into OMZs, dominates the origin of OMZs (*Olson et al., 1993; Kalvelage et al., 2013; Sonnerup et al., 2019*).

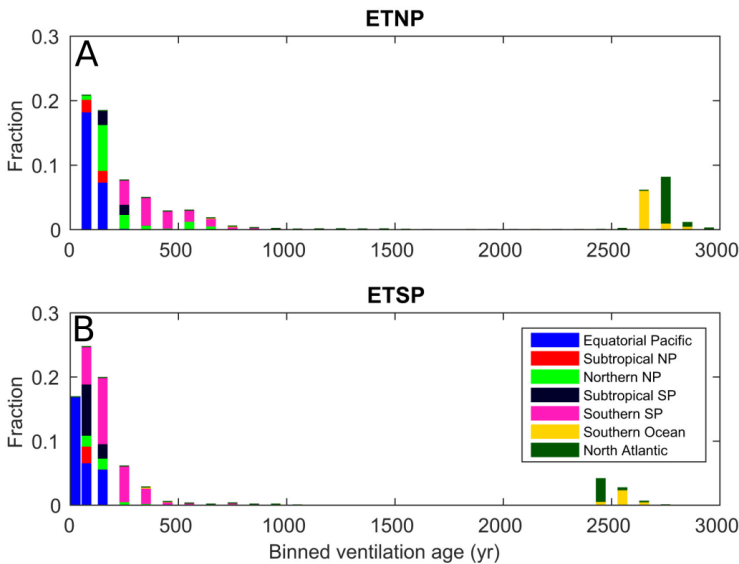


Figure 2.7: The volume fraction of OMZ waters contributed by different regions at different ventilation timescales for (A) Eastern Tropical South Pacific (ETSP) and (B) the Eastern Tropical North Pacific (ETNP). Figure from *Fu et al. (2018)*.

Transport matrices can be used to infer global ventilation pathways to the OMZs, as well as their timescales. *Fu et al. (2018)* used a transport matrix based on the ocean circulation field of an Earth System Model (ESM) to quantify which surface ocean regions ventilate the Pacific OMZs, the Eastern Tropical South Pacific (ETSP) OMZ and the Eastern Tropical North Pacific (ETNP) OMZ, and at

what timescales. They show that these OMZs are mostly ventilated by the Equatorial Pacific and intermediate waters, at decadal and centennial timescales, respectively. High latitudes, on the other hand, contribute marginally to the OMZs volume at millennial timescales (Figure 2.7). *DeVries et al. (2012)* used another transport matrix, Ocean Circulation Inverse Model (OCIM), and estimated that these OMZs are replenished by surrounding waters at decadal timescales, -i.e., ETSP in 0.9 ± 0.4 yr and the ETNP in 3.9 ± 0.8 yr), indicating that OMZs are not stagnant, supporting the idea that the waters that enter OMZs are already low in oxygen before reaching the OMZ.

The fate of oxygen in the ocean has recently been explored by *Holzer (2022)*, using an updated version of the OCIM transport matrix (*DeVries and Holzer, 2019*). Southern Ocean and the North Pacific contribute to most of the oxygen that is remineralized within the ETNP OMZ (Figure 2.8A). Similarly, oxygen utilization also happens in the interior ocean, away from the OMZ, that is subsequently transported as oxygen-deficit to the OMZ (Figure 2.8B). Therefore, part of the oxygen-deficit in the ETNP OMZ would originate remotely, with important implications for the origin and sensitivity of OMZs to climate.

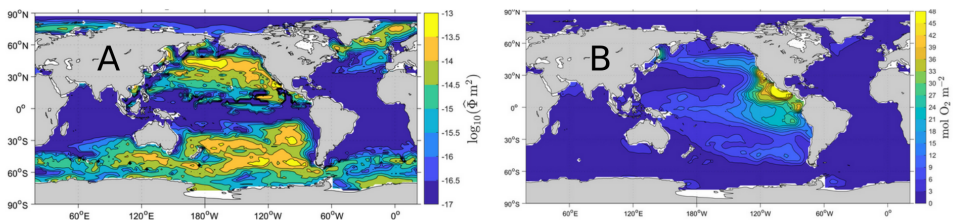


Figure 2.8: The flux of O₂ from the atmosphere into the ocean that is destined to be utilized in the East Tropical North Pacific (ETNP) OMZs (A), and the oxygen utilization at each inner ocean location that will be transported as oxygen-deficit to the ETNP OMZ (B). Figure adapted from *Holzer (2022)*.

Chapter 3

Data and methods

This chapter describes the methods used throughout this thesis, the Total Matrix Intercomparison (TMI), and how it was applied to answer the questions and reach the objectives posed in this thesis. In Paper I and II we use the global version of the model developed by *Gebbie and Huybers (2012)* to investigate the origin, transport and fate of C_{ant} and oxygen on the ocean. In paper III we build upon a regional, high resolution version for the Nordic Seas developed by *Brakstad et al. (2023)* to constrain the ventilation timescales through the inversion of water-mass mean ages derived from CFC-12 observations.

3.1 Total Matrix Intercomparison (TMI)

The TMI, and transport matrices in general, fall between observational methods and more complex dynamical General Circulation Models. Transport matrices are offline circulation models, -i.e., they are not coupled with other components such as an atmospheric model, and they represent a climatological, steady-state circulation. In essence, they connect a surface boundary condition with any interior point as mass fluxes between boxes. The circulation in transport matrices can be i) constrained from observations, as in the case of the TMI, or ii) derived directly from a GCM as in the Total Matrix Method (TMM) from *Khatiwala et al. (2005)*, or iii) a combination of both, were the parameters involved in General Circulation Models are optimized by the use of observations, where the Ocean Circulation Inverse Model (OCIM) by *DeVries and Primeau (2011)* is the main example. While the steps to constrain the circulation matrices differ, all these methods converge once the matrix is obtained. This matrix is a diffusive-advective transport operator that connects every grid cell among each other through mass fluxes, which results in a square matrix. From here on, I refer to this matrix as the pathway matrix or \mathbf{A} matrix. Because most of the grid cells only interact with the neighbouring boxes, \mathbf{A} is highly sparse (mostly full of zeros). The key aspect to bear in mind here, is that the matrix formulation of such circulation models allows for efficient diagnostics that are computationally very expensive in General Circulation Models.

From any of the \mathbf{A} , one can relate the distribution of a tracer in the ocean with its boundary conditions and interior sources from the steady-state tracer equation:

$$\mathbf{A}\mathbf{c} = \mathbf{d} \quad (3.1)$$

where \mathbf{c} is the vector formed from a three-dimensional tracer distribution, such as temperature or oxygen, and \mathbf{d} is the forcing vector that contains the boundary conditions and interior sources/sink:

$$\mathbf{d} = \mathbf{B}\mathbf{c}_b + \mathbf{\Gamma}\mathbf{q} \quad (3.2)$$

where \mathbf{B} and $\mathbf{\Gamma}$ are the mixed-layer and interior ocean masks, respectively, that prescribe the mixed-layer concentration boundary condition \mathbf{c}_b and interior biogeochemical sources/sinks \mathbf{q} . Equation (3.1) thus becomes:

$$\mathbf{A}\mathbf{c} = \mathbf{B}\mathbf{c}_b + \mathbf{\Gamma}\mathbf{q} \quad (3.3)$$

In the TMI, \mathbf{A} , \mathbf{c}_b and \mathbf{q} are constrained through inversion of the tracer conservation equations for six ocean properties (potential temperature (θ), salinity, $\delta^{18}\text{O}_{sw}$, PO_4^{3-} , NO_3^- and O_2 ; *Gebbie and Huybers, 2010*). The global version is constructed from the World Ocean Circulation Experiment (WOCE) climatology (*Gouretski and Koltermann, 2004*), while the Nordic TMI is based on the climatology constructed by *Brakstad et al. (2019, 2023)* which includes the same tracers as the global with the exception of $\delta^{18}\text{O}_{sw}$. The TMI is based on the principle that the observation of a tracer at an interior point C_i can be expressed as the linear combination of multiple sources:

$$C_i = \sum_{j=1}^N m_{ij}C_j + q_i \quad (3.4)$$

where $N = 6$ is the number of neighbouring boxes, m_{ij} is the fraction of water that originates from the cell j with property C_j and $\sum_{j=1}^N m_{ij} = 1$ to assure mass conservation, and q_i is interior sources/sink for C_i .

Additionally, the global version of the TMI includes radiocarbon ($\Delta^{14}\text{C}$), which were mapped obeying the diffusive-advective pathways in \mathbf{A} (*Gebbie and Huybers, 2012*). Because radiocarbon decay in time, they can be used to estimate the mean age of the ocean:

$$a_i = \sum_{i=1}^N m_{ij}a_j + \tau_i \quad (3.5)$$

where m_i is taken from \mathbf{A} and is the mass fraction of water contributed by each of the neighbouring boxes, a_i is the mean age in each box, and τ_i is the age source or local residence time of the waters and is computed as $\tau = C_{sink}/\lambda C$. *Gebbie and Huybers (2012)* solved for C_{sink} with Equation (3.4) and λ is the radioactive

^{14}C decay rate ($\lambda = \log(2)/5730\text{yr}$).

From the interior age sources or local residence times τ , one can calculate the time required for each of the grid cells to outflux its volume, \mathbf{F}_0 , as the inverse of τ ($\mathbf{F}_0 = 1/\tau$), where \mathbf{F}_0 has units of yr^{-1} . The product of \mathbf{F}_0 and the pathways matrix \mathbf{A} gives us the transient version of the TMI, the \mathbf{L} matrix, that include transport rates:

$$\mathbf{L} = \mathbf{F}_0 \mathbf{A} \quad (3.6)$$

The evolution of a conservative tracer $\frac{dc}{dt}$ can be obtained by timestepping the product of \mathbf{L} and the tracer \mathbf{c} :

$$\frac{dc}{dt} = \mathbf{L} \mathbf{c} \quad (3.7)$$

By assimilating radiocarbon observations, *Gebbie and Huybers (2012)* also solved for the transit time distributions $G_s(i, t)$. The radiocarbon concentration C_i at a given ocean interior point i results from the contributions of multiple surface end-members (*Holzer and Hall, 2000*), with individual contributions decaying according to an age distribution $G_s(i, t)$:

$$C_i = \sum_{s=1}^N m_s C_s \int_0^{\infty} t G_s(i, t) e^{-\lambda t} dt \quad (3.8)$$

where N is the number of constituents, m_s is the mass fraction of the surface end-member s , and C_s is the initial concentration of the same end-member. The function $G_s(i, t)$ is the distributions of transit times from a source region or end-member s to the interior ocean, and is equivalent to a TTD, although the latter usually denotes the global surface as surface source region. The transit time distributions estimated by *Gebbie and Huybers (2012)* are used in Paper I to trace the interior distribution of C_{ant} back to the mixed layer, in time and space. In Paper II, they are used to estimate the sensitivity timescales of OMZs to surface perturbations.

3.2 Constraining ventilation rates in the Nordic Seas

The global TMI contains steady-state ventilation rates obtained through the inversion of radiocarbon (*Gebbie and Huybers, 2012*), and is referred to as a transient steady-state version. The Nordic TMI, however, only contains the steady-state pathways as none of the tracers originally used to constrain it includes temporal information. Therefore, some of the aspects researched in Paper I and II that related to transit timescales, such as the distribution and fluxes of C_{ant} across the mixed layer, was not possible to investigate using the Nordic TMI developed by *Brakstad et al. (2023)*. Paper III builds upon the Nordic TMI and the method developed by *Gebbie and Huybers (2012)* to add ventilation rates to the climatological pathways in the Nordic TMI by inverting for water-mass mean ages derived from transient tracer measurements.

3.2.1 Water-mass mean ages

The ventilation and transport rates in the Nordic TMI are estimated by the inversion of ventilation or water-mass ages. *Jeansson et al. (2021)* estimated these ages from the CFC data in GLODAPv2 data synthesis product (*Olsen et al., 2016*) following the TTD method (*Waugh et al., 2004*). The dataset contains discrete estimates that were derived from ship-based CFCs measurements in the water column (Figure 3.1; DOI:10.25921/xp33-q351). For a steady-state transport, the interior concentration of a transient tracer with a known time-varying surface concentration $C_0(t)$ is given by the TTD $G(i, t')$. Similar to Equation (3.3) but with a different normalization (*Waugh et al., 2004*):

$$C(i, t) = \int_0^\infty C_0(t - t')G(i, t')dt' \quad (3.9)$$

The TMI has some advantages to estimate the transit time distributions compared to the classic TTD method. The main difference between Equation (3.8) and (3.9) is that in $C_0(t)$ in (3.9) is spatially uniform, -i.e., there is no distinction between sources, while (3.8) contains the pathways in m_s . Another important assumption is the degree of tracer saturation at surface waters and the shape of the TTD, as mentioned in Section 2.2.2. The degree of CFC-12 saturation in this dataset is assumed to be 100%. Some studies, however, suggest that is closer to 90% (*Doney and Jenkins, 1988*) and even lower in regions where the local residence time of waters at surface is not long enough to reach full equilibration with the atmosphere, notably in deep convection regions such as Labrador Sea (*Wallace and Lazier, 1988*) or Barents Sea, or regions covered with substantial sea-ice like the Chukchi Sea (*Terhaar et al., 2020*). The degree of saturation can also vary with time for the same location (*Jeansson et al., 2023*). Additionally, *Jeansson et al. (2021)* assumed a balance between advection and mixing, -i.e., unity ratio between the width and the mean age of the TTDs. While this assumption is typically adopted in the global ocean (e.g., *Waugh et al., 2006*), there is regional variability (e.g., *Stöven and Tanhua, 2014*; *Rajasakaren et al., 2019*). However, *Olsen et al. (2010)* showed that a unity ratio is appropriate for the Nordic Seas. The uncertainty of the mean ages, mostly as a consequence of potential errors in these assumptions, is about 20% (*Jeansson et al., 2021*).

The aim of the age inversion is to assimilate the estimates of water-mass mean ages consistently with the circulation pathways that already exist in the Nordic TMI transport matrix. In steady state and treating the water-mass age as an ideal tracer (e.g., *England, 1995*; *Peacock and Maltrud, 2006*), the surface boundary condition for the mean age is zero, and in an interior box, the mean age is given by τ in Equation (3.5).

To constrain τ from discrete estimates of interior ocean mean age, three pieces of information are necessary: i) The mass fraction fluxes m_i that are provided by the transport matrix \mathbf{A} from *Brakstad et al. (2023)*, ii) a first-guess boundary condition and interior sources \mathbf{d}_θ , and iii) the perturbations to the surface boundary condition \mathbf{u}_θ that best fits the discrete observations, \mathbf{y} , according to the cost

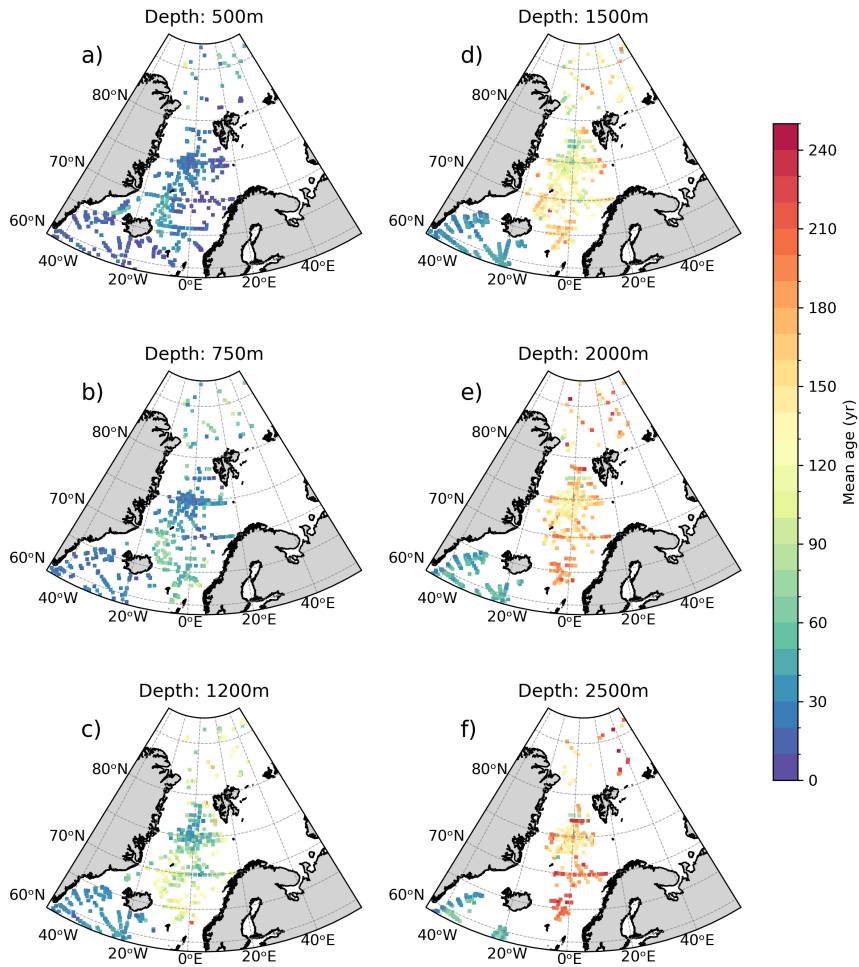


Figure 3.1: water-mass mean age estimates derived from CFC-12 observations by [Jeansson et al. \(2021\)](#) that are used to constrain the local residence time and ventilation timescales with the Nordic TMI.

function J :

$$\mathbf{J} = (\tilde{\mathbf{y}} - \mathbf{y})^T \mathbf{W}^{-1} (\tilde{\mathbf{y}} - \mathbf{y}) \quad (3.10)$$

where \mathbf{J} is the cost function of the problem, \mathbf{y} are the observational estimates linearly interpolated into the Nordic Sea grid, $\tilde{\mathbf{y}}$ is the modelled tracer at the same locations in the grid as the observations, and T indicates the transpose. Equation (3.10) has the form of a weighted least squares problem, where \mathbf{W}^{-1} is a diagonal matrix that contains the weights imposed to the model-data misfit $\tilde{\mathbf{y}} - \mathbf{y}$. \mathbf{W}^{-1} contains $1/\sigma_{obs}^2$ everywhere on its diagonal, where σ_{obs} is the observational error of the measurements.

The cost function \mathbf{J} is minimized subjected to the steady-state tracer equation (3.3), but substituting the right-hand side by a first guess:

$$\mathbf{A}\tilde{\mathbf{y}} = \mathbf{d}_\theta + \mathbf{u}_\theta \quad (3.11)$$

where \mathbf{A} is the matrix that contains the pathways and add the circulation constraints to $\tilde{\mathbf{y}}$. \mathbf{d}_θ is a vector of the first-guess boundary condition and interior estimate for τ_i , which are prescribed independently for the different boundaries of the domain and interior points. Finally, \mathbf{u}_θ is a vector containing the perturbations to the boundary conditions and interior age sources and are mapped into their corresponding location in \mathbf{d}_θ .

To solve for the $\tilde{\mathbf{y}}$ that best fits the data, a sensitivity or "adjoint" problem that gives a solution in one calculation is derived. First, Equation (3.11) is inverted and substituted into (3.10). This allows to write \mathbf{J} solely as a function of \mathbf{u}_θ . The sensitivity of \mathbf{J} (the output) is given by its partial derivative with respect to \mathbf{u}_θ (the input). Taking the partial derivative and setting it equal to zero, it is possible to solve for \mathbf{u}_θ and hence $\tilde{\mathbf{y}}$ (The complete derivation is available in the Auxiliary Material in [Gebbie and Huybers, 2011](#)). Finding the solution through the sensitivity of \mathbf{J} is much more computationally efficient than arbitrarily adjusting the \mathbf{u}_θ that best fits the data, which is prohibitive when \mathbf{u}_θ and $\tilde{\mathbf{y}}$ have many elements. The solution to the problem can be found by optimizing \mathbf{u}_θ so that it minimizes \mathbf{J} , and was performed through the "Optim.jl" Julia package and the LBFGS Gradient Descent algorithm (Mogensen2018; DOI:10.5281/zenodo.7350608). Once τ is constrained, the water-mass mean age can be estimated with Equation (3.3) and the evolution of a transient tracer with Equation (3.7).

Chapter 4

Summary of the papers

Paper I: How Is the Ocean Anthropogenic Carbon Reservoir Filled?

Xabier Davila, Geoffrey Gebbie, Ailin Brakstad, Siv K. Lauvset, Elaine L. McDonagh, Jörg Schwinger, and Are Olsen (2022), Global Biogeochemical Cycles, volume(36).

While the size of the global ocean reservoir of anthropogenic carbon (C_{ant}) is well constrained by different methods, the fluxes across the mixed layer that result in this reservoir are not, despite being the bottleneck for the uptake. The distribution of the C_{ant} inventory suggests that deep water formation regions are important for the vertical transport of C_{ant} , however, the exact magnitude of these fluxes has rarely been explored. Paper I estimates the fluxes of C_{ant} across the mixed layer using the TMI observation-based transport matrix. Here, the TMI is combined with an already published time-evolving boundary condition of C_{ant} to reproduce and trace back the current inventory to the regions of subduction in the mixed layer. When, where, and how much C_{ant} has been injected since the beginning of the industrial era is shown. Most of the C_{ant} stored below the mixed layer has been injected in the subtropics (40.1%) and the Southern Ocean (36.0%), while the largest fluxes have been in the Subpolar North Atlantic (Labrador and Nordic Seas). However, the large injection in the subtropics, has only penetrated the upper 1000 m of the water column, with the Subantarctic region and the Subpolar North Atlantic as the major contributors to the C_{ant} stored below this depth, 45.9% and 81.6% of their respective total injection, respectively. We also highlight the role of the Subpolar North Atlantic in fluxing out the carbon injected there. Specifically in the Nordic Seas, where 88.3% of the injected C_{ant} is transported to other oceanic regions. Paper I emphasizes the role of a few oceanic regions to fill the ocean C_{ant} reservoir.

Paper II: On the origins of open ocean Oxygen Minimum Zones

Xabier Davila, Are Olsen, Siv K. Lauvset, Elaine L. McDonagh, Ailin Brakstad, Geoffrey Gebbie (in review), Journal of Geophysical Research: Oceans

Under the ubiquitous threat of ocean deoxygenation, open ocean Oxygen Mini-

imum Zones (OMZs) are especially sensitive, and their expansion jeopardizes marine life and perturbs the ocean carbon and nitrogen cycles. Recent studies have suggested that OMZs are sustained by the supply of oxygen-poor waters rather than the local export and subsequent remineralization of organic matter within the OMZs. However, the mechanisms that form and maintain OMZs are not well constrained, such as the origin of the oxygen that oxygenates OMZs, and the locations where oxygen consumption occurs. Paper II uses the information implicit in the TMI to determine the origins of OMZs in terms of i) OMZ volume, ii) oxygen that survives remineralization and oxygenates OMZs, and iii) oxygen utilization in the interior ocean that contributes to the oxygen-deficit in the OMZs. Although OMZs are mostly ventilated by waters from high-latitude regions, these waters contribute little to the oxygenation of the OMZs, as most of the oxygen is utilized upon arrival. Instead, oxygen is mostly supplied by tropical, subtropical and intermediate waters originating in adjacent regions. An exception to this is the Nordic Seas, which contributes 14% of the oxygen that survives remineralization and oxygenates the North Pacific OMZ. In addition, we determine where the utilization of oxygen occurs along the water-mass pathways from the mixed layer to the OMZs, which we refer to as oxygen "remineralization pathways". These pathways show that less than a third of the oxygen-deficit in OMZs originates within the OMZs. Despite of the relatively small fraction, the most intense oxygen loss occurs in the OMZs. Other regions of substantial oxygen utilization are the Southern Ocean and, to a lesser extent, the North Pacific. Paper II highlights how waters originating from afar at high latitudes, with associated low remineralisation rates over relatively long time scales, have a significant role in shaping the OMZs.

Paper III: water-mass ages and ventilation timescales of the Nordic Seas inferred from transient tracers

Xabier Davila, Geoffrey Gebbie, Ailin Brakstad, Siv K. Lauvset, Elaine L. McDonagh, Emil Jeansson, Are Olsen (in prep.)

The Nordic Seas play a critical role in climate by taking up heat, C_{ant} and by oxygenating the world ocean due to a large amount of water mass being formed there and contributing to the Atlantic Meridional Overturning Circulation. Paper III investigates the ventilation timescales of the Nordic Seas by further developing an existing regional version of the TMI. The current version of the recently developed Nordic TMI provides the climatological water-mass pathways in the Nordic Seas but lacks any temporal information. In this paper, we assimilate water-mass mean ages derived from observations of CFC-12, into the existing pathways in the Nordic TMI by minimizing a weighted least square problem, and developing a transient version of the Nordic TMI. The ventilation timescales that are constrained represent the mean state of the Nordic Seas circulation rates. The residuals from the model-observation fit allow us to estimate changes in ventilation from the mean state. Prior to the 2000s, intermediate depths of the Greenland Sea were more slowly ventilated, reaching values closer to the mean state after

the reinvigoration of the Greenland Sea after the 2000s. Concurrently, the deepest parts of the Greenland Sea which were more ventilated than the mean state before the 2000s, became more sluggishly ventilated by the mixed layer. We also provide a glimpse of the capabilities of the transient Nordic TMI by emulating a dye experiment where the mixed layer in the Nordic Seas is dyed at once, representing a mixed-layer water vintage. The spatiotemporal evolution of this vintage is quantified. The mixed-layer water vintage is mostly restricted to the surface, while the deepest parts are barely ventilated by the Nordic Seas mixed-layer waters at any time scale. The evolution of the vintage suggests a very rapid renewal of the upper and intermediate waters, as about 50% of mixed-layer water vintage exit the domain after 5 years. Such rapid ventilation reinforces the idea that the Nordic Seas contributes to a large extent to the C_{ant} and oxygen world ocean inventory and that the deepest parts are now slowly filled by old waters from the Arctic.

Chapter 5

Synthesis

5.1 Synergy between papers

This dissertation assesses the role of ocean circulation for the origin, transport and fate of ocean anthropogenic carbon (C_{ant}) and oxygen by exploiting the potential of the observation-based TMI transport matrix ([Gebbie and Huybers, 2012](#); [Brakstad et al., 2023](#)) for applications in biogeochemistry. A water mass decomposition method such as the TMI, which reproduces the circulation pathways and timescales in a computationally inexpensive way, offers a wide range of possibilities for biogeochemical studies. This has been exemplified in Paper I by combining the TMI with additional data, and in Paper II by extracting the information inherent in the TMI. Paper I and II show how the distribution of C_{ant} and oxygen, is to a large extent controlled by ocean circulation in a large spectrum of spatial and temporal scales. Specifically, they highlight the role of high latitudes in the transport of these tracers across the mixed layer and into the interior ocean, from pole to pole. While a global perspective is necessary, the resolution of the global TMI is too coarse to determine smaller-scale processes. Regional, high-resolution tracer inversions such as the transient Nordic TMI, presented in Paper III, fill this gap.

Paper I shows that C_{ant} is mostly injected in the subtropics, Subantarctic and Subpolar North Pacific. Most of the C_{ant} injected in these regions is fluxed out and converges in the tropics, where the inventory is larger than the C_{ant} injected. While the subtropics are regions that contribute the most to the C_{ant} inventory, most of the injection occurs above 1000 m, where the resurface timescales are relatively short. In order to sequester C_{ant} effectively from the atmosphere, the C_{ant} needs to be injected below 1000 m, although regional differences exist ([Primeau and Holzer, 2006](#); [Siegel et al., 2021](#)). The Subpolar North Atlantic very efficiently injects C_{ant} below this depth (81.9 % of the total injection), contributing to the deep inventories of the world ocean. The role of the Nordic Seas is further highlighted when comparing the total injection in the Labrador and Nordic Seas. Our results suggest that the downward transports of C_{ant} in the Nordic Seas are 1.6 times larger than in the Labrador Sea. Such a dominant role of the Nordic Seas agrees with the volumetric contributions of these regions to the lower limb of the AMOC across the OSNAP (Overturning in the Subpolar North Atlantic

Program) current meter array (*Lozier et al., 2019*). Our calculated subduction rates of 2.6 Sv north of OSNAP-West and 12.6 Sv north of OSNAP-East agree well with the direct current measurements presented by *Lozier et al. (2019)*. Furthermore, the contribution from the Nordic Seas across the Greenland-Scotland Ridge of 8.1 Sv in the Green's function, is in agreement with the transport estimate by *Østerhus et al. (2019)* of 7.8 ± 1.9 Sv and by *Chafik and Rossby (2019)* of 6.87 Sv. In Paper III, the short outflux time of the mixed-layer water vintage, where 50% of the waters originated in the Nordic Seas mixed layer are not anymore present after 5 years, renders confidence of the outflux of C_{ant} in Paper I. Paper I and Paper III, therefore, agree that the Nordic Seas are rapidly flushed out, which would supply young and C_{ant} enriched waters afar in the world ocean.

Similarly, Paper II shows the important role of the Nordic Seas in supplying oxygen and oxygen-deficit to Oxygen Minimum Zones (OMZs). For most OMZs, the Subpolar North Atlantic contributes with low-oxygen waters (or oxygen-deficit). Part of the oxygen is utilized along the pathways that connect the mixed layer with the OMZs, but another large part is utilized around and within the OMZs. For most OMZs, the oxygen supply by the Subpolar North Atlantic is negligible, however, about 14% of the oxygen in the North Pacific (NP) OMZ originates in the Subpolar North Atlantic. While surprising, this is consistent with the study by *Holzer (2022)* that showed that a substantial amount of oxygen originating in the Subpolar North Atlantic is utilized in the North Pacific OMZ. In fact, the Subpolar North Atlantic is vital for the oxygenation of the world ocean (*Holzer, 2022*). The convection in the Greenland Sea has been reinvigorated since the 2000s and increased the oxygen levels in intermediate waters (*Lauvset et al., 2018*). Over the last decades, *Stendardo and Gruber (2012)* detected a positive trend in the oxygen concentration in the mode waters in the southwestern North Atlantic due to an increase in oxygen, which was linked with enhanced circulation or ventilation. Given the flux-out timescales of the Nordic Seas identified in Paper III, changes in the Greenland Sea gyre might be partially responsible for such changes.

5.2 Outlook

5.2.1 Challenges and opportunities

It has become increasingly evident that limiting the global average temperature increase to 1.5°C as stated in the Paris Agreement will only be achievable through large-scale deployment of carbon dioxide removal (CDR; *IPCC, 2021*), including ocean-based strategies (e.g., Ocean Alkalinity Enhancement or macroalgae cultivation; *Bach et al., 2019; Berger et al., 2023*). A critical task in the context of CDR is the Measurement, Reporting and Verification (MRV) of the amount of carbon effectively sequestered. However, MRV is an observational challenge due to the small signal-to-noise ratio of the carbon to be removed (of similar magnitude to the anthropogenic perturbation) with respect to the natural carbon

background and the spatial scales at which it would have to be deployed. According to *Berger et al.* (2023), ocean circulation may also limit the attribution of a DIC deficit (or enhanced air-sea carbon flux) to a specific CDR (e.g., macroalgal afforestation project), and therefore, MRV of CDR is likely to rely on the use of tracers of water mass residence time, ocean circulation, and gas exchange coupled with calibrated and validated numerical simulations.

Observation-based transport matrices, such as the TMI, may provide means to trace the perturbation of a specific CDR in terms of residence time and fate, similar to the study by *Siegel et al.* (2021). However, a number of developments would be beneficial to achieve this goal. First, the circulation in the global version of the TMI should be also constrained with age estimates derived from CFC-12 (as in Paper III) in combination with $\Delta^{14}\text{C}$, since Paper I suggests that the circulation in the upper ocean is too sluggish. Second, the inorganic carbon cycle should be represented in the TMI by assimilating DIC and alkalinity measurements (*Lawset et al.*, 2022), as well as surface ocean $p\text{CO}_2$ observations (*Bakker et al.*, 2016). The addition of the inorganic carbon cycle would provide a mean state of the natural carbon background plus a time-dependent C_{ant} perturbation. Constraining these components in a consistent manner would help to assess the sensitivity of the carbon cycle to CDRs in time and space.

While a global TMI is essential to understand the transport of carbon and oxygen (and other tracers), as shown in this dissertation, regional TMI as the one for the Nordic Seas provides information of pathways and ventilation timescales that a global model is unable of because of its coarse resolution and representation of local pathways. While the upper part of the Nordic Seas is rapidly ventilated by its mixed layer, the deeper part is not. Exploring the residence time of the deepest basins would give a sense of how effective would these regions be in terms of effective carbon sequestration if CDRs would be deployed.

The same analysis performed in Paper I and II could be done in the Nordic Seas with the Nordic TMI. But more generally, the Nordic TMI would allow us to explore the ventilation timescales in the Nordic Seas through a new methodology. For example, for studying the transport of heat and nutrient (e.g., *Gao et al.*, 2005; *Árthun et al.*, 2017; *Fransner et al.*, 2023), reproducing transient tracer release experiments (e.g., *Messias et al.*, 2008; *Marnela et al.*, 2008), or calculating transport rates (e.g., *Østerhus et al.*, 2019; *Chafik and Rossby*, 2019), applying these timescales for paleoceanographic studies (*Gebbie*, 2012).

One of the main limitations of the TMI is the steady-state nature of its pathways, and thus, changes in circulation and properties cannot be directly inferred. There are, however, other methods that are more appropriate to assess variability and its drivers. The use of the adjoint of more complex models, such as the adjoint of the MIT ocean general circulation model (MITgcm; *Marotzke et al.*, 1999; *Heimbach et al.*, 2005), would provide valuable information about the variability and sensitivity of interior ocean properties in a mechanistic way (*Hill et al.*, 2004). With the TMI, one can circumvent the lack of variability by constructing

different matrices for different periods (*DeVries et al., 2017*) or seasons. Given that there are enough observations to constrain the circulation for each of those periods, one could estimate changes in the pathways, remineralization, and ventilation timescales. However, unobserved regions do exist and can impede the development of time-evolving, or high-resolution regional matrices, such as the winter-time southern ocean or the deep ocean. While Argo programs such as the Deep-Argos and Biogeochemical Argos have the potential to provide enough data to build some of those inverse transport matrices, designing an efficient observing system is vital. Here, the use of the TMI and other adjoint models could assist in such an arduous task by avoiding sampling locations that contain redundant information (*Loose and Heimbach, 2021*).

5.2.2 Long-term perspective

While the transport across the mixed layer is the rate-limiting step for the uptake and governs the interior distribution of C_{ant} (*Sarmiento et al., 1992*) and oxygen (*Koelling et al., 2017*), the fluxes and the physical mechanisms that control them are poorly understood (*Sallée et al., 2012; Bopp et al., 2015*). Changes in the storage pattern of C_{ant} have been recently detected (*Gruber et al., 2019; Müller et al., 2023*), suggesting a strong role of circulation. However, to what extent are changes in the redistribution of C_{ant} , and changes in the fluxes across the mixed layer, responsible?

Henry Stommel imagined a "Demon" sitting in the base of the mixed layer, opening the door and allowing only late-winter mixed-layer waters to escape the mixed layer into the deep ocean (*Stommel, 1979*). Stommel's Demon operates at seasonal timescales (*Williams et al., 1995*), but also at interannual timescales via the effect of atmospheric forcing onto year-to-year changes in the mixed layer depth (*MacGilchrist et al., 2021*). The shallower the next year's mixed layer, the more water is effectively detrained from the mixed layer of the current year. And vice-versa, the deeper the mixed layer in the coming year, the more water is re-entrained. The mixed layer also affects the equilibration timescales of CO_2 (*Jones et al., 2014*), and thus, the concentration and subsequent fluxes out of the mixed layer. An anomalously deep mixed layer would result in longer equilibration times, but also in a larger volume detrained the subsequent year. To what extent do these mechanisms counteract each other? What is the net effect on the transport of carbon across the mixed layer? Is there a Demon in the transport of oxygen and carbon?

Chapter 6

Scientific results

Paper I

How is the Ocean Anthropogenic Carbon Reservoir Filled?

Xabier Davila, Geoffrey Gebbie, Ailin Brakstad, Siv K. Lauvset, Elaine L. McDonagh, Jörg Schwinger, and Are Olsen
Global Biogeochemical Cycles, **36** (2022)

Global Biogeochemical Cycles



RESEARCH ARTICLE

10.1029/2021GB007055

Key Points:

- The cumulative anthropogenic carbon fluxes across the mixed-layer base over the industrialized era are derived from observations
- The subtropics, Southern Ocean and North Atlantic are the main conduits of anthropogenic carbon from the surface to the interior ocean
- The subtropics have been the most efficient regions in transporting anthropogenic carbon across the mixed layer per unit of volume

Supporting Information:

Supporting Information may be found in the online version of this article.

Correspondence to:

X. Davila,
Xabier.Davila@uib.no






Citation:

Davila, X., Gebbie, G., Brakstad, A., Lauvset, S. K., McDonagh, E. L., Schwinger, J., & Olsen, A. (2022). How is the ocean anthropogenic carbon reservoir filled? *Global Biogeochemical Cycles*, 36, e2021GB007055. <https://doi.org/10.1029/2021GB007055>

Received 5 MAY 2021
 Accepted 28 APR 2022

© 2022. The Authors.
 This is an open access article under the terms of the [Creative Commons Attribution License](https://creativecommons.org/licenses/by/4.0/), which permits use, distribution and reproduction in any medium, provided the original work is properly cited.

How Is the Ocean Anthropogenic Carbon Reservoir Filled?

Xabier Davila¹ , Geoffrey Gebbie², Ailin Brakstad¹ , Siv K. Lauvset³ , Elaine L. McDonagh^{3,4} , Jörg Schwinger³, and Are Olsen¹ 

¹Geophysical Institute, University of Bergen, Bjerknes Centre for Climate Research, Bergen, Norway, ²Department of Physical Oceanography, Woods Hole Oceanographic Institution, Woods Hole, MA, USA, ³Norwegian Research Centre (NORCE) AS, Bjerknes Centre for Climate Research, Bergen, Norway, ⁴National Oceanography Centre, Southampton, UK

Abstract About a quarter of the total anthropogenic CO₂ emissions during the industrial era has been absorbed by the ocean. The rate limiting step for this uptake is the transport of the anthropogenic carbon (C_{ant}) from the ocean mixed layer where it is absorbed to the interior ocean where it is stored. While it is generally known that deep water formation sites are important for vertical carbon transport, the exact magnitude of the fluxes across the base of the mixed layer in different regions is uncertain. Here, we determine where, when, and how much C_{ant} has been injected across the mixed-layer base and into the interior ocean since the start of the industrialized era. We do this by combining a transport matrix derived from observations with a time-evolving boundary condition obtained from already published estimates of ocean C_{ant}. Our results show that most of the C_{ant} stored below the mixed layer are injected in the subtropics (40.1%) and the Southern Ocean (36.0%), while the Subpolar North Atlantic has the largest fluxes. The Subpolar North Atlantic is also the most important region for injecting C_{ant} into the deep ocean with 81.6% of the C_{ant} reaching depths greater than 1,000 m. The subtropics, on the other hand, have been the most efficient in transporting C_{ant} across the mixed-layer base per volume of water ventilated. This study shows how the oceanic C_{ant} uptake relies on vertical transports in a few oceanic regions and sheds light on the pathways that fill the ocean C_{ant} reservoir.

1. Introduction

Since the beginning of the industrial era, humankind has emitted large quantities of CO₂ to the atmosphere. This has changed its radiative properties and resulted in global warming. The increased atmospheric CO₂ concentration also drives ocean anthropogenic carbon (C_{ant}) uptake, which mitigates the atmospheric CO₂ rise and consequently global warming. Although oceanic C_{ant} is chemically indistinguishable from the large natural carbon pool of 38 000 Pg C (Sarmiento & Gruber, 2002), the total C_{ant} inventory in the ocean has been constrained to within 15%. Various methods, based on the reconstruction of preindustrial ocean carbon concentrations, tracers, and optimized circulation models agree that the global ocean has absorbed one fourth of the total anthropogenic emissions from fossil fuel combustion, cement manufacturing, and land use change (DeVries, 2014; Khatiwala et al., 2009; McNeil et al., 2003; Sabine et al., 2004), that is, 160 ± 20 Pg C out of 655 ± 55 Pg C (Friedlingstein et al., 2020). These estimates of ocean C_{ant} content and distribution are valuable for understanding climate sensitivity to CO₂ emissions, vulnerability of ocean carbon uptake for further climate change, for quantifying the extent of ocean acidification (Lauvset et al., 2020), as an independent check on estimates of the terrestrial sink of CO₂ (e.g., DeVries, 2014; Khatiwala et al., 2009), and for evaluation of Earth System Models (e.g., Liddicoat et al., 2021).

Ocean C_{ant} uptake is regulated by an interaction of physical and chemical processes (Maier-Reimer & Hasselmann, 1987). The chemical processes control the mass of C_{ant} that can be absorbed into the well-mixed upper ocean for a given rise in atmospheric CO₂ before equilibrium is reached. It is dependent on the water's buffer capacity, formally quantified as the Revelle factor, which expresses the relationship between changes in CO₂ partial pressure (pCO₂) and Dissolved Inorganic Carbon (DIC) (Middelburg et al., 2020). A high Revelle factor means low buffer capacity and relatively low capacity for C_{ant} uptake and vice versa for low Revelle factor. The physical processes control the extent to which waters that have absorbed C_{ant} from the atmosphere are transported away from the well-ventilated upper ocean mixed layer to the deep ocean (Graven et al., 2012; Sarmiento et al., 1992) and replaced with older waters through upwelling. These older waters have not been exposed to the present atmosphere and thus provide the surface ocean with further capacity for C_{ant} uptake. The ocean circulation thus ensures the ongoing absorption of C_{ant} by the subduction of C_{ant} across the mixed layer.

Some features of the C_{ant} subduction across the mixed-layer base are evident from the distribution of C_{ant} in the ocean, in particular, the large column inventories within and immediately downstream of deep and mode water formation regions. These include the North Atlantic, reflecting the C_{ant} transport by the North Atlantic Deep Water (NADW), and the Antarctic convergence and regions to the north of this, reflecting the C_{ant} transport by Antarctic Intermediate Water (AAIW) and Subantarctic Mode Water (SAMW) (Sabine et al., 2004). AAIW and SAMW are collectively referred to as MIW (Mode/Intermediate Water) in the remainder of this contribution. However, inventory estimates do not provide explicit information about these C_{ant} fluxes across the mixed-layer base. Instead, such anthropogenic carbon transports have been determined by combining C_{ant} estimates with geostrophic flow fields (e.g., Alvarez et al., 2003; Holfort et al., 1998; Lundberg & Haugan, 1996; Macdonald et al., 2003; Rosón et al., 2003) and by using data-based inverse methods (Mikaloff-Fletcher et al., 2006). These studies show that the C_{ant} that is taken up in the deep water formation regions in the Subpolar North Atlantic (i.e., Labrador and Nordic Seas) is transported southward by entrainment into the NADW. In the Southern Ocean, about half of the C_{ant} that is absorbed are transported equatorward mostly as a consequence of the spreading of the MIW (Mikaloff-Fletcher et al., 2006). The C_{ant} transported along these pathways is stored below the subtropical gyres, resulting in the high-column inventories observed there.

More sophisticated methods, such as transport matrices (offline ocean circulation models in the form of a matrix), have been used to provide the first 3D estimates of C_{ant} distribution (Khatiwala et al., 2009) and transport (DeVries, 2014; Khatiwala et al., 2013). Khatiwala et al. (2013) and DeVries (2014) used observationally optimized transport matrices to determine ocean C_{ant} uptake, transport, and storage. Their findings largely agree with those determined using the inverse methods described above; the large storage rates in the midlatitude oceans are a consequence of the equatorward flows of C_{ant} rich waters subducted in the Southern Ocean and Subpolar North Atlantic. The results provided by these methods are part of the cornerstones of oceanic C_{ant} studies; however, fluxes across the mixed-layer base were not estimated. Such fluxes across the base of the mixed layer and their spatial distribution have only been explored in models. Bopp et al. (2015) used the NEMO-PISCES model (Aumont & Bopp, 2006; Madec, 2008; Timmerman et al., 2005) to show that global subduction is dominated by the Southern Ocean and the subtropics. The subduction in the Southern Ocean was found to be a result of vertical mixing, while in the subtropics, it is a result of the interplay between the sloping mixed-layer base (horizontal mixed-layer base depth gradients) and lateral advection, including Ekman pumping. At high northern latitudes, vertical mixing was found to drive most of the subduction. Pathways of C_{ant} to the interior ocean were also explored by Iudicone et al. (2016) who applied a thermodynamic water-mass framework to output from the ORCA2-LIM-PISCES model (Aumont & Bopp, 2006; Madec et al., 1998; Timmerman et al., 2005) to identify the importance of various processes, in particular water mass transformation and diffusion, in transporting C_{ant} to the different density levels of the global ocean.

The overall aim here is to provide an observation-based estimate of the fluxes across the base of the mixed layer and the subsequent movement in the interior by identifying the oceanic regions that filled the ocean with C_{ant} over the time period 1780–2012. We do this by combining the Total Matrix Intercomparison (TMI) transport matrix (Gebbie & Huybers, 2012) with estimates of C_{ant} growth rates in the mixed layer, obtained from DeVries (2014). Unlike other transport matrices, the TMI matrix is constrained almost entirely from observations without relying on information from General Circulation Models (Khatiwala et al., 2013) or dynamical constraints (DeVries & Primeau, 2011). By combining a boundary Green's function derived from the TMI transport matrix with the time evolving C_{ant} boundary concentration, we estimate the total amount of C_{ant} injected across the mixed-layer base and into the interior ocean. We also apply a particular focus on deep regions (>1,000 m) both where and when the deep ocean C_{ant} was injected at surface.

2. Methods

C_{ant} behaves as a conservative tracer (Sarmiento et al., 1992), and thus with a representation of ocean circulation and a boundary condition, the ocean transport of C_{ant} can be quantified. Green's functions reproduce the advective-diffusive pathways that connect the ocean surface with the interior and they have been widely used to assess the distribution of C_{ant} in the ocean (e.g., Khatiwala et al., 2009; Waugh et al., 2006). Here, we determine the subduction of C_{ant} across the ocean's mixed layer using the boundary Green's function from Gebbie and Huybers (2012) that encapsulates the ocean circulation and a C_{ant} boundary condition obtained from

DeVries (2014). The cumulative fluxes in each of the mixed-layer patches, $F(s, t)$ (in mol), into the interior ocean locations, i , are given by

$$F(s, t) = \sum_{\tau=0}^{233} \sum_{i=0}^N g(s, i, \tau) c(s, t - \tau) \quad (1)$$

where $g(s, i, \tau)$ represents the boundary propagator from the mixed-layer patch s to each of $N = 57,514$ interior locations below the mixed layer and is here expressed in terms of volume (i.e., in m^3). Overall, the ocean is discretized into a grid with a horizontal resolution of 4° by 4° and 33 vertical levels. The depth of the mixed layer varies regionally, such that the number of vertical levels in the mixed-layer patches (i.e., mixed-layer) also varies regionally. There are altogether 74,064 grid cells with 2,806 mixed-layer patches that contain 16,550 grid cells within the mixed layer (which is completely homogeneous). The boundary propagator g runs with a lag, τ , up to 233 years. The volume that leaves the mixed-layer patch s is combined with the mixed-layer C_{ant} time histories c (in mol m^{-3}) for times $t = 1780\text{--}2012$.

The C_{ant} boundary condition was obtained from the C_{ant} distribution estimated with the Ocean Circulation Inverse Model (OCIM) by DeVries (2014), which provides an appropriate representation of the C_{ant} concentrations by coupling an interactive atmosphere and an ocean transport matrix based on observational and dynamical constrains.

2.1. Boundary Green's Function

Here, we use the boundary Green's function determined by Gebbie and Huybers (2012). This contains the surface pattern of contributions ($g(s, i, \tau)$ in Equation 1) to ocean's interior volume that arrive with a lag of τ time steps. It was determined from modern-day tracer observations by constraining ocean-mixing pathways with the TMI and ventilation rates with ^{14}C . The TMI is a water decomposition method based on the inversion of tracer conservation equations for six ocean properties (potential temperature (θ), salinity, $\delta^{18}\text{O}_{sw}$, PO_4^{3-} , NO_3^- , and O_2) (Gebbie & Huybers, 2010). In essence, by identifying mixtures of water properties, the TMI diagnoses the pathways that connect 57,514 inner ocean boxes with 2,806 mixed-layer patches as explained above. For the ventilation rates, lags up to 2,000 years permit more than 99.9% of ocean's memory to be captured (Gebbie, 2012; Gebbie & Huybers, 2012). The TMI ocean circulation model is also used here as a forward model to estimate the distribution and inventory of C_{ant} in the ocean, which is used to examine model consistency (Section 2.3).

2.2. Mixed-Layer C_{ant} Time History

The time history of C_{ant} in the mixed layer used as boundary condition c was extracted from the time and space resolving the global ocean C_{ant} (control "inversion" (CTL)) estimate published by DeVries (2014), which is based on the OCIM. Briefly, the OCIM is data-constrained dynamical circulation model, optimized by assimilating observations of θ , salinity, ^{14}C and CFC-11, as well as estimates of mean sea surface height and sea surface heat, and freshwater fluxes (DeVries, 2014; DeVries & Primeau, 2011). DeVries (2014) estimated the C_{ant} ocean distribution as the difference in ocean DIC between a time-varying run where the atmospheric $p\text{CO}_2$ increases according to observations and a preindustrial run under a constant preindustrial atmospheric concentration of 280 ppm. He assumed that ocean biology and circulation remained constant since the preindustrial era. The OCIM C_{ant} distribution was supplied on a resolution of 2° by 2° and was interpolated onto the TMI grid (4° by 4°) to enable us to use it as a boundary condition.

2.3. Model Evaluation

To evaluate our approach, we propagate the OCIM mixed-layer C_{ant} concentration throughout the ocean interior. We derive a surface boundary flux f , equivalent to the yearly growth rate of the OCIM mixed-layer C_{ant} time history (c in Equation 1), and then force the TMI ocean circulation model (Section 2.1) according to the equation:

$$\frac{dC_{ant}}{dt} = LC_{ant} + Bf \quad (2)$$

where B is the matrix corresponding to the mixed layer that imposes the surface boundary flux f into the interior ocean transport matrix L (Gebbie & Huybers, 2012). The equation is solved by the timestepping algorithm “ode15s” in MATLAB. The boundary Green's function, the collection of g 's in Equation 1, is self-consistently produced with this method (see Appendix A in Gebbie, 2012). Thus, the extent to which the C_{ant} distribution and inventory determined using Equation 2 align with existing assessments provides insight on the fidelity of our results.

The total ocean C_{ant} inventory determined from the TMI for 2010 is 178 Pg C (Figure 1a). This is close to the recent inventory estimates by Khatiwala et al. (2013) and DeVries (2014) who estimated 155 ± 31 and 155–160 Pg C, respectively. In this study, we focus on the fluxes across the base of the mixed layer, and the reproduction of the inventory provides an insight of the suitability of the circulation model for that purpose. Given that the true size of the ocean carbon inventory is not known, and that our C_{ant} concentration in the mixed layer is not independently constrained, our approach cannot be used to provide an independent estimate of the inventory.

Differences between the TMI column inventory distribution (Figure 1b) and the one presented by DeVries (2014) (Figure 1c) are solely due to differences in circulation. In general, the distribution of C_{ant} derived from the TMI aligns with other estimates (DeVries, 2014; Khatiwala et al., 2013). The Labrador and Nordic Seas contain large amounts of C_{ant} up to 90 mol m^{-2} , while the smallest column inventories are found in the Southern Ocean, south of the Polar Front. This region is dominated by upwelling of old waters from the Antarctic Circumpolar Current with low concentrations of C_{ant} . In the Subpolar and Subtropical North Atlantic, the TMI-derived estimates are about 66% and 69% of the OCIM-derived ones, respectively. Specifically, while the OCIM results show large inventories in the west associated with the Deep Western Boundary Current, this feature is much less strong in the TMI results, indicating more diffusive transports in the latter. The largest disagreement in terms of total inventory occurs in the tropical Pacific, where, when integrated over the large volume of the basin, the slightly higher concentrations in the TMI amount to a difference of 10.8 Pg C (Figure 1d). The column inventories in the Arctic are slightly higher likely as a consequence of poor constraints on its circulation rates due to the dearth of ^{14}C data from this region at the time the TMI analyses were carried out (Gebbie & Huybers, 2012).

The zonally integrated cross sections (Figure 2) shed light on which water masses contribute most to these differences. The deepest penetration of C_{ant} comes from the NADW in the North Atlantic due to the contributions of the Labrador Sea Water (LSW; $\sim 1,000 \text{ m}$ north of 40°N) and the deep convection in the Nordic Seas (north of 60°N) that transport C_{ant} concentrations of $\sim 30 \text{ } \mu\text{mol kg}^{-1}$. In the Atlantic, Pacific, and Indian Ocean basins, the Southern Hemisphere MIW propagates C_{ant} down to 1,000 m and northward, resulting in high concentrations in the main thermocline below the subtropical gyres. The largest disagreement with the OCIM, up to $20 \text{ } \mu\text{mol kg}^{-1}$ less, appears throughout the North Atlantic water column between 30 and 50°N and is the deep expression of the differences in the Deep Western Boundary Current discussed above. Further, concentrations in the deep Nordic Seas are at least $15 \text{ } \mu\text{mol kg}^{-1}$ larger in the TMI than in the OCIM. We note, however, that the TMI-derived Nordic Seas inventory of $\sim 70 \text{ mol m}^{-2}$ and $\sim 1.3 \text{ Pg C}$ for 2002 (not shown) agrees with previous estimates of $\sim 70 \text{ mol m}^{-2}$ and $0.9\text{--}1.4 \text{ Pg C}$ (Olsen et al., 2010) for the same year, whereas the OCIM estimate is $\sim 60 \text{ mol m}^{-2}$ and about 1.2 Pg C , which renders confidence to the TMI approach here. In the equatorial thermocline in all ocean basins, the concentrations are about $20 \text{ } \mu\text{mol kg}^{-1}$ higher in the TMI-derived estimates.

The difference between the TMI and OCIM C_{ant} inventory results from the differences in the circulation field partially due to the different set of ocean tracers used to constrain the mixing pathways and ventilation rates in the OCIM and TMI. First, the rates in the OCIM are constrained by CFC-11 and ^{14}C , while the TMI only uses ^{14}C . Due to its long half-life (5,730 years), ^{14}C data are suitable to resolve ventilation rates on a long timescale, whereas CFCs, being much more modern, resolve decadal to multidecadal timescales (England & Maier-Reimer, 2001). This long half-life likely results in the concentration differences in the North Atlantic, which we believe are more trustworthy in the OCIM. The Deep Western Boundary Current is sharp in the OCIM, while it appears more diffuse in the TMI likely due to the dependency of the ^{14}C alone that might not be sufficient to resolve the near-present circulation in the latter. Second, the additional nutrient and oxygen tracers in the TMI could constrain uncertain biogeochemical fluxes (DeVries & Primeau, 2011; Schlitzer, 2004). In the equatorial regions, the TMI accumulates more C_{ant} than the OCIM: about $10 \text{ } \mu\text{mol kg}^{-1}$ in the thermocline. PO_4^{3-} is among the tracers used to derive the pathways in the TMI, and the TMI corrects for remineralization under the assumption that the Anderson and Sarmiento (1994) stoichiometric ratios, 1:-170 P:O₂, apply. Recently, Carter et al. (2021) determined that this ratio is likely smaller, $1\text{--}141 \pm 12$. The fixed stoichiometric ratios or

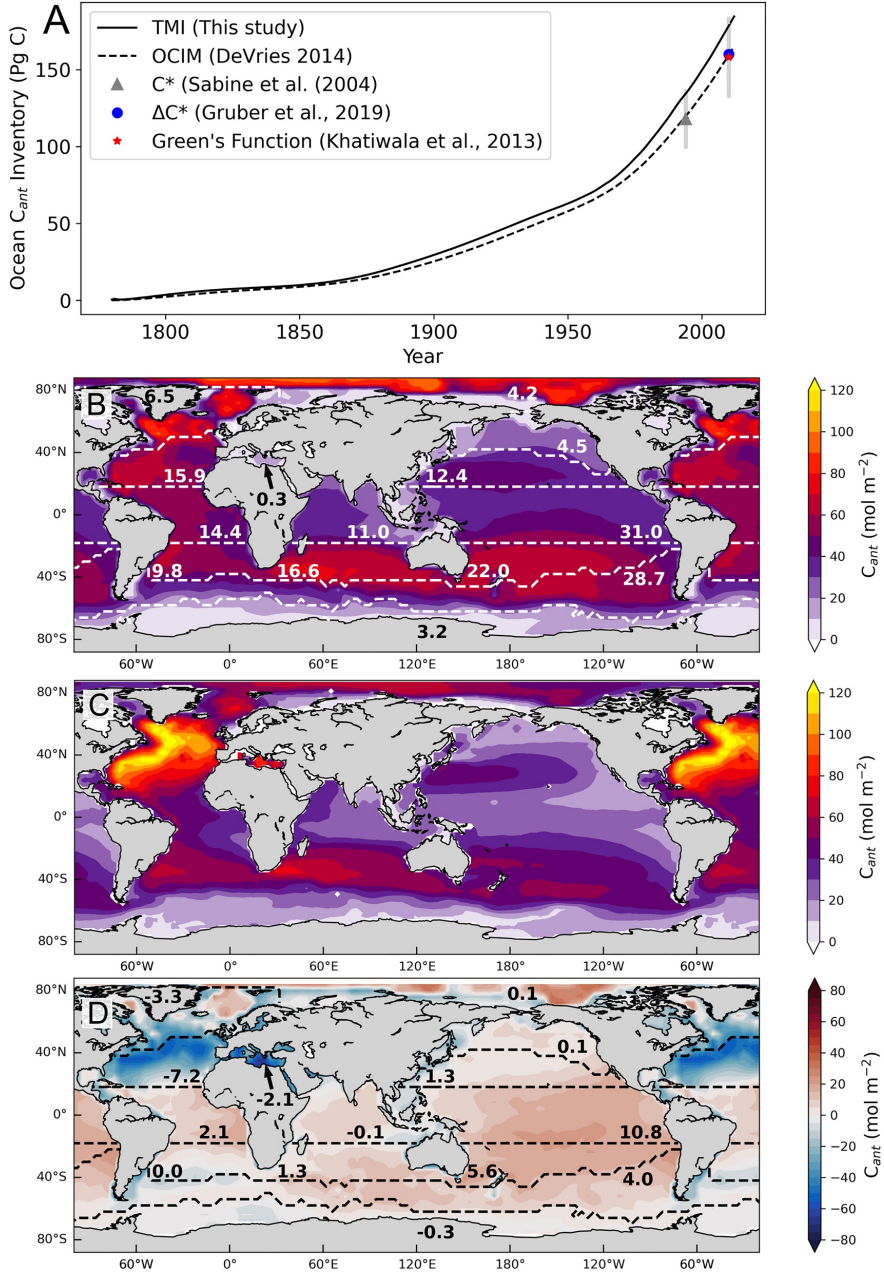


Figure 1.

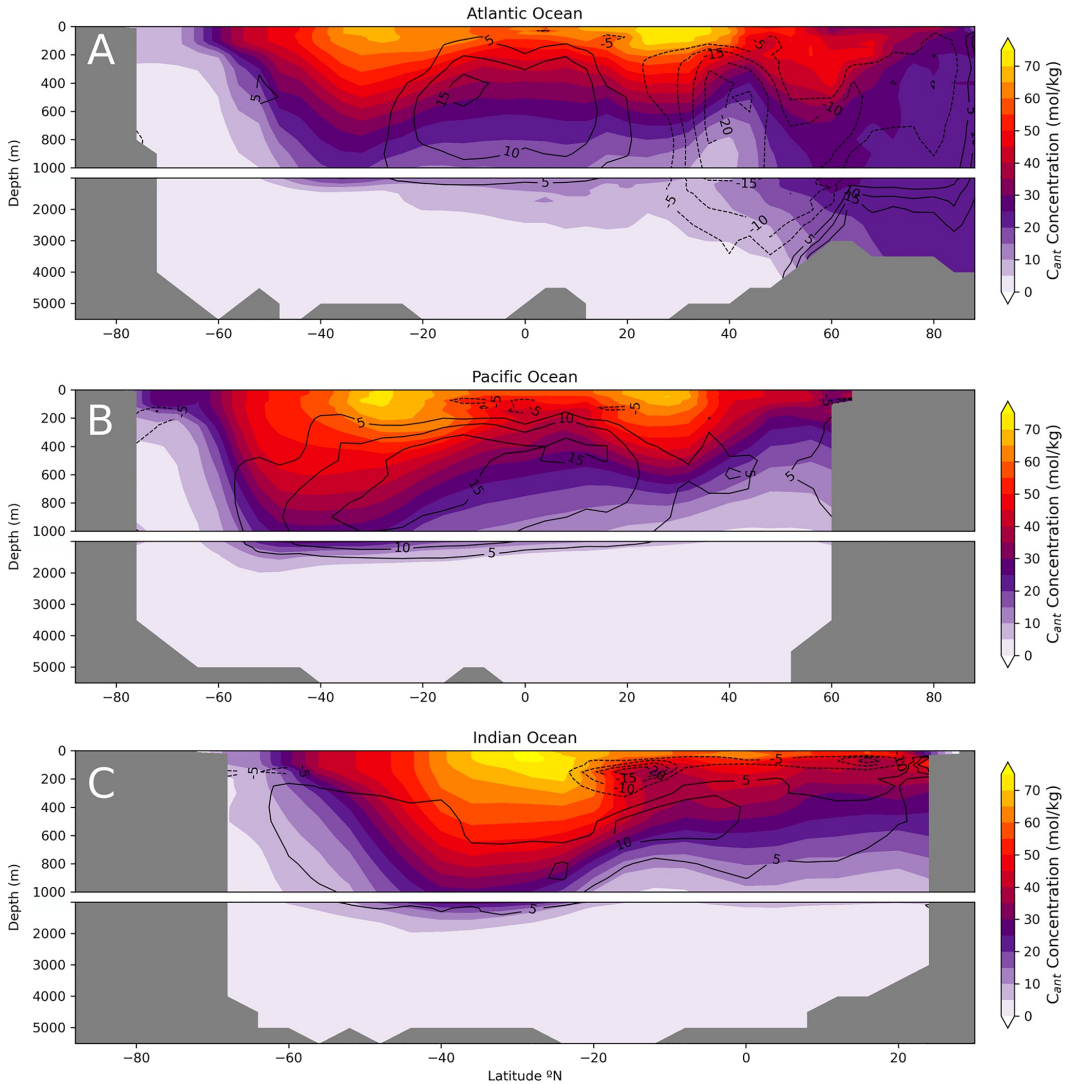


Figure 2. Vertical distribution of C_{anti} , zonally averaged, for (a) Atlantic, (b) Pacific, and (c) Indian Ocean for 2010. Black contours indicate the differences with Ocean Circulation Inverse Model (OCIM) for 2010 calculated as Total Matrix Intercomparison (TMI) minus OCIM, where solid lines mean higher and dashed lines lower concentrations in the TMI. The missing Greenland-Scotland Ridge in the Atlantic (60°N) is an artifact of the longitudinal averaging across the entire basin. Note difference in y axis (depth) scaling between 0–1,000 m and 1,000–5,000 m.

Figure 1. (a) C_{anti} inventory evolution produced by the Total Matrix Intercomparison (TMI) for 1780–2012 and estimates from the C^* method by Sabine et al. (2004), Green's Function by Khatiwala et al. (2009), ΔC^* by Gruber et al. (2019), and Ocean Circulation Inverse Model (OCIM) by DeVries (2014). (b) C_{anti} column inventory produced by the TMI for 2010. (c) C_{anti} column inventory produced by the OCIM control “inversion” for 2010 (DeVries, 2014). (d) Differences between the OCIM and the TMI column inventory estimates for 2010 calculated as TMI minus OCIM; blue colors indicate lower and red higher inventories in the TMI. The OCIM field was interpolated onto the TMI grid. Dashed lines represent the outcrop areas of different water masses according to Gebbie and Huybers (2010). The values within each region indicate the total mass of C_{anti} .

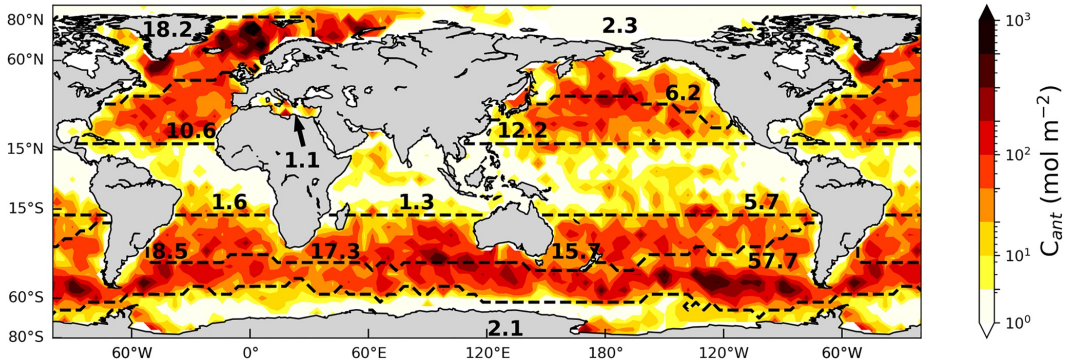


Figure 3. Cumulative C_{ant} fluxes across the mixed-layer base for 1780–2012 from the boundary Green's function and C_{ant} boundary condition. Black-dashed lines define the various regions mentioned in the text and in Table 1, while the numbers indicate the total mass of C_{ant} injected within each region, in Pg C. The color scale is logarithmic.

Table 1
Regional Injection and Inventory Below the Mixed Layer for 2012 in Pg C

Region	Injection	Inventory
Arctic Ocean	2.3	4.2 (4.3)
Atlantic Ocean	49.8	41.9 (52.5)
Labrador Sea	7.1	4.1 (5.2)
Nordic Seas	11.1	1.3 (1.6)
North Subtropical Atlantic	10.6	14.6 (16.4)
South Subtropical Atlantic	8.5	8.9 (10.1)
Tropical Atlantic	1.6	14.0 (14.9)
Subantarctic Atlantic	10.9	3.4 (4.3)
Pacific Ocean	77.7	80.6 (91.8)
Subpolar North Pacific	6.2	3.9 (4.6)
North Subtropical Pacific	12.2	11.2 (12.8)
South Subtropical Pacific	15.7	20.1 (22.7)
Tropical Pacific	5.7	29.5 (32.1)
Subantarctic Pacific	37.9	15.9 (19.6)
Indian Ocean	25.5	30.1 (34.3)
Subtropical Indian	15.3	15.3 (17.1)
Tropical Indian	1.3	10.3 (11.4)
Subantarctic Indian	8.9	4.5 (5.8)
Mediterranean Sea	1.1	0.3 (0.4)
Antarctic Marginal Seas	2.1	2.4 (3.3)
Weddell Sea	0.7	0.5 (0.8)
Ross Sea	0.9	0.9 (1.3)
Adélie Region	0.5	1.0 (1.2)

Note. The numbers in parenthesis correspond to the regional inventory when the mixed layer is included. Regions in bold represent the sum of the sub-regions listed below. Rounding errors account for the mismatch between the estimates in the text.

the inclusion of oxygen to further constrain the circulation in the TMI could contribute to the differences in C_{ant} concentration in the equatorial regions. In particular, a deeper ventilation of those regions could be translated to a higher C_{ant} concentration in the TMI relative to that in OCIM.

Although there are some regional differences among the OCIM and TMI circulation fields, the two matrices are broadly consistent. Carter et al. (2021) compared the surface contributions to a point at the base of the Northern Pacific Subtropical gyre thermocline for the TMI and OCIM in addition to the 2.8° transport matrix from Khatiwala (2007). Despite regional differences, the three matrices show a similar pattern (Figure 1 in Carter et al., 2021). We also note here that the OCIM and the TMI provide similar age estimates for deep and bottom waters (>2,000 m) (DeVries & Primeau, 2011; Gebbie & Huybers, 2012).

3. Results

3.1. C_{ant} Injection

The accumulated flux of C_{ant} across the mixed-layer base in each grid cell from the industrial revolution through 2012 was calculated using Equation 1 (Figure 3). Table 1 summarizes the total injection and inventory in the set of ocean areas defined by Gebbie and Huybers (2010) with additional separation into tropical and subtropical regions at 18° north and south. Of the total ocean inventory of 184.5 Pg C in 2012, 24.3 Pg C remains within the mixed layer, while 160.2 Pg has been injected across the base of the mixed layer. The accumulated injection is largest in deep water formation areas with the strongest flux in the Subpolar North Atlantic (NADW formation region) and Southern Ocean (MIW formation region). Despite its relatively small area (4.2% of the global ocean), the total mass of carbon injected in the Subpolar North Atlantic is 18.2 Pg C (11.3% out of the 160.2 Pg C global total below the mixed layer). 7.1 Pg C (4.4%) of this was injected in the Labrador Sea (including the Irminger Sea and Canadian Archipelago) and 11.1 Pg C (6.9%) in the Nordic Seas. On the other hand, despite being important deep water formation regions with intense fluxes (Figure 3), the Ross and Weddell Seas have contributed with only 1.6 Pg C (1.0%) to the interior ocean inventory.

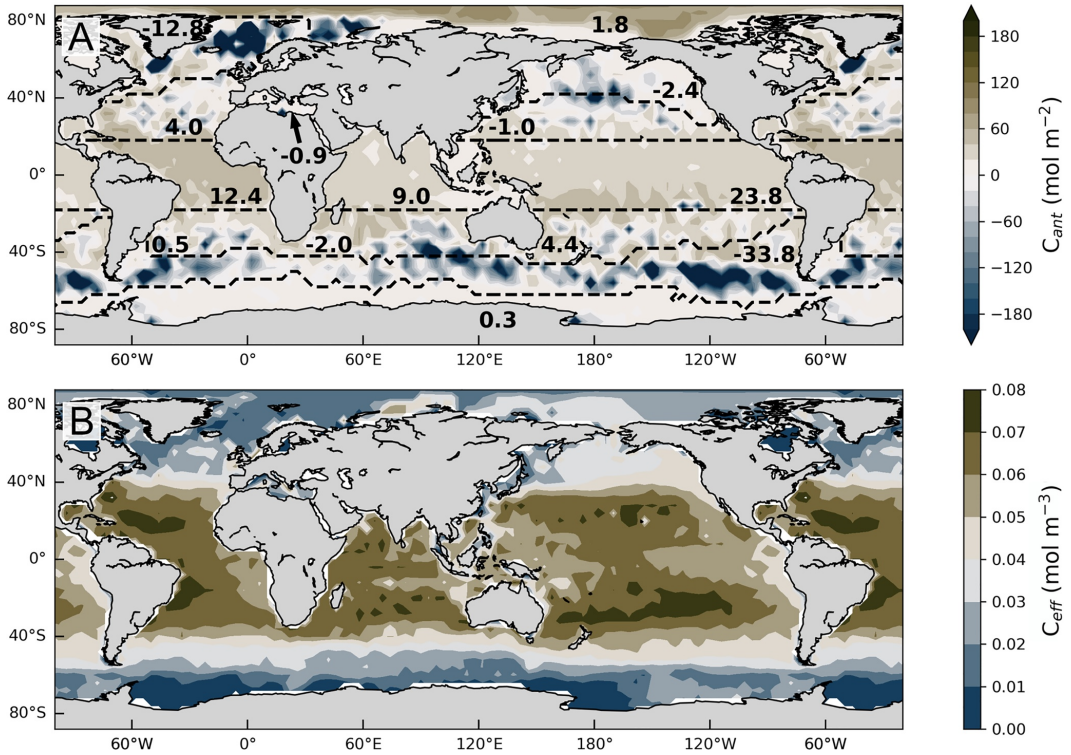


Figure 4. (a) The difference between the inventory below the mixed layer and the cumulative fluxes across. Positive values reflect a convergence of C_{ami} , while negative values reflect a divergence in the ocean interior. The values indicate the net balance of C_{ami} per region in Pg C. (b) Effective C_{ami} end-member concentration, $C_{eff}(s,t)$, for the waters now residing in the interior ocean, calculated from Equation 3.

The fluxes are also substantial in subtropical regions as a consequence of Subtropical Mode Water (STMW) formation in the subtropical gyres. The fluxes are lowest in tropical regions because of strong stratification and/or upwelling; only 8.6 Pg C (5.4%) has been injected in such regions when summed over the three oceans. Integrated over regions, most of the carbon have been injected in the subtropics (64.3 Pg C or 40.1% of the total injection across the mixed layer) and in the subantarctic region of the Southern Ocean (57.7 Pg C or 36.0%).

The difference between the regional injection and the regional inventory below the mixed layer (Table 1 and Figure 4a) reflects the interior oceanic transport of C_{ami} . The areas where the amount of injected C_{ami} is higher than the inventory correspond to regions of C_{ami} divergence, whereas the areas where the inventory is larger than the injection are regions of C_{ami} convergence. The Nordic Seas is the region that exports most carbon relative to the injected amount (88.3%). Other areas of strong divergence are the subantarctic region (58.6%), the Labrador Sea (42.3%), as well as the Subpolar North Pacific (38.7%). The C_{ami} exported from these regions ends up mostly in the tropics, where about one third of the ocean interior C_{ami} reservoir is found. Here, the C_{ami} that is imported from other regions is 5.3 times the amount injected locally.

The relative importance of high-latitude deep water formation areas for filling the inner ocean C_{ami} reservoir has been much smaller than what one would expect from their importance for water volume itself. For instance, while the ratio of water volume injected in the subpolar North Atlantic to the volume injected in the subtropical and tropical Atlantic is approximately 25:3 (Gebbie & Huybers, 2010), the same ratio for C_{ami} is closer to 1:1 (18.2:20.7, Figure 3). This can be understood when considering that most of the waters from the subtropics and tropics now present in the ocean are much younger and had higher concentrations of C_{ami} when they were injected

than most of the waters from the high-latitude north Atlantic or Southern Ocean as their resurfacing timescales are much shorter (Primeau & Holzer, 2006). This resurfacing is not explicitly modeled with our approach, but its impacts are included via the age associated with the different water masses. Deep waters from high latitudes remain in the interior ocean on millennial timescales (Primeau & Holzer, 2006) and therefore have higher overall ages. This means they brought with them lower C_{ant} per volume of water formed compared to water injected in the subtropics and tropics, which have much shorter residence times in the interior ocean as they resurface faster and are overall younger. We illustrate this effect by calculating effective C_{ant} end-member concentrations:

$$C_{eff}(s, t) = \frac{F(s, t)}{\sum_{\tau=0}^{233} \sum_{i=0}^N g(s, i, \tau)} \quad (3)$$

where the denominator is in effect the total volume of water injected from the mixed-layer patch s over the industrial era (last 233 years) that has not yet been recycled to the mixed layer, and the numerator is the total mass of C_{ant} injected as calculated by Equation 1. C_{eff} is on average 2.3 times higher in the subtropics and subtropics than at high latitudes and up to 4 times higher in individual grid cells (Figure 4b). From the Revelle factor alone, one expects a much smaller concentration gradient and the surface C_{ant} saturation concentration is only 1.2 times higher in the tropics and subtropics than at high latitudes (Figure S1 in Supporting Information S1). The larger C_{ant} undersaturation at high latitudes, likely caused by deep mixing that brings low C_{ant} waters to the surface, increases this to 1.5 (Figure S1 in Supporting Information S1). Thus, most of the regional differences in C_{eff} are explained by the young ages of waters injected in the tropics and subtropics compared to the high latitudes, which made the injection of C_{ant} per cubic meter more efficient. The spatial pattern of effective C_{ant} boundary condition is broadly opposite to the cumulative flux pattern (Figure 3). The largest cumulative fluxes are, however, associated with deep and mode water formation areas, suggesting that the ventilation and mean residence time of the waters in the ocean interior are the rate limiting factor for the ocean carbon uptake.

3.2. Deep Injection

Ocean-based Carbon Dioxide Removal strategies, such as injection of CO_2 in the ocean by various means, have been proposed to achieve negative emissions, and 1,000 m has been previously used as an approximation for the depth at which C_{ant} can be sequestered for centennial timescales (Passow & Carlson, 2012), and while this is approximately correct, the actual sequestration timescale varies regionally (Primeau, 2005; Siegel et al., 2021). Here, we therefore set a uniform boundary at 1,000 m to separate the intermediate ocean reservoirs of C_{ant} of 142.2 Pg C (77.1%) and the deep reservoir of 42.3 Pg C (22.9%) for 2012. Our results provide broad insight into which surface regions contribute to the C_{ant} stored below 1,000 m and therefore, a large part of the C_{ant} stored for approximately centennial timescales.

Not every region has the same role in filling the deep ocean. By modifying the selection of interior points i in Equation 1, we can determine where C_{ant} stored in any particular part of the global ocean was subducted out of the mixed layer (Figure 5). The largest of such fluxes are found in the Subpolar North Atlantic, where altogether 14.9 Pg C has been injected deeper than 1,000 m, as associated with the formation of NADW. This is 81.9% of the C_{ant} injected across the mixed-layer base in this region, meaning that most of the carbon injected there end up at more than 1,000 m depth. The subantarctic region is the other main injection region where, by the formation of MIW, 19.4 Pg C are injected (45.9% of the total injection to levels deeper than 1,000 m). The STMW in the subtropical gyres contributes to only 6.2 Pg C to the deep ocean, a much smaller fraction (14.7% of the total injection below 1,000 m). In the Mediterranean Sea, 0.8 Pg C are injected below 1,000 m, almost three quarters of the total C_{ant} injected in this region, by means of the Mediterranean Overflow waters that enter the North Atlantic at ~1,000 m depth (Aldama-Campino & DÖös, 2020).

The C_{ant} stored in the deep Atlantic and Arctic (Atlantic-Arctic), Pacific, Indian, and Southern oceans mostly originates from high latitudes (Figures 6b–6e). The deep Atlantic (Figure 6b) has accumulated 18.1 Pg C, and most of it was injected in the Nordic Seas (8.5 Pg C) and the Labrador Sea (4.5 Pg C). The deep Pacific (Figure 6c) stores 12.3 Pg C_{ant} , and a large part (8.2 Pg C) was injected in the subantarctic region with the MIW formed there. Some (0.6 Pg C) has also been injected in the North Pacific with the formation of North Pacific Intermediate Water. In addition, both the Subpolar North Atlantic and the Arctic contribute to the deep Pacific C_{ant} inventory (0.3 and 0.2 Pg C). The deep Indian (Figure 6d) ocean C_{ant} reservoir has been filled similarly. It stores 4.5 Pg C

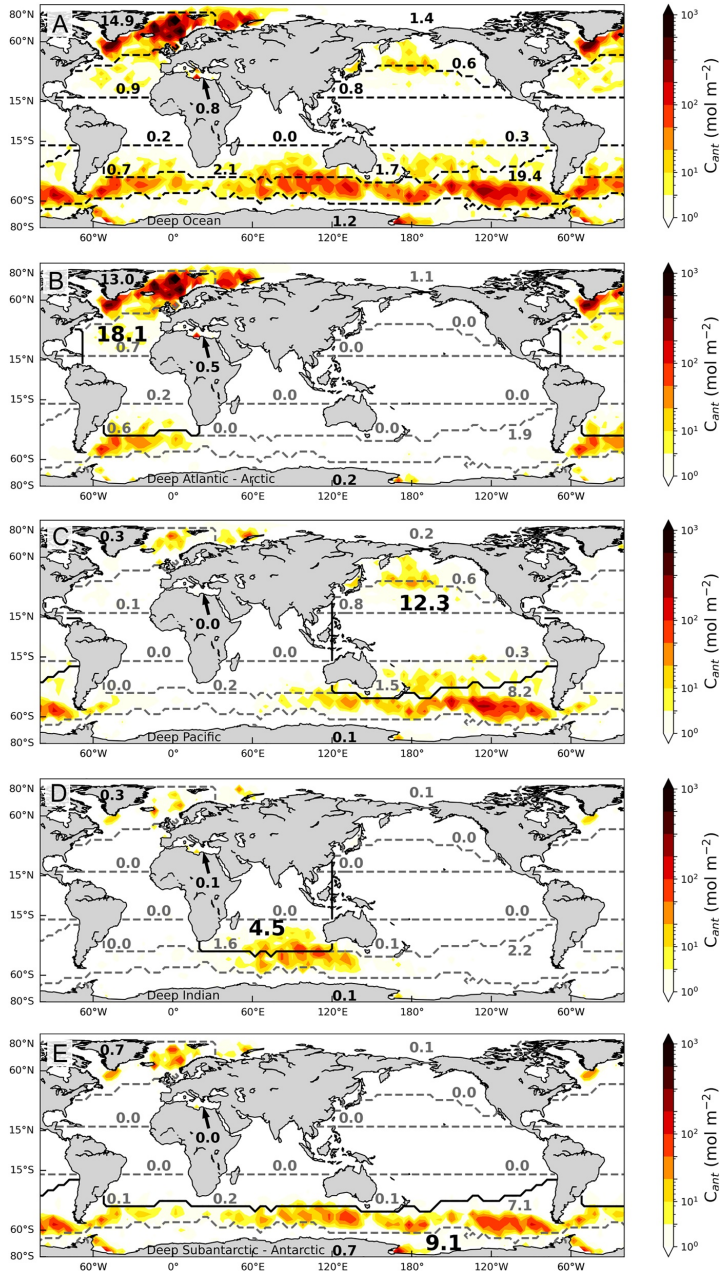


Figure 5. Same as Figure 3 but for (a) C_{ami} fluxes into the deep ocean (>1,000 m) and (b–e) the deep reservoirs of major oceanic regions. For (b–e): The solid black line marks the horizontal limit of the respective deep reservoir and the number in black indicates the total mass of C_{ami} stored within the reservoir in Pg C. Colors show the fluxes across the mixed layer, where gray-dashed lines delimit the surface injection regions and gray numbers give the total mass of C_{ami} injected within each of these regions (in Pg C). The color scales are logarithmic. Numbers for total mass are consistent with each other within rounding errors.

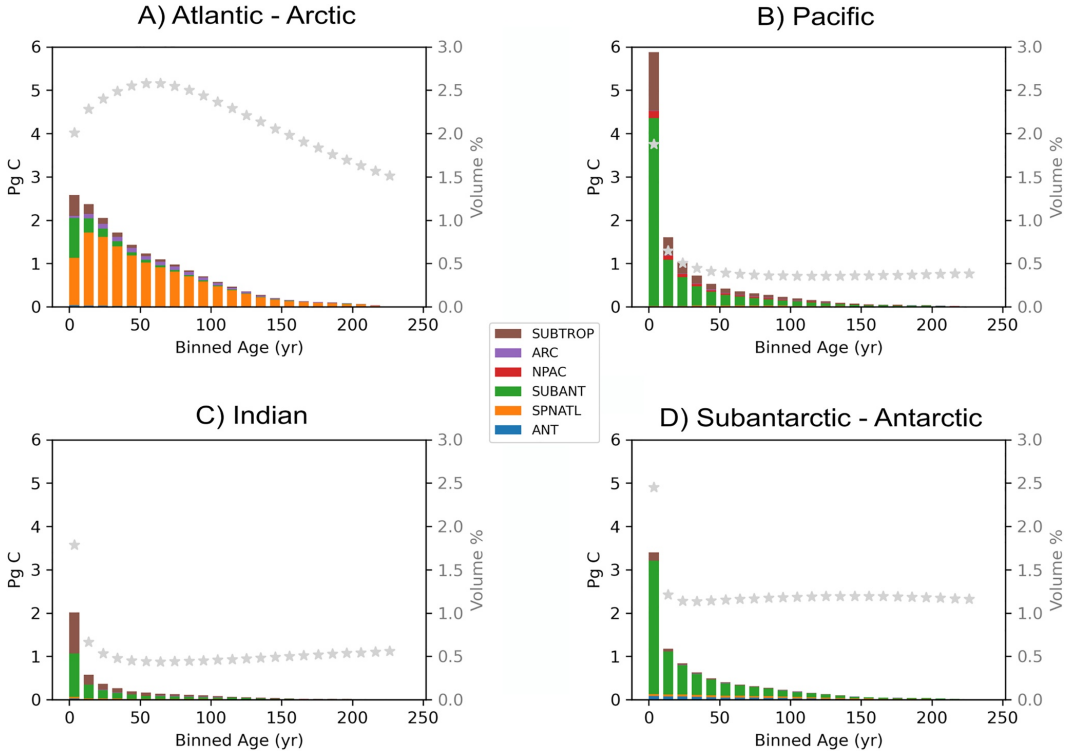


Figure 6. Age distribution of C_{ami} below 1,000 m for 2012 in the major ocean regions considered here, showing where and when the C_{ami} stored in the deep (a) Atlantic (including the Arctic), (b) Pacific, (c) Indian, and (d) Antarctic was injected across the mixed layer. The different colors refer to the region of injection: ANT (Antarctic), SPNATL (Subpolar North Atlantic), SUBANT (Subantarctic), NPAC (North Pacific), and ARC (Arctic). Gray stars indicate the water-age distribution as volume percentage of the entire reservoir for each age class for the last 233 years. The age distribution was binned every 10 years.

of which a third (1.6 Pg C) was injected locally but the main fraction has been transported from the subantarctic region through the subduction with MIW (2.2 Pg C). The Subpolar North Atlantic also contributes to the deep Indian Ocean C_{ami} reservoir (0.3 Pg C). The deep Subantarctic-Antarctic (Figure 6e) stores 9.1 Pg C of which most (7.1 Pg C) were injected north of the Polar Front by the MIW. Antarctic Bottom Water (AABW) from the Ross and Weddell Seas have relatively minor contributions to the deep C_{ami} stored in this reservoir, 0.4 and 0.3 Pg C, respectively. The Subpolar North Atlantic contributes also with 0.7 Pg C through the southward transport of NADW. Overall, these results highlight how the deep, long-term, C_{ami} storage in the ocean relies on a few key regions.

For each of the pathways that connect a subduction region to a long-term reservoir, there is an associated water-age distribution, which is equivalent to the boundary Green's function. How long it takes for each of the deep reservoirs to be filled is, essentially, the age distribution of C_{ami} below 1,000 m in the oceanic region in question (Figure 6). This distribution results from the convolution of the water-age distribution and the C_{ami} concentration at the time of subduction (i.e., the boundary condition). The C_{ami} -age distribution is calculated by removing the temporal summation in Equation 1 and selecting the interior points i within the deep reservoir R :

$$F(t, \tau) = \sum_{s=0}^{2806} \sum_{i=0}^N g(s, i, \tau) c(s, t - \tau) \quad \text{where } i \in R. \quad (4)$$

The C_{ant} -age distributions (Figures 6a–6d) show that young C_{ant} predominates in all deep reservoirs. The lower amount of C_{ant} at the tail end of the distribution reflects the smaller C_{ant} concentration in waters ventilated at the beginning of the industrial era. In the deep Atlantic-Arctic, the C_{ant} is older than in the rest of the deep reservoirs. This is a consequence of the presence of large fractions of water at older ages in the Atlantic-Arctic region; about 50% of the reservoir has been ventilated during the industrial period up to $\sim 2.5\%$ for each 10-year interval shown (Figure 6a). Such large ventilated water volume, combined with the appreciable amount of C_{ant} present in the atmosphere at the time they were ventilated, leads to quite high concentrations of C_{ant} (not shown). Even if the volume fraction of waters at ages 40 to ~ 100 years is large, these waters contribute less to the C_{ant} inventory because of their smaller C_{ant} concentrations. In the deep Pacific, Indian, and Subantarctic-Antarctic oceans, waters ventilated in the industrial era constitute only a small part of the total volume (10.6%, 12.9%, and 28.7%, respectively) (see longer age spectra in Figure S2 in Supporting Information S1). The volume fraction of waters younger than 10 years is relatively large, likely resulting from the vigorous ventilation of the MIW. The combination of large volume fraction and high C_{ant} concentrations in these recent waters results in a strong peak of C_{ant} for the 10-year age class. For the rest of the industrial period, the various age classes in the Pacific and Indian contribute quite equally to volume, about 0.5% for each 10-year interval. Counterintuitively, the smaller amount of C_{ant} present in the deep Pacific and Indian oceans is thus younger than the large amounts present in the deep Atlantic-Arctic. In the Pacific and Indian oceans, C_{ant} has entered primarily from ventilation of the thermocline in the subtropics (SUBTROP contribution in Figure 6) and with MIW from the subantarctic (SUBANT).

4. Discussion

4.1. Comparison With Other Estimates

The C_{ant} injection calculated here represents the cumulative fluxes across the mixed-layer base and is comparable to the annual fluxes determined by Bopp et al. (2015). Their modeling approach and the observationally derived Green's function approach presented here provide consistent results. Overall, the studies agree that substantial amounts of C_{ant} are injected in the subtropical gyres and in the Southern Ocean, while they disagree in the Subpolar North Atlantic. In both studies, the subtropics inject the highest amount of C_{ant} . The injection across the mixed-layer base in the Southern Ocean as derived from the Green's function is 31.3% (57.7 Pg C) of the total ocean inventory of 184.5 Pg C, whereas in Bopp et al. (2015), 0.74 Pg C yr⁻¹ are injected, corresponding to 32.5% of their annual mean global uptake over 1998–2007. The injection north of 49°N is, in our case, substantially higher than the 5.7% of the yearly uptake from Bopp et al. (2015) at 14.3% (26.4 Pg C) of the total inventory, and the difference is mainly associated with the Labrador and Nordic Seas.

Bopp et al. (2015) pointed out that their modeled inventory in the North Atlantic was slightly underestimated and therefore, it is possible that the vertical transports were also underestimated. Some models struggle to represent the small-scale processes involved in deep water formation in the Subpolar North Atlantic (Heuzé, 2017, 2021), such that weak mixing and ventilation results in a lower C_{ant} uptake (Wang et al., 2012). The NEMO-PISCES model used by Bopp et al. (2015) is based on the OPA ocean circulation model (Madec, 2008) and the LIM2 ice model (Timmerman et al., 2005). These are shared by the ocean/sea-ice model used at NOCS (National Oceanography Centre Southampton), which showed one of the shallowest March mean mixed-layer depths among the models compared by Danabasoglu et al. (2014). Shallower mixed-layer depths were correlated with a weak Atlantic Meridional Overturning Circulation (AMOC) (Danabasoglu et al., 2014), which translates into smaller transport of C_{ant} to depths below 1,000 m (Goris et al., 2018). Furthermore, the NEMO-PISCES model has been shown to misrepresent the Nordic Seas Overflow and underestimate its C_{ant} transport (Racapé et al., 2018). In general, there is an ongoing discussion on how accurately the models represent the deep water formation in the North Atlantic (Menary et al., 2020) and thus the C_{ant} transports. Our approach, based on the TMI model, provides a validation data set by empirically fitting modern observations. As a result, the TMI better captures the higher C_{ant} concentrations in NADW compared to some coarse-resolution models; yet, these are lower than in other observation-based models (DeVries, 2014; Gruber et al., 2019).

Our results suggest that the downward transports of C_{ant} in the Nordic Seas are 1.6 times larger than in the Labrador Sea (Table 1). Such a dominant role of the Nordic Seas agrees with recent observations of the contribution of these regions to the lower limb of the AMOC across the OSNAP (Overturning in the Subpolar North Atlantic Program) current meter array located in the Subpolar North Atlantic and presented by Lozier et al. (2019). Specifically, they found that the contribution from the Labrador Sea (through the OSNAP-West array) to the overturning

circulation (2.1 ± 0.3 Sv) was substantially smaller than the contribution from the Nordic Seas, Irminger Sea, and Iceland basin (15.6 ± 0.8 Sv through the OSNAP-East array) over late 2014 through spring 2016. For a more specific comparison, we estimated the subduction rates of volume north of OSNAP-West and north of OSNAP-East by integrating volume contributions from the Green's function over time as in Primeau and Holzer (2006). Our calculated subduction rates of 2.6 Sv north of OSNAP-West and 12.6 Sv north of OSNAP-East agree well with the direct current measurements presented by Lozier et al. (2019). This renders confidence to our results and further suggests that a dominance of northeastern sources to the lower limb is a persistent feature of the AMOC as the TMI analyses were conducted using climatological data and the assumption of a statistical steady state. We further determined the contribution from the Nordic Seas across the Greenland-Scotland Ridge to 8.1 Sv in the Green's function, which is in excellent agreement with the transport estimate by Østerhus et al. (2019) of 7.8 ± 1.9 Sv and by Chafik and Rossby (2019) of 6.87 Sv. A more direct evaluation of our estimated C_{ant} export from the Nordic Seas is possible by comparing to the C_{ant} budget from Jeansson et al. (2011). They reported that $0.09 \text{ Pg C yr}^{-1}$ of C_{ant} were transported southward by the overflow waters across the Greenland-Scotland Ridge in 2002. This transport represents 4.5% of the global air-sea CO_2 flux for 2002, which agrees extremely well with the 4.2% (7.8 Pg C) export relative to the global C_{ant} inventory found in our study.

Our results show that the Southern Ocean has injected 31.3% of the total inventory of C_{ant} across the mixed layer, consistent with its widely recognized key role for the downward transports of C_{ant} . In comparison, Sallée et al. (2012) suggested in their observation-based regional study that these fluxes are about 20% (south of 35°S) of the global annual air-sea C_{ant} flux of $2.0 \pm 0.6 \text{ Pg C}$ (Friedlingstein et al., 2020). One can also consider the regional air-sea flux of C_{ant} as the upper limit for the injection across the mixed layer in the Southern Ocean, given the limited advection of C_{ant} with surface waters into this region. Several studies agree that the Southern Ocean C_{ant} uptake corresponds to 30%–40% of the global uptake (DeVries, 2014; Frölicher et al., 2015; Gruber et al., 2018; Khatiwala et al., 2013; Mikaloff-Fletcher et al., 2006; Sallée et al., 2012). Because of the large volumes of MIW and AABW water that is formed, one can expect that most of the transport in the Southern Ocean occur below the mixed layer and therefore the injection estimates do not fall far from the uptake. Thus, our estimate (31.3%) falls between the upper limit determined by the air-sea C_{ant} fluxes and the observed 20% (Sallée et al., 2012). We finally note that our estimate is fully consistent with the 32.5% modeled by Bopp et al. (2015).

The agreement with other estimates strengthens our confidence in the results and we believe that the differences in the ocean circulation between the TMI and OCIM, which result in differences in total inventory (Figure 1d), have a small impact on the general pattern of the fluxes through the mixed layer. In the North Atlantic, differences resulting from circulation (Section 2.3) suggest that the injection estimates as derived from the Green's function are lower in the Subpolar North Atlantic than in the OCIM. Similarly, the positive differences in the equatorial thermocline suggest a slightly higher injection in the subtropics in the Green's function estimates. Another aspect to bear in mind is that the ocean circulation and biogeochemistry are considered steady state (i.e., time invariant), which is a common assumption in transport matrices. Model simulations show that the global impact of these assumptions is small. Changes in circulation lead to an uncertainty in the total inventory of less than 1% or 4% when also accounting for variations in biogeochemistry (Wang et al., 2012). Regionally, however, errors in C_{ant} estimates derived from steady-state transport matrices associated with lack of representation of circulation changes are of the same order of magnitude as errors in data-based estimates (Khatiwala et al., 2013). Recent observational studies indicate that decadal changes in circulation do occur and that this affects both the transport and distribution of C_{ant} (DeVries et al., 2017; Gruber et al., 2019), which would impact both the pattern and intensity of C_{ant} injection. Therefore, the results presented in this study should be considered and interpreted in a climatological sense.

4.2. Climate Sensitivity Timescales

Because each of the pathways that connect a subduction region to a long-term reservoir has an associated transit time (Figure 6), we are able to infer where and over what timescales a change in surface anthropogenic carbon uptake will be detectable in the deep (>1,000 m) reservoirs. We refer to this as climate sensitivity timescales. The transit times vary spatially; thus, the climate sensitivity timescales are specific to each of the injection regions. For example, under current atmospheric CO_2 growth rates, the response in C_{ant} storage for a change in the surface forcing in the Subpolar North Atlantic will be strongest after 20 years in the Atlantic-Arctic reservoir (Orange bars in Figure 6a), but the signal would be weakened and lost by the time it reaches the rest of the reservoirs as a

consequence of extensive diffusion along the way (Primeau, 2005). On the other hand, a change in the forcing in the subantarctic region would strongly impact the C_{ant} storage in the deep Pacific, Indian, and Subantarctic-Arctic reservoirs within a decade, given that the C_{ant} -age distribution is biased young and the small size of the inventory there. We note, however, that the relative importance of the short-term signal might decrease as these reservoirs fill. The region contaminated with C_{ant} , or ventilated during the industrial era, amounts to a very small fraction of the entire reservoirs (Figure 6) as the waters deeper than 1,000 m in North Pacific are mostly ventilated by the AABW at millennial timescales (Holzer et al., 2021).

5. Summary

The TMI and its derived Green's function, built using observations of ocean tracers, have allowed us to investigate how the ocean anthropogenic carbon reservoir has been filled. By following the mixing pathways that connect any ocean interior point with the surface, we determined where and when C_{ant} was injected across the mixed-layer base and into the interior ocean from the beginning of the industrial era through 2012.

Most of the C_{ant} currently stored in the ocean interior were injected in high-latitude mode and deep water formation regions and in the subtropics. The Southern Ocean is the main injection region, where about one third of the C_{ant} stored in the interior ocean crossed the mixed layer carried by the MIW (Mode and Intermediate Waters: SAMW and AAIW). Other important injection regions are the subtropics through the STMW formation and the Subpolar North Atlantic by means of NADW formation. Most of the C_{ant} injected in these regions are transported away, mostly into the tropics where the reservoir size is five times larger than the amount of C_{ant} injected locally. Here, we highlight the Nordic Seas, where very little of the injected C_{ant} remains in the region. At the same time, the Subpolar North Atlantic has been one of the most inefficient regions in terms of C_{ant} injected per unit volume, a pattern shown to be common for high latitudes and related to the low buffer capacity of these waters, the rapid ventilation of surface waters by vigorous mixing, and the longer residence time of these waters in the interior ocean. On the contrary, subtropical regions have been the most efficient injecting C_{ant} per unit of volume.

At least one fifth of the total C_{ant} injected since preindustrial times has now reached depths greater than 1,000 m, which constitutes the deep, long-term reservoir where most of the C_{ant} are stored for centennial timescales. Although the deep injection pattern is similar to the total injection, the relative importance of each of the regions differs. A relatively small proportion of the C_{ant} injected in the subtropics ends up in the deep ocean, while this proportion is much higher in the Southern Ocean and the Nordic Seas, which are the most important regions in transporting C_{ant} into the deep ocean.

The source region and timescale at which the deep reservoir is filled vary regionally. The deep Pacific, Indian, and Subantarctic-Arctic reservoirs have been only recently filled with C_{ant} subducted in the Southern Ocean, and the age of the C_{ant} is therefore young. The C_{ant} in the deep Atlantic-Arctic and Antarctic is older due to the shorter transit times, which allowed those regions to be filled at earlier times.

Future work is needed to constrain the fluxes of C_{ant} from tracers. The TMI offers the advantage of being derived mostly from observations; however, the ventilation rates are dependent on the ^{14}C observations, which are sparse in many regions (e.g., the Arctic). New ^{14}C measurements in combination with other ocean tracers, such as CFCs and SF6 gases, would provide a better constraint on the ventilation rates in the TMI and similar methods.

Data Availability Statement

The Total Matrix Intercomparison transport matrix used in this study to produce the anthropogenic carbon fields as well as the Green's functions is published by Gebbie & Huybers (2012) and is available in GitHub (<https://github.com/gebbie/TMI.mat>). The anthropogenic carbon boundary condition is published by DeVries (2014) and GLODAP mapped climatology by Lauvset et al. (2016).

References

- Aldama-Campino, A., & DÖös, K. (2020). Mediterranean overflow water in the North Atlantic and its multidecadal variability. *Tellus, Series A: Dynamic Meteorology and Oceanography*, 72(1), 1–10. <https://doi.org/10.1080/16000870.2018.1565027>
- Álvarez, M., Ríos, A. F., Pérez, F. F., Bryden, H. L., & Rosón, G. (2003). Transports and budgets of total inorganic carbon in the subpolar and temperate North Atlantic. *Global Biogeochemical Cycles*, 17(1), 2–1. <https://doi.org/10.1029/2002gb001881>

Acknowledgments

We thank Tim DeVries and an anonymous reviewer for their constructive reviews. X. Davila was supported by a PhD research fellowship from the University of Bergen. G. Gebbie was supported by U.S. NSF Grant 88075300. A. Brakstad was supported by the Trond Mohn Foundation under grant agreement BFS2016REK01. E. L. McDonagh was supported by UKRI grants Atlantic Biogeochemical fluxes (ref no. NE/M005046/2) and TICOC:Transient tracer-based Investigation of Circulation and Thermal Ocean Change (ref no. NE/P019293/2). A. Olsen and S. K. Lauvset appreciate support from the Research Council of Norway (ICOS-Norway, project number 245972). J. Schwinger acknowledges support by the Research Council of Norway through project INES (project number 270061). Supercomputer time and storage resources were provided by the The Norwegian e-infrastructure for Research Education (UNINETT Sigma2, projects nn2980k and ns2980k).

- Anderson, L. A., & Sarmiento, J. L. (1994). Redfield ratios of remineralization determined by nutrient data analysis. *Global Biogeochemical Cycles*, 8(1), 65–80. <https://doi.org/10.1029/93GB03318>
- Aumont, O., & Bopp, L. (2006). Globalizing results from ocean in situ iron fertilization studies. *Global Biogeochemical Cycles*, 20(2). <https://doi.org/10.1029/2005GB002591>
- Bopp, L., Lévy, M., Resplandy, L., & Sallée, J. B. (2015). Pathways of anthropogenic carbon subduction in the global ocean. *Geophysical Research Letters*, 42(15), 6416–6423. <https://doi.org/10.1002/2015GL065073>
- Carter, B. R., Feely, R. A., Lauvset, S. K., Olsen, A., DeVries, T., & Sonnerup, R. (2021). Preformed properties for marine organic matter and carbonate mineral cycling quantification. *Global Biogeochemical Cycles*, 35(1), e2020GB006623. <https://doi.org/10.1029/2020GB006623>
- Chafik, L., & Rossby, T. (2019). Volume, heat, and freshwater Divergences in the subpolar North Atlantic suggest the Nordic Seas as key to the state of the meridional overturning circulation. *Geophysical Research Letters*, 46(9), 4799–4808. <https://doi.org/10.1029/2019GL082110>
- Danabasoglu, G., Yeager, S. G., Bailey, D., Behrens, E., Bentsen, M., Bi, D., et al. (2014). North Atlantic simulations in coordinated ocean-ice reference experiments phase II (CORE-II), Part I: Mean states. *Ocean Modelling*, 73, 76–107. <https://doi.org/10.1016/j.ocemod.2013.10.005>
- DeVries, T. (2014). The oceanic anthropogenic CO₂ sink: Storage, air-sea fluxes, and transports over the industrial era. *Global Biogeochemical Cycles*, 1–17. <https://doi.org/10.1002/2013GB004739>
- DeVries, T., Holzer, M., & Primeau, F. (2017). Recent increase in oceanic carbon uptake driven by weaker upper-ocean overturning. *Nature*, 542(7640), 215–218. <https://doi.org/10.1038/nature21068>
- DeVries, T., & Primeau, F. (2011). Dynamically and observationally constrained estimates of water-mass distributions and ages in the global ocean. *Journal of Physical Oceanography*, 41(12), 2381–2401. <https://doi.org/10.1175/JPO-D-10-05011.1>
- England, M. H., & Maier-Reimer, E. (2001). Using chemical tracers to assess ocean models. *Reviews of Geophysics*, 39(1), 29–70. <https://doi.org/10.1029/1998RG000043>
- Friedlingstein, P., O'Sullivan, M., Jones, M. W., Andrew, R. M., Hauck, J., Olsen, A., et al. (2020). Global carbon budget 2020. *Earth System Science Data*, 12(4), 3269–3340. <https://doi.org/10.5194/essd-12-3269-2020>
- Frölicher, T. L., Sarmiento, J. L., Paynter, D. J., Dunne, J. P., Krasting, J. P., & Winton, M. (2015). Dominance of the Southern Ocean in anthropogenic carbon and heat uptake in CMIP5 models. *Journal of Climate*, 28(2), 862–886. <https://doi.org/10.1175/JCLI-D-14-00117.1>
- Gebbie, G. (2012). Tracer transport timescales and the observed Atlantic-Pacific lag in the timing of the Last Termination. *Paleoceanography*, 27(3), 1–14. <https://doi.org/10.1029/2011PA002273>
- Gebbie, G., & Huybers, P. (2010). Total matrix Intercomparison: A method for determining the geometry of water-mass pathways. *Journal of Physical Oceanography*, 40(8), 1710–1728. <https://doi.org/10.1175/2010jpo4272.1>
- Gebbie, G., & Huybers, P. (2012). The mean age of ocean waters inferred from radiocarbon observations: Sensitivity to surface sources and accounting for mixing histories. *Journal of Physical Oceanography*, 42(2), 291–305. <https://doi.org/10.1175/jpo-d-11-043.1>
- Goris, N., Tjiputra, J. F., Olsen, A., Schwinger, J., Lauvset, S. K., & Jeansson, E. (2018). Constraining projection-based estimates of the future North Atlantic carbon uptake. *Journal of Climate*, 31(10), 3959–3978. <https://doi.org/10.1175/JCLI-D-17-0564.1>
- Graven, H. D., Gruber, N., Key, R., Khatiwala, S., & Giraud, X. (2012). Changing controls on oceanic radiocarbon: New insights on shallow-to-deep ocean exchange and anthropogenic CO₂ uptake. *Journal of Geophysical Research*, 117(10), 1–16. <https://doi.org/10.1029/2012JC008074>
- Gruber, N., Clement, D., Carter, B. R., Feely, R. A., Heuven, S. V., Hoppema, M., et al. (2019). The oceanic sink for anthropogenic CO₂ from 1994 to 2007. *Science*, 363(6432), 1193–1199. <https://doi.org/10.1126/science.aau5153>
- Gruber, N., Landschützer, P., & Lovenduski, N. S. (2018). The variable Southern Ocean carbon sink. *Annual Review of Marine Science*, 9(1), 159–186. <https://doi.org/10.1146/annurev-marine-121916-063407>
- Heuzé, C. (2017). North Atlantic deep water formation and AMOC in CMIP5 models. *Ocean Science Discussions*, 1–22. <https://doi.org/10.5194/os-2017-2>
- Heuzé, C. (2021). Antarctic bottom water and North Atlantic deep water in CMIP6 models. *Ocean Science*, 17(1), 59–90. <https://doi.org/10.5194/os-17-59-2021>
- Holfort, J., Johnson, K. M., Schneider, B., Siedler, G., & Wallace, D. W. (1998). Meridional transport of dissolved inorganic carbon in the South Atlantic Ocean. *Global Biogeochemical Cycles*, 12(3), 479–499. <https://doi.org/10.1029/98GB01533>
- Holzer, M., Devries, T., & de Lavergne, C. (2021). Diffusion controls the ventilation of a Pacific Shadow Zone above abyssal overturning. *Nature Communications*, 1–13, 4348. <https://doi.org/10.1038/s41467-021-24648-x>
- Iudicone, D., Rodgers, K. B., Plancherel, Y., Aumont, O., Ito, T., Key, R. M., et al. (2016). The formation of the ocean's anthropogenic carbon reservoir. *Scientific Reports*, 6(1), 1–16. <https://doi.org/10.1038/srep35473>
- Jeansson, E., Olsen, A., Eldevik, T., Skjelvan, I., Omar, A. M., Lauvset, S. K., et al. (2011). The Nordic Seas carbon budget: Sources, sinks, and uncertainties. *Global Biogeochemical Cycles*, 25(4), 1–16. <https://doi.org/10.1029/2010GB003961>
- Khatiwala, S. (2007). A computational framework for simulation of biogeochemical tracers in the ocean. *Global Biogeochemical Cycles*, 21(3), 1–14. <https://doi.org/10.1029/2007GB002923>
- Khatiwala, S., Primeau, F., & Hall, T. (2009). Reconstruction of the history of anthropogenic CO₂ concentrations in the ocean. *Nature*, 462(7271), 346–349. <https://doi.org/10.1038/nature08526>
- Khatiwala, S., Tanhua, T., Mikaloff Fletcher, S., Gerber, M., Doney, S. C., Graven, H. D., et al. (2013). Global ocean storage of anthropogenic carbon. *Biogeosciences*, 10(4), 2169–2191. <https://doi.org/10.5194/bg-10-2169-2013>
- Lauvset, S. K., Carter, B. R., Perez, F. F., Jiang, L. Q., Feely, R. A., Velo, A., & Olsen, A. (2020). Processes driving global interior ocean pH distribution. *Global Biogeochemical Cycles*, 34(1), 1–17. <https://doi.org/10.1029/2019GB006229>
- Lauvset, S. K., Key, R. M., Olsen, A., Van Heuven, S., Velo, A., Lin, X., et al. (2016). A new global interior ocean mapped climatology: The 1° × 1° GLODAP version 2. *Earth System Science Data*, 8(2), 325–340. <https://doi.org/10.5194/essd-8-325-2016>
- Liddicoat, S. K., Wiltshire, A. J., Jones, C. D., Arora, V. K., Brovkin, V., Cadule, P., et al. (2021). Compatible fossil fuel CO₂ emissions in the CMIP6 Earth System models' historical and shared socioeconomic pathway experiments of the twenty-first century. *Journal of Climate*, 34(8), 2853–2875. <https://doi.org/10.1175/JCLI-D-19-0991.1>
- Lozier, M. S., Li, F., Bacon, S., Bahr, F., Bower, A. S., Cunningham, S. A., et al. (2019). A sea change in our view of overturning in the subpolar North Atlantic. *Science*, 363(6426), 516–521. <https://doi.org/10.1126/science.aau6592>
- Lundberg, L., & Haugan, P. M. (1996). A Nordic Seas-Arctic Ocean carbon budget from volume flows and inorganic carbon data. *Global Biogeochemical Cycles*, 10(3), 493–510. <https://doi.org/10.1029/96GB00359>
- Maccdonald, A. M., Baringer, M. O., Wanninkhof, R., Lee, K., & Wallace, D. W. (2003). A 1998–1992 comparison of inorganic carbon and its transport across 24.5°N in the Atlantic. *Deep-Sea Research Part II Topical Studies in Oceanography*, 50(22–26), 3041–3064. <https://doi.org/10.1016/j.dsr2.2003.07.009>
- Madeç, G. (2008). *NEMO Ocean Engine* (Vol. 27). Institut Pierre-Simon Laplace (IPSL). <https://doi.org/10.5281/zenodo.3878122>

- Madec, G., Delecluse, P., Imbard, M., & Lévy, C. (1998). *OPA 8.1 ocean general circulation model reference manual* (Vol. 11, p. 91). Note du Pole de modélisation, Institut Pierre-Simon Laplace (IPSL).
- Maier-Reimer, E., & Hasselmann, K. (1987). Transport and storage of CO₂ in the ocean. *Climate Dynamics*, 2(2), 63–90. <https://doi.org/10.1007/BF01054491>
- McNeil, B. I., Matear, R. J., Key, R. M., Bullister, J. L., & Sarmiento, J. L. (2003). Anthropogenic CO₂ uptake by the ocean based on the global chlorofluorocarbon data set. *Science*, 299(5604), 235–239. <https://doi.org/10.1126/science.1077429>
- Menary, M. B., Jackson, L. C., & Lozier, M. S. (2020). Reconciling the relationship between the AMOC and Labrador Sea in OSNAP observations and climate models. *Geophysical Research Letters*, 47(18). <https://doi.org/10.1029/2020GL089793>
- Middelburg, J. J., Soetaert, K., & Hagens, M. (2020). Ocean alkalinity, buffering and biogeochemical processes. *Reviews of Geophysics*, 58(3). <https://doi.org/10.1029/2019RG000681>
- Mikaloff-Fletcher, S. E., Gruber, N., Jacobson, A. R., Doney, S. C., Dutkiewicz, S., Gerber, M., et al. (2006). Inverse estimates of anthropogenic CO₂ uptake, transport, and storage by the ocean. *Global Biogeochemical Cycles*, 20(2), 1–16. <https://doi.org/10.1029/2005GB002530>
- Olsen, A., Omar, A. M., Jeansson, E., Anderson, L. G., & Bellerby, R. G. (2010). Nordic seas transit time distributions and anthropogenic CO₂. *Journal of Geophysical Research*, 115(5), 1–14. <https://doi.org/10.1029/2009JC005488>
- Østerhus, S., Woodgate, R., Valdimarsson, H., Turrell, B., de Steur, L., Quadfasel, D., et al. (2019). Arctic Mediterranean exchanges: A consistent volume budget and trends in transports from two decades of observations. *Ocean Science Discussions*, 1–37. <https://doi.org/10.5194/os-2018-114>
- Passow, U., & Carlson, C. A. (2012). The biological pump in a high CO₂ world. *Marine Ecology Progress Series*, 470(2), 249–271. <https://doi.org/10.3354/meps09985>
- Primeau, F. W. (2005). Characterizing transport between the surface mixed layer and the ocean interior with a forward and adjoint global ocean transport model. *Journal of Physical Oceanography*, 35(4), 545–564. <https://doi.org/10.1175/JPO2699.1>
- Primeau, F. W., & Holzer, M. (2006). The Ocean's memory of the atmosphere: Residence-time and ventilation-rate distributions of water masses. *Journal of Physical Oceanography*, 36(7), 1439–1456. <https://doi.org/10.1175/JPO2919.1>
- Racapé, V., Zunino, P., Mercier, H., Lherminier, P., Bopp, L., Pérez, F. F., & Gehlen, M. (2018). Transport and storage of anthropogenic C in the North Atlantic Subpolar Ocean. *Biogeosciences*, 15(14), 4661–4682. <https://doi.org/10.5194/bg-15-4661-2018>
- Rosón, G., Rios, A. F., Perez, F. F., Lavin, A., & Bryden, H. L. (2003). Carbon distribution, fluxes, and budgets in the subtropical North Atlantic Ocean (24.5°N). *Journal of Geophysical Research*, 108(C5), 3144. <https://doi.org/10.1029/1999jc000047>
- Sabine, C. L., Feely, R. A., Gruber, N., Key, R. M., Lee, K., Bullister, J. L., et al. (2004). The oceanic sink for anthropogenic CO₂. *Science*, 305(July), 367–372. <https://doi.org/10.1126/science.1097403>
- Sallée, J. B., Matear, R. J., Rintoul, S. R., & Lenton, A. (2012). Localized subduction of anthropogenic carbon dioxide in the Southern Hemisphere oceans. *Nature Geoscience*, 5(8), 579–584. <https://doi.org/10.1038/ngeo1523>
- Sarmiento, J. L., & Gruber, N. (2002). Sinks for anthropogenic carbon. *Physics Today*, 55(8), 30–36. <https://doi.org/10.1063/1.1510279>
- Sarmiento, J. L., Orr, J. C., & Siegenthaler, U. (1992). A perturbation simulation of CO₂ uptake in an ocean general circulation model. *Journal of Geophysical Research*, 97(C3), 3621–3645. <https://doi.org/10.1029/91JC02849>
- Schlitzer, R. (2004). Export production in the equatorial and North Pacific derived from dissolved oxygen, nutrient and carbon data. *Journal of Oceanography*, 60(1), 53–62. <https://doi.org/10.1023/B:JOCE.0000038318.38916.e6>
- Siegel, D. A., Devries, T., Doney, S. C., & Bell, T. (2021). Assessing the sequestration time scales of some ocean-based carbon dioxide reduction strategies. *Environmental Research Letters*, 16(10), 104003. <https://doi.org/10.1088/1748-9326/ac0b0e>
- Timmerman, R., Goosse, H., Madec, G., Fichéfet, T., Ethe, C., & Duliere, V. (2005). On the representation of high latitude processes in the ORCA-LIM global coupled sea ice-ocean model. *Ocean Modelling*, 8(1–2), 175–201. <https://doi.org/10.1016/j.ocemod.2003.12.009>
- Wang, S., Moore, J. K., Primeau, F. W., & Khatiwala, S. (2012). Simulation of anthropogenic CO₂ uptake in the CCSM3.1 ocean circulation-biogeochemical model: Comparison with data-based estimates. *Biogeosciences*, 9(4), 1321–1336. <https://doi.org/10.5194/bg-9-1321-2012>
- Waugh, D. W., Hall, T. M., McNeil, B. I., Key, R., & Matear, R. J. (2006). Anthropogenic CO₂ in the oceans estimated using transit time distributions. *Tellus Series B Chemical and Physical Meteorology*, 58(5), 376–389. <https://doi.org/10.1111/j.1600-0889.2006.00222.x>

References From the Supporting Information

- Lueker, T. J., Dickson, A. G., & Keeling, C. D. (2000). Ocean pCO₂ calculated from dissolved inorganic carbon, alkalinity, and equations for K₁ and K₂: Validation based on laboratory measurements of CO₂ in gas and seawater at equilibrium. *Marine Chemistry*, 70(1–3), 105–119. [https://doi.org/10.1016/S0304-4203\(00\)00022-0](https://doi.org/10.1016/S0304-4203(00)00022-0)
- van Heuven, S., Pierrot, D., Rae, J., Lewis, E., & Wallace, D. (2011). *CO₂SYS, MATLAB program developed for CO₂ system calculations. ORNL/CDIAC-105b*. Carbon Dioxide Inf. Anal. Cent. Oak Ridge Natl. Lab.

Supporting Information for ”How is the ocean anthropogenic carbon reservoir filled?”

Xabier Davila¹, Geoffrey Gebbie², Ailin Brakstad¹, Siv K. Lauvset³, Elaine

L. McDonagh^{3,4}, Jrg Schwinger³, Are Olsen¹

¹Geophysical Institute, University of Bergen and Bjerknnes Centre for Climate Research, Bergen, Norway.

²Department of Physical Oceanography, Woods Hole Oceanographic Institution, Woods Hole, MA 02543, USA.

³NORCE Norwegian Research Centre, Bjerknnes Centre for Climate Research, Bergen, Norway.

⁴National Oceanography Centre, Southampton, UK.

1. C_{ant} at saturation

As surface-waters are constantly mixed, the less time they spend in contact with the atmosphere the less saturated with C_{ant} they are. C_{ant} concentration at saturation can be calculated assuming that the surface ocean pCO_2 has tracked the atmospheric CO_2 rise using the definition of the Revelle factor:

$$\gamma_{DIC} = \frac{DIC^0 \partial pCO_2}{pCO_2^0 \partial DIC} \quad (1)$$

where γ_{DIC} is the Revelle factor, DIC^0 is the preindustrial Dissolved Inorganic Carbon (DIC) concentration and pCO_2^0 is the surface ocean preindustrial partial pressure of CO_2 .

Corresponding author: X. Davila, Geophysical Institute, University of Bergen and Bjerknnes Centre for Climate Research, Bergen, Norway (Xabier.Davila@uib.no)

We want to resolve for the change in DIC (∂DIC) assuming that the ocean change in pCO_2 (∂pCO_2) is equal to the change in atmospheric concentrations.

Two known parameters of the carbon system are enough to compute the Revelle factor and the unknown change in DIC. In our case we use DIC^0 and modern alkalinity from the mapped GLODAP climatology (Lauvset et al., 2016), where alkalinity is assumed to have remained constant throughout the industrial era. Here we use the software CO2SYS for this calculation (van Heuven et al., 2011) with the K1 and K2 dissociation constants from Lueker, Dickson, and Keeling (2000). pCO_2 and DIC are calculated at a timestep of 1 year and substitute the preindustrial values at Equation 1. The differences between C_{ant} at saturation and "observed" concentrations show that highly stratified regions, like the tropics, are very close to being saturated with C_{ant} (Figure S1). Regions with deep mixed-layers, on the other hand, are far from saturation, especially the Southern Ocean. The difference between the observed and saturated C_{ant} reflects the effects of mixing and transport of surface waters and further exacerbates the effect of the buffer capacity and the residence time of waters in the interior ocean.

References

- Lauvset, S. K., Key, R. M., Olsen, A., Van Heuven, S., Velo, A., Lin, X., . . . Watelet, S. (2016). A new global interior ocean mapped climatology: The 1° 1° GLODAP version 2. *Earth System Science Data*, 8(2), 325–340. doi: 10.5194/essd-8-325-2016
- Lueker, T. J., Dickson, A. G., & Keeling, C. D. (2000, 5). Ocean pCO_2 calculated from dissolved inorganic carbon, alkalinity, and equations for K1 and K2: Validation based on laboratory measurements of CO_2 in gas and seawater at equilibrium. *Marine*

Chemistry, 70(1-3), 105–119. doi: 10.1016/S0304-4203(00)00022-0

van Heuven, S., Pierrot, D., Rae, J., Lewis, E., & Wallace, D. (2011). CO2SYS, MATLAB program developed for CO2 system calculations. *ORNL/CDIAC-105b. Carbon Dioxide Inf. Anal. Cent. Oak Ridge Natl. Lab., Oak Ridge, Tenn.*

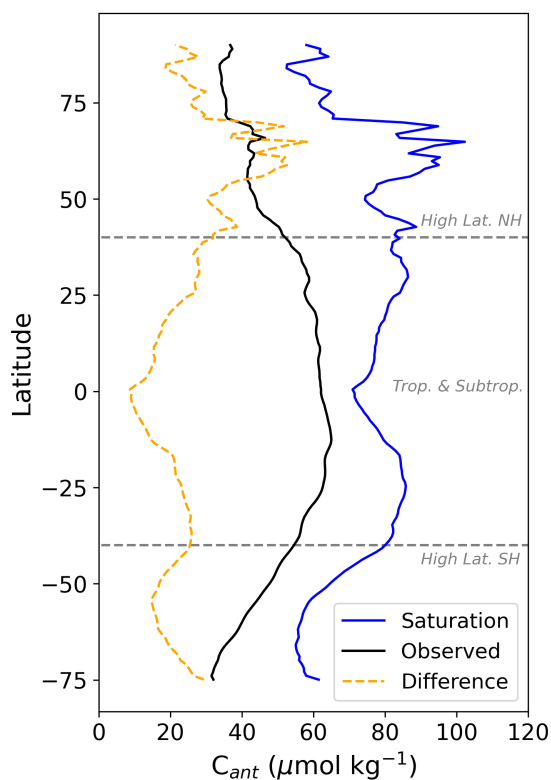


Figure S1. Latitudinal average of observed and saturation mixed-layer C_{ant} concentration. Observation-based C_{ant} was extracted from the mapped GLODAP climatology (Lauvset et al., 2016). Saturation concentrations were calculated from the preindustrial DIC in mapped GLODAP using CO2SYS (van Heuven et al., 2011) and assuming that the surface ocean $p\text{CO}_2$ has tracked the atmospheric CO_2 rise. The difference (saturation minus the "observed") is due to the mixing and transport of surface waters.

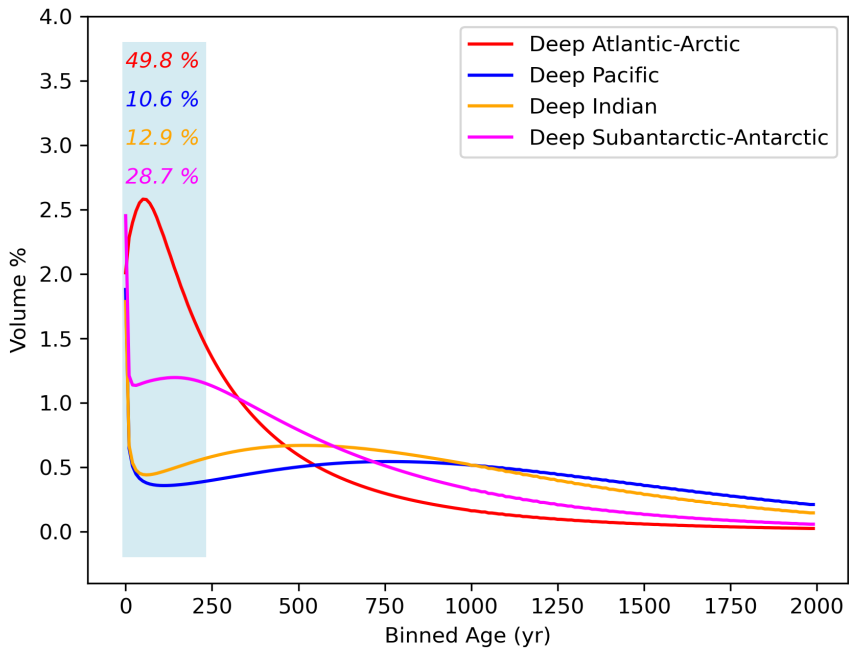


Figure S2. Transient time distribution (TTD) of all waters below 1000 m in the (A) deep Atlantic (including the Arctic), (B) Pacific, (C) Indian and (D) Antarctic were injected across the mixed layer. The age distribution was binned every 10 years. The light blue shadow indicate the industrial period (last 233 years) considered in Figure 7 and the number within correspond to the percentage of the deep reservoir ventilated for the same period.

Paper II

On the Origins of Open Ocean Oxygen Minimum Zones

Xabier Davila, Are Olse, Siv K. Lauvset, Elaine L. McDonagh, Ailin Brakstad, Geoffrey Gebbie

Journal of Geophysical Research: Oceans, (Submitted)

On the Origins of Open Ocean Oxygen Minimum Zones

Xabier Davila^{1,2}, Are Olsen^{1,2}, Siv K. Lauvset^{3,2}, Elaine L. McDonagh^{3,2,4},
Ailin Brakstad^{1,2}, Geoffrey Gebbie⁵

¹Geophysical Institute, University of Bergen, Norway.

²Bjerknes Centre for Climate Research, Bergen, Norway.

³NORCE Norwegian Research Centre, Bergen, Norway.

⁴National Oceanography Centre, Southampton, UK.

⁵Department of Physical Oceanography, Woods Hole Oceanographic Institution, Woods Hole, MA 02543,
USA.

Key Points:

- We determine the origins of Oxygen Minimum Zones (OMZs) in terms of sources of volume, oxygen, and oxygen-deficit.
- High-latitude source regions have a key role in feeding OMZs with oxygen-deficit, at centennial to millennial timescales.
- The oxygen-deficit in the OMZs originates mostly from remineralization outside the OMZs.

Corresponding author: Xabier Davila, Xabier.Davila@uib.no

Abstract

Recent work suggests that Oxygen Minimum Zones (OMZs) are sustained by the supply of oxygen-poor waters rather than the export of organic matter from the local surface layer and its subsequent remineralization inside OMZs. However, the mechanisms that form and maintain OMZs are not well constrained, such as the origin of the oxygen that oxygenates OMZs, and the locations where oxygen consumption occurs. Here we use an observation-based transport matrix to determine the origins of open ocean OMZs in terms of 1) OMZ volume, 2) oxygen that survives remineralization and oxygenates OMZs, and 3) oxygen utilization in the interior ocean that contributes to the oxygen-deficit of OMZs. We also determine where the utilization of oxygen occurs along the pathways that ventilate the OMZs. Our results show that about half of the volume of OMZ waters originate in high-latitude regions, but most of their oxygen is utilized for remineralization before they reach OMZs. Instead, OMZs are mostly oxygenated by tropical, subtropical and intermediate waters formed in nearby regions. More than half of the utilization of oxygen occurs in the tropics and subtropics, while less than a third occurs within the OMZs themselves. We therefore suggest that, in steady-state, OMZs are primarily set by ocean circulation pathways that high-latitude deep and old water upwards, with relatively low oxygen content.

Plain Language Summary

Oxygen Minimum Zones (OMZs) are regions in the ocean where the dissolved oxygen concentration is low enough that many animals cannot survive there. It is uncertain what processes dominate the formation of OMZs because oxygen measurements only tell us about their deficit in oxygen, not where the oxygen loss occurred. Recent studies suggest that the oxygen is consumed in waters away from the OMZs and then these oxygen-poor waters are transported inside. However, the exact locations where the oxygen consumption occurs are still uncertain. Here we use a model built on observations to show where the oxygen is coming from and where it is consumed. We find that most of the oxygen in the OMZs is coming from young waters originating in nearby regions, while old waters that are low in oxygen come from distant, high-latitude regions. The latter suggests that oxygen consumption originates outside the OMZs and is then transported inside, agreeing with previous studies. About half of this consumption occurs as waters resurface in the tropics and subtropics where they are exposed to organic matter. We also find that the location of the OMZs is determined mainly from where water masses that sink in the high latitudes eventually resurface.

1 Introduction

Oxygen Minimum Zones (OMZs) are dissolved oxygen (O_2) deficient layers in the ocean of great importance for marine ecosystems and biogeochemical cycles. At oxygen concentrations below $20 \mu\text{mol kg}^{-1}$, denitrification takes place (Smethie, 1987), leading to the production of nitrous oxide, which is a powerful greenhouse gas that amplifies global warming (Keeling et al., 2010). Regions below $60 \mu\text{mol kg}^{-1}$ are effectively “dead zones” for many higher trophic level animals such as fish and crustaceans (Gray et al., 2002). OMZs are usually found at depths between 100 m and 900 m with O_2 concentrations as low as $4.5 \mu\text{mol kg}^{-1}$ (Karstensen et al., 2008). Direct observations show that OMZs are expanding (Stramma et al., 2010; Zhou et al., 2022), yet the underlying mechanisms are unclear. While global warming is expected to decrease ocean ventilation in a more stratified ocean (Keeling & Garcia, 2002), the myriad feedbacks involved result in highly uncertain responses of OMZs (Fu, Primeau, et al., 2018; Frölicher et al., 2020). Changes in circulation and biology dictate the shift from contraction to expansion of OMZ in CMIP6 models. A more sluggish circulation results in the expansion of low oxygenated waters in the periphery, while a combination of circulation and biological changes explain the

67 contraction of the core (Busecke et al., 2022). However, two key aspects that link changes
 68 in circulation and biology to changes at OMZs are generally unexplored, which are i) the
 69 origin of the oxygen that survives remineralization and oxygenates OMZs, as well as ii)
 70 the interior locations where the oxygen is utilized. Determining the mixed layer and ocean
 71 interior sources of OMZs is the purpose of this contribution.

72 The location and intensity of OMZs, as well as their sensitivity to climate variabil-
 73 ity and change, are determined by the fine balance between mechanisms that regulate
 74 oxygen supply and demand (Fu, Primeau, et al., 2018). There are three mechanisms that
 75 can contribute to the oxygen-deficit of OMZs: (1) Typically, OMZs are located under-
 76 neath high productivity upwelling areas (Helly & Levin, 2004), thus, export of a copi-
 77 ous amount of organic material and its remineralization can generate the oxygen-deficit;
 78 (2) the location of OMZs often coincides with the so-called "shadow zones" of thermo-
 79 cline ventilation pathways (Luyten et al., 1983) such that a combination of average oxy-
 80 gen consumption and sluggish circulation can lead to low oxygen; and (3) ample oxy-
 81 gen consumption can occur along the pathways as water circulates from the surface ocean
 82 to OMZs, such that the water masses that enter OMZs may be already depleted in oxy-
 83 gen on arrival. Hydrographic studies now indicate that the third mechanism, the trans-
 84 port of low-oxygen waters into OMZs, is the dominant contribution to OMZs. Olson et
 85 al. (1993) suggested that the Arabian Sea OMZ is maintained by moderate consump-
 86 tion in waters with initially low oxygen concentrations. Similarly, Kalvelage et al. (2013)
 87 showed that coastal currents (e.g., Peru-Chilean Undercurrent, Czeschel et al., 2011) trans-
 88 port a low-oxygen signal generated by remineralization within the sediments, into the
 89 East Tropical South Pacific (ETSP) OMZ. Finally, Sonnerup et al. (2019) estimated car-
 90 bon export rates and ventilation timescales in the ETSP OMZ based on transient tracers
 91 and suggested that this OMZ may be sustained by the input of low-oxygen water from
 92 the Peru-Chile coastal upwelling rather than local utilization.

93 More sophisticated methods, such as transport matrices that are generated by the
 94 inversion of either model output or observations, can be used to infer global ventilation
 95 pathways of OMZs. Fu, Bardin, and Primeau (2018) used a transport matrix based on
 96 the ocean circulation field of an Earth System Model (ESM) to quantify how surface ocean
 97 regions ventilate the Pacific OMZs, as well as the associated timescales. Their findings
 98 highlight the importance of intermediate waters, in accordance with previous studies that
 99 show the importance of these waters in ventilating the subtropics (Shimizu et al., 2004;
 100 Sloyan et al., 2010; Jones et al., 2016). However, they did not diagnose the origin of their
 101 oxygen content. Recently, Holzer (2022) used the Ocean Circulation Inverse Model 2 (OCIM2;
 102 DeVries & Holzer, 2019) transport matrix to investigate the injection and fate of oxy-
 103 gen in the ocean, with specific attention given to the formation and sensitivities of the
 104 North Pacific Hypoxic Zone and the East Tropical North Pacific (ETNP) OMZ. They
 105 found that most of the oxygen-deficit in the North Pacific Hypoxic Zone and ETNP origi-
 106 nates in the upper ocean, at mid-latitudes and in the eastern Tropical Pacific. However,
 107 their analysis did not cover specifically the sources of all major OMZs. Here we use an
 108 observation-based transport matrix to take a closer look at the four major OMZs in the
 109 world ocean.

110 We use the Total Matrix Intercomparison (TMI) from Gebbie and Huybers (2012)
 111 to determine the sources of the four major OMZs: the East Tropical South Pacific (ETSP),
 112 East Tropical North Pacific (ETNP), North Pacific (NP) and the Arabian Sea - Bay of
 113 Bengal (AS-BB) OMZ. We explore the mixed layer origin of volume, oxygen and oxygen-
 114 deficit for the different endmembers that ventilate OMZs as well as the mean transit or
 115 ventilation timescales. We also determine the interior locations where the OMZ oxygen-
 116 deficit originates. These locations constitute the remineralization pathways between the
 117 mixed layer and OMZs, as well as within OMZs. Our results provide an observation-based
 118 benchmark for the origin and sensitivity of OMZs that results from each of the pathways
 119 and their contribution to oxygen and oxygen-deficit.

2 Methods

2.1 The TMI framework

In this section, we provide a brief review of the TMI framework as used in this study. The TMI is a water mass decomposition method developed by (Gebbie & Huybers, 2010, 2012) that diagnoses the circulation pathways that connect the inner ocean with the mixed layer. The TMI exploits the fact that the value of a water mass property in the interior ocean can be expressed as a linear combination of the properties in the neighbouring grid cells:

$$c_i = \sum_{j=i}^N m_{ij} c_j + r q_i, \quad (1)$$

where $N = 6$ is the number of neighbouring grid cells, m_{ij} is the fraction of water that originates from cell j with property c_j , and $\sum_{j=1}^N m_{ij} = 1$ for conservation of mass. The local source and sink for non-conservative properties are expressed by q_i , a single interior remineralization source that relates oxygen and nutrients through a global fixed stoichiometric ratio of P:N:O = 1:15.5:170 (Anderson & Sarmiento, 1994). Gebbie and Huybers (2010) expressed (1) in matrix form:

$$\mathbf{A} \mathbf{c} = \mathbf{d}, \quad (2)$$

where \mathbf{c} is a vector of the three-dimensional tracer field and \mathbf{A} is a matrix containing, *a priori* unknown, dimensionless mixing coefficients between grid cells, which result from the diffusive-advective water mass pathways. The right-hand side of (2), \mathbf{d} , is a vector containing the mixed layer boundary conditions \mathbf{c}_b and interior sources and sinks \mathbf{q} so that $\mathbf{d} = \mathbf{c}_b + \mathbf{q}$.

The only known element in (2) is the tracer distribution \mathbf{c} . (Gebbie & Huybers, 2010) used the climatological water property fields from Gouretski and Koltermann (2004) (potential temperature (θ), salinity, $\delta^{18}\text{O}_{sw}$, PO_4^{3-} , NO_3^- and O_2) to invert for \mathbf{A} , \mathbf{q} and \mathbf{c}_b . Later on, the circulation rates were also constrained through radiocarbon ($\Delta^{14}\text{C}$) observations from Key et al. (2004). The resulting transport matrix encapsulates the modern-day ocean circulation rates, in steady-state, where no changes in circulation, solubility or biology are accounted for. There are altogether 74064 grid cells distributed in 33 vertical levels with a horizontal resolution of 4° by 4° . In the mixed layer that represents \mathbf{c}_b , there are 16550 grid cells distributed in $s = 2806$ mixed layer boxes that represent a vertically homogeneous winter-time mixed layer for each horizontal grid cell. The depth of the mixed layer varies regionally, such that the number of vertical levels of grid cells in the mixed layer varies from 1 to 14.

Here, we use their ocean pathways \mathbf{A} , \mathbf{q} , and \mathbf{c}_b , as well as the transit time distribution within the pathways constrained by Gebbie and Huybers (2012). With these elements, the steady-state distribution of a tracer, - e.g., oxygen (Section 2.3), can be obtained by inverting (2) so that $\mathbf{c} = \mathbf{A}^{-1} \mathbf{d}$.

Similar to the ocean tracer distribution, the volume of the interior ocean originating from a given mixed layer box, \mathbf{v}_{tot} , can be estimated with (2) by propagating a dye from s in succession. However, a computationally more efficient way is by volume integrating the rows of \mathbf{A}^{-T} , which is done by multiplying the inverse transpose of \mathbf{A} by a vector containing the interior volume \mathbf{v} (Gebbie & Huybers, 2011):

$$\mathbf{v}_{\text{tot}} = \mathbf{A}^{-T} \mathbf{v}_i \quad \text{where } i \in \Omega. \quad (3)$$

When Ω is the entire interior ocean, the values of the vector \mathbf{v}_{tot} that are located at surface correspond to the total volume originating from each mixed layer box in the entire interior ocean. This expression is derived as a sensitivity or "adjoint" problem (see auxiliary material in Gebbie & Huybers, 2011). In our case, Ω is each of the OMZs considered (see Section 2.3), so that we are only tracing the volume of the OMZs back to surface and masking the rest of the ocean. The values in \mathbf{v}_{tot} corresponding to the interior ocean, match the amount of volume at Ω that crosses each interior grid cell i (Gebbie & Huybers, 2011; Brakstad et al., 2023).

The mean age or ventilation timescales $\bar{T}_{s,i}$ can be estimated by integrating the transit time distributions -i.e. the distribution of times t that it takes for mixed layer waters from s to arrive at an interior grid cell i , $G_{s,i}(t)$, constrained by Gebbie and Huybers (2012):

$$\bar{T}_{s,i} = \int_0^{\infty} t G_{s,i}(t) dt \quad \text{where } i \in \Omega, \quad (4)$$

where G is the transit time distribution, similar to the boundary propagator or Green's function of Haine and Hall (2002) but normalized to time-integrate to unity $\int_0^{\infty} G(t) dt = 1$ (Gebbie & Huybers, 2012).

2.2 Calculations of OMZ sources

To characterise the oceanic processes that lead to the formation of OMZs, we use the above equations and different combinations of prescribed boundary conditions and interior sources/sinks. Specifically, we calculate the origins of i) OMZ volume, ii) oxygen that survives remineralization and oxygenates OMZs and iii) its counterpart, the amount of oxygen utilized, as well as iv) the mean transit timescales or ventilation timescales. These results are presented in Section 3.1. We also determine the patterns of oxygen utilization that happen as the water travels from their mixed layer source regions to the various OMZs. We refer to these patterns as "remineralization pathways" and they are presented in Section 3.2.

We first present the dissolved oxygen distributions reconstructed by the TMI, for model evaluation purposes and to define the OMZs (Section 2.3). The oxygen distribution is given by inverting (2) so that $O_2 = \mathbf{A}^{-1}\mathbf{d}$. In this context, the two elements that compose \mathbf{d} are i) the optimized boundary condition of oxygen \mathbf{c}_b , and ii) the deficit of oxygen generated in each interior grid cell, \mathbf{q} (expressed in terms of $\mu\text{mol kg}^{-1}$), and represents the product of Oxygen Utilization Rates and the local residence times of waters in each grid cell (Gebbie & Huybers, 2012). Latitudinally averaged sections of \mathbf{q} are presented in Figure S1 in the Supporting Information.

The OMZs volume originating from each mixed layer box is given by the surface values of \mathbf{v}_{tot} by (3). Here, only the interior grid cells i within the OMZs ($i \in \Omega$) are traced back to their mixed layer origin.

The injection of oxygen across the base of the mixed layer that survives remineralization and reaches the OMZs, O_{2s} , is calculated with (2), by integrating the contribution from each of the mixed layer box s to the interior ocean, individually. This is done by prescribing a boundary condition of oxygen at s and keeping remineralization \mathbf{q} active in the entire interior ocean. We then invert for \mathbf{c} , from the resulting tracer field, O_{2s} is calculated by integrating the mass of oxygen over all i located within Ω :

$$O_{2s} = \sum_{i=0}^N O_{2s,i} \quad \text{where } i \in \Omega. \quad (5)$$

202 The counterpart of the preformed oxygen that has survived remineralization and
 203 reaches Ω is the True Oxygen Utilization (TOU, Ito et al., 2004) of s -sourced oxygen,
 204 i.e., the usual TOU partitioned by mixed layer origin. The injection of TOU of s -sourced
 205 is calculated in a similar way to (5). We first calculate the amount of preformed oxygen
 206 injected from each mixed layer box into Ω , O_{2s}^0 , by prescribing again a boundary con-
 207 dition of oxygen at s , but this time setting $q_i = 0$ everywhere, and integrating the re-
 208 sulting oxygen field over $i \in \Omega$. Then we calculate the TOU of s -sourced oxygen, $\Delta O_{2s} =$
 209 $O_{2s}^0 - O_{2s}$.

210 The mean transit times are directly calculated from the transit time distribution,
 211 $G_{s,i}$, determined by Gebbie and Huybers (2012) with the difference that only the wa-
 212 ters within the OMZ are traced ($i \in \Omega$). We also determine the mean age of the OMZs
 213 with (4).

214 The remineralization pathways presented in Section 3.2 represent the along-path
 215 oxygen utilization ($\overrightarrow{\Delta O_{2s}}$; $\mu\text{mol kg}^{-1}$), and represents the total amount of oxygen uti-
 216 lized in each interior location i that was transported across the mixed layer in s and will
 217 contribute to the oxygen-deficit in Ω . $\overrightarrow{\Delta O_{2s}}$ is calculated by combining the oxygen sinks
 218 \mathbf{q} and the density field ρ , with the global water pathways \mathbf{v}_{tot} in (3). This allows us to
 219 determine the oxygen utilized at each interior location on the paths that connect the mixed
 220 layer grid cell s with the OMZs. We call this the along-path oxygen utilization:

$$\overrightarrow{\Delta O_{2s}} = \mathbf{q} \cdot \mathbf{f}_s \cdot \rho \cdot \frac{\mathbf{v}_{\text{tot}}}{\mathbf{v}}, \quad (6)$$

221 where $\overrightarrow{\Delta O_{2s}}$ is a vector of a three-dimensional field and is the interior distribution of ΔO_{2s} ,
 222 so that $\Delta O_{2s} = \sum_{i=0}^N \overrightarrow{\Delta O_{2s,i}}$, where i in this case is anywhere in the world ocean. The
 223 elements on the right-hand side are also vectors and are multiplied element-wise. The
 224 interior distribution of water mass fraction originating from s is represented by \mathbf{f}_s , and
 225 $\frac{\mathbf{v}_{\text{tot}}}{\mathbf{v}}$ normalizes the volume of the OMZs that cross each interior grid cell in \mathbf{v}_{tot} with
 226 respect to the volume of each grid cell itself in \mathbf{v} , so that $\frac{\mathbf{v}_{\text{tot}}}{\mathbf{v}}$ indicates the fraction of
 227 \mathbf{v} that ends up in the OMZ. In other words, (6) quantifies the amount of water in each
 228 interior ocean grid cell that originates at s and is bound to arrive at an OMZ, combined
 229 with \mathbf{q} .

230 If s is the entire ocean mixed layer boxes, the totality of OMZ remineralization path-
 231 ways are mapped (Section 3.2). If s is the mixed layer boxes at a defined endmember
 232 (e.g., North Atlantic), the remineralization pathways for that individual endmember can
 233 be quantified (Supporting Information). The water mass fraction is calculated with (2)
 234 and prescribing a boundary condition of ones at the selected mixed layer boxes and zero
 235 elsewhere at surface, with no interior sources/sinks $q_i = 0$.

236 2.3 Model Evaluation

237 The TMI reproduces the oxygen distribution appropriately with respect to the er-
 238 ror of the observed climatology used to constrain it (Gouretski & Koltermann, 2004; Geb-
 239 bie & Huybers, 2010). The modelled and observed climatological distributions are com-
 240 parable, but the modelled concentrations are generally lower than observed (Figure 1).
 241 The TMI oxygen field is mostly biased towards the lower bound of the observational er-
 242 ror. The mismatch is well within observational error in the upper ocean but worsens with
 243 depth, up to ~ 10 times the observational error in the Southern Ocean (Figure S2).

244 The concentration gradients around OMZs are relatively small and the locations
 245 of OMZs are, as a consequence, very sensitive to the threshold used to define them. Ad-
 246 ditionally, biases of a few $\mu\text{mol kg}^{-1}$ in the climatology can significantly affect the ob-
 247 served OMZ extension. Several factors contribute to potential error in the climatology,
 248 notably: i) seasonal and interannual variability related to both circulation and biologi-

ical export can affect the position and intensity of OMZs, and is typically highest in the first 1000 m (Gouretski & Koltermann, 2004; Deutsch et al., 2011); ii) low oxygen levels such as in OMZs are close to the detection limit of available analytical methods (Bianchi et al., 2012); iii) the choice of spatial correlation when gap-filling discrete data points oversmooths data at small scales (Gouretski & Koltermann, 2004); and iv) evidence that gridded climatologies overestimate the oxygen concentrations and underestimate OMZs volume (Fuenzalida et al., 2009; Bianchi et al., 2012). On the other hand, the TMI is constrained using a climatological distribution and, as such, does not capture the co-variations between water mass formation and primary production. In addition, the oxygen distribution in the TMI is modelled assuming a fixed stoichiometric ratio of P:N:O = 1:15.5:170, which we acknowledge is not representative for the entire ocean (Teng et al., 2014; Carter et al., 2021), in particular in the OMZs as the strong reduction-oxidation gradients lead to denitrification and to differences in the P:N:O ratios (DeVries et al., 2012). However, we note that the mismatches between the modelled and observed distributions are not particularly high for the OMZs when normalized by the observational error of the data used to constrain the TMI (Figure S2).

We use an oxygen concentration of $20 \mu\text{mol kg}^{-1}$ as a threshold for OMZs. We do note that there is no agreed threshold that defines an OMZ, however (Karstensen et al., 2008; Paulmier & Ruiz-Pino, 2009; Busecke et al., 2022), and different studies use different thresholds depending on their goal. We decided to use $20 \mu\text{mol kg}^{-1}$ so our results are comparable to those of Fu, Bardin, and Primeau (2018) in terms of ventilation. This threshold also provides a good compromise between OMZ volume and the maximum concentration at which denitrification has been observed (Smethie, 1987), even if the definition of suboxic conditions is much lower ($2\text{--}10 \mu\text{mol kg}^{-1}$, Bianchi et al., 2012).

We focus on the four major OMZs: The East Tropical South Pacific (ETSP), East Tropical North Pacific (ETNP), North Pacific (NP) and the Arabian Sea - Bay of Bengal (AS-BB). Because the TMI is biased towards slightly low oxygen concentrations, the modelled OMZs are larger both horizontally and vertically than the observed ones (Figures 1 and 2). Also, the modelled ETSP and ETNP OMZs are not as separated as in the observations, but two distinct cores are nevertheless visible. We set the border between the ETNP and NP to 38°N . This coincides with the steep deepening of the $20 \mu\text{mol kg}^{-1}$ isoline that separates these two OMZs (not shown). The position of the modelled AS-BB OMZ agrees well with the observations, but it extends slightly too far south. The TMI also models an East Tropical Atlantic OMZ, however, this is not visible in observations as concentrations are higher than $20 \mu\text{mol kg}^{-1}$ (Keeling et al., 2010). The East Tropical Atlantic OMZ is therefore left out from our analyses. For the NP OMZ, the observed size is significantly smaller than the modelled. Overall we conclude that the TMI, as constrained by available observations and their uncertainties, provides a qualitatively realistic representation of oxygen in the ocean despite some systematic quantitative differences.

3 Results

3.1 Mixed Layer Sources

The role of the various water mass formation regions for the oxygenation of OMZs is determined by the interplay of their volume contributions and oxygen concentrations. While every OMZ is slightly different, they share some general features. Most of the volume originates from high latitudes, from the formation of mode, intermediate and bottom waters (Figure 3). For the Pacific OMZs, waters from the Southern Ocean make up the bulk of the volume, formed either in the Subantarctic region as Mode/Intermediate Water (defined as the combination of Antarctic Intermediate Water and Subantarctic Mode Water) or in the Antarctic region as Antarctic Bottom Water. The relative importance of Subantarctic Mode/Intermediate Waters for the Pacific OMZs decreases from

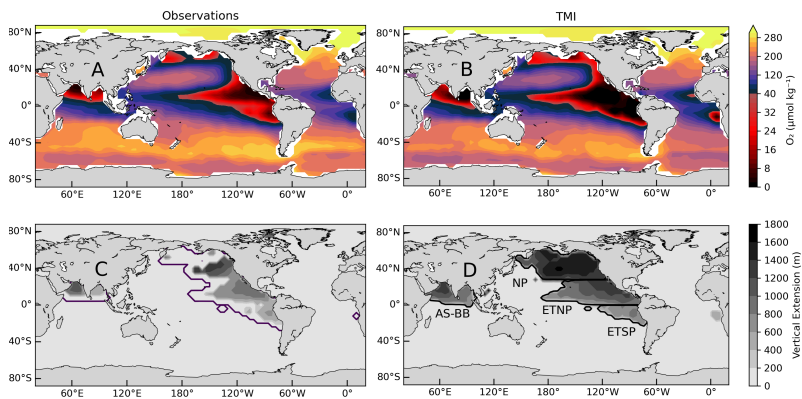


Figure 1. Oxygen concentration at 1000 m depth from (A) observations and (B) the TMI. The observed distribution is taken from the WOCE dataset (Gouretski & Koltermann, 2004), which was used to constrain the TMI. The modelled TMI distribution is calculated with (2) and assuming a fixed stoichiometric ratio of P:O = 1:-170. The colorbar breaks at 40 $\mu\text{mol kg}^{-1}$ to highlight the small gradients in the vicinity of the OMZs. Horizontal and vertical extension of (C) observed and (D) modelled OMZs, defined as waters with oxygen levels $< 20 \mu\text{mol kg}^{-1}$. The black contours in C indicate the maximum horizontal extension of OMZs when the observational error is taken into account. The four OMZs evaluated here are the Arabian Sea-Bay of Bengal (AS-BB), North Pacific (NP), East Tropical North Pacific (ETNP) and East Tropical South Pacific (ETSP).

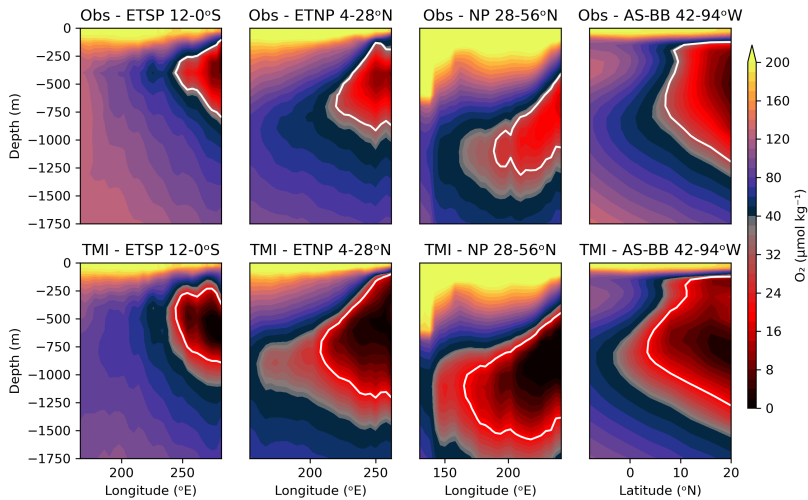


Figure 2. Meridionally averaged cross-sections of observed (top) and TMI (bottom) oxygen distributions in the water column for the East Tropical South Pacific, East Tropical North Pacific and North Pacific OMZs, and zonally averaged cross-section for the Arabian Sea - Bay of Bengal OMZ. The observed distribution is taken from the WOCE dataset (Gouretski & Koltermann, 2004) used to constrain the TMI. The colorbar breaks at $40 \mu\text{mol kg}^{-1}$ to highlight the small concentration gradients in the vicinity of OMZs. The white contour that overlies the observations indicates the maximum extent of the observed OMZ when observational error is taken into account, and the location of the modelled OMZ for the modelled distributions.

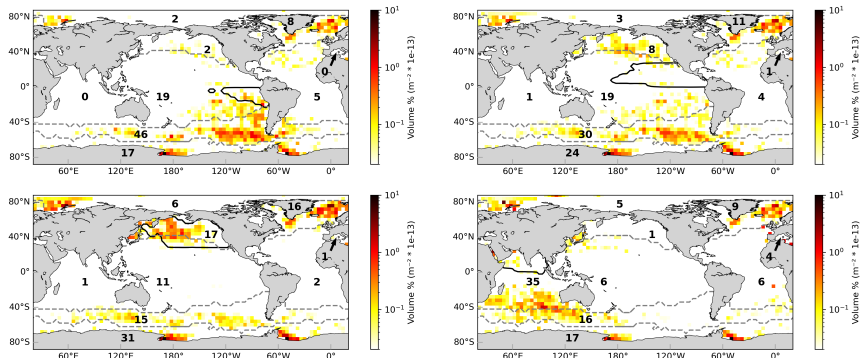


Figure 3. Fractional volume contributions of each mixed layer box to the OMZs, based on the transit time distributions (Section 2.1; Gebbie & Huybers, 2012). Values below $0.02 \text{ m}^{-2} \times 10^{-13} \%$ are masked. Black contours show the location of the OMZs as defined in Figure 1. Grey dashed lines show the outcrop region for each of the source water masses defined as in Gebbie and Huybers (2012) and the black numbers represent the volume % when integrated over each outcrop region. The colorscale is logarithmic.

300 south (46% in ETSP) to north (15% in NP). Conversely, the relative contribution of Antarctic
 301 Bottom Water increases from 17% in the ETSP to 31% in the NP. This is in accordance
 302 with previous estimates of these water masses (Johnson, 2008; DeVries & Primeau,
 303 2011). The fraction of water from the North Atlantic (North Atlantic Deep Water) also
 304 increases from south to north in the Pacific (from 8% in the ETSP to 16% in the NP).
 305 On the other hand, the North Pacific region contributes more to the northern Pacific OMZs
 306 (17% in NP) and less to the southern OMZ (2% in ETSP). The combined contribution
 307 by the tropics and subtropics to the volume of OMZs is substantial, but always less than
 308 the combined contributions of high-latitude sourced waters. The AS-BB is the most unique
 309 of all OMZs in terms of source waters, as more than a third (35%) of the volume origi-
 310 nates in the tropical and subtropical parts of the Indian Ocean. There are, neverthe-
 311 less, substantial contributions from Antarctic Bottom Water (17%) and Subantarctic Mode/Intermediate
 312 Waters (16%) to the AS-BB. Overall, the waters present in OMZs stem mostly from the
 313 high latitudes, specifically through the formation of bottom and mode waters in the South-
 314 ern Ocean. These waters contribute to about half of the volume of every OMZ except
 315 for the AS-BB where they contribute about one-third. The volumetric contributions from
 316 the mixed layer to the ETSP and ETNP, as well as its transit times, were also estimated
 317 by Fu, Bardin, and Primeau (2018) and the comparability of these estimates are discussed
 318 in Section 4.

319 The pattern of the oxygen injected across the base of the mixed layer that survives
 320 remineralization and reaches the OMZs (Figure 4) and its counterpart, the amount of
 321 injected oxygen that is utilized (Figure 5), follow the volume injection pattern largely.
 322 Endmembers adjacent to OMZs (i.e., Tropical and Subtropical regions) carry more oxy-
 323 gen than those further away from OMZs (i.e., the high latitudes) as waters from the lat-
 324 ter have been subjected to more utilization and thus contribute more to OMZs' oxy-
 325 gen-deficit. For the Pacific OMZs, Subantarctic Mode/Intermediate Waters and North Pa-
 326 cific Intermediate Waters are the main sources of oxygen that survives remineralization
 327 and is delivered to the OMZs. Similarly to water volume, the contribution to oxygena-
 328 tion by the Subantarctic Mode/Intermediate Waters endmember decreases from south

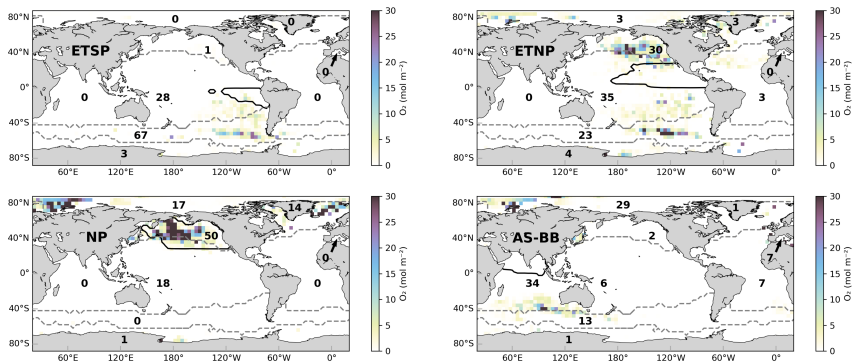


Figure 4. Injection of oxygen from each mixed layer box into the OMZs. This oxygen survives remineralization and arrives in the OMZs. Black contours represent the location of the OMZs as defined in Figure 1. Grey dashed lines represent the outcrop regions for each of the source water masses defined as in Figure 3. The numbers are the contributions of each outcrop region to the total oxygen content in the OMZ, in %. The colorscale of the ETSP panel has a different range than the rest.

329 to north, from 67% for ETSP to virtually zero for the NP. The contributions from the
 330 Antarctic region through the Antarctic Bottom Water, however, deviate from the vol-
 331 ume pattern. The Antarctic Bottom Water barely contributes to oxygen supply for any
 332 OMZ, despite its large volume contribution, reflecting that a large part of the preformed
 333 oxygen has been utilized as this water mass travels from its formation regions to OMZs.
 334 This is apparent in the oxygen-deficit contributions (ΔO_2 ; Figure 5). The North Atlantic
 335 is another region that barely contributes to oxygen as most of it has been utilized along-
 336 path; it contributes to the oxygen-deficit instead. In general, high-latitude waters are
 337 the most important contributors to oxygen-deficit and are in accordance with that of vol-
 338 ume; the oxygen-deficit from the AABW increase from the southernmost OMZ in the
 339 Pacific (20% for ETSP) to the northernmost (35% for NP), and so does that of the North
 340 Atlantic endmember (from 10% for ETSP to 18% to NP). Intermediate waters from the
 341 Subantarctic and North Pacific contribute to both oxygen-deficit and oxygenation. The
 342 oxygen-deficit contributions of Subantarctic Mode/Intermediate Waters to OMZs fol-
 343 low the same pattern as volume and oxygen, and decrease from the ETSP (45%) to NP
 344 (16%). Subtropical and Tropical waters, on the other hand, are more important for oxy-
 345 genation than for volume, reflecting the short pathways of these waters to OMZs. While
 346 these waters are the largest contributor to oxygen for the AS-BB (34%), they are also
 347 the largest contributor to the oxygen-deficit (30%, Figure 5). Surprisingly, the contri-
 348 bution of Arctic waters to the oxygenation of the AS-BB as well as the NP is also large,
 349 30 and 18%, respectively. While surprising, this partly agrees with the findings presented
 350 in Holzer (2022) (discussed in Section 4) where part of the oxygen that is utilized within
 351 the North Pacific Hypoxic Zone (PHZ) originates from the Arctic and North Atlantic.
 352 In general, the large amount of preformed oxygen injected by high-latitude endmembers
 353 as opposed to low-latitude ones, and its subsequent conversion to oxygen or oxygen-deficit,
 354 underscores the sensitivity of OMZs to high-latitude processes and the need for their cor-
 355 rect representation, e.g., in Earth System Models.

356 The regions that contribute most to the oxygen-deficit in OMZs are also those for
 357 which the transit times to the OMZs are the longest (Figure 6). The waters from these

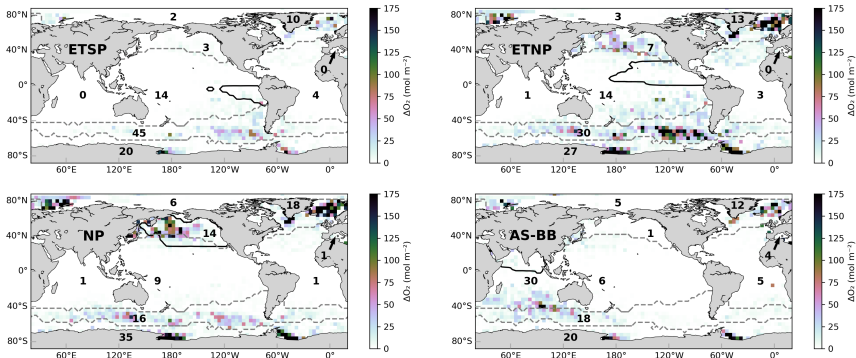


Figure 5. The injection of TOU of s -sourced oxygen across the base of the mixed layer, or the oxygen that is bound to be utilized from each mixed layer box en route to each of the OMZs. The integrated mass of oxygen utilized is equivalent to the total oxygen-deficit accumulated in each OMZ. Black and grey contours represent the same as in Figure 4. The numbers are the contributions of each outcrop region to the total oxygen-deficit in the OMZ, in %. The colorscale of the ETSP panel has a different range than the rest.

358 regions are subjected to remineralization for the longest time and thus have the high-
 359 est total utilization of oxygen. The transit times of the water masses from their source
 360 regions to the OMZs range from decadal to millennial. AABW and North Atlantic Deep
 361 Water have the longest mean transit time from their source regions to the OMZs, about
 362 3000 years. The shortest mean transit times are from regions adjacent to the OMZs. Sub-
 363 tropical and Tropical waters arrive in the ETSP and ETNP OMZs at decadal timescales,
 364 while Subantarctic Mode/Intermediate Waters and North Pacific Intermediate Water end-
 365 members take centuries. Transit times are overall longer to the NP and AS-BB OMZs.
 366 The shortest ventilation timescale for the NP OMZ is about 1000 years, by the North
 367 Pacific Intermediate Water, and 500 years for the AS-BB OMZ, by Subtropical and Tropi-
 368 cal waters. For both, the transit times of the other source waters (Subantarctic Mode/Intermediate
 369 Waters, Antarctic Bottom Water, North Atlantic Deep Water) are up to 3000 years. The
 370 mean age of the OMZ is determined as the volume-weighted average of all the transit
 371 times. This is lowest for the AS-BB OMZ, ~ 360 yr, followed by the ETSP OMZ with
 372 ~ 440 yr, the ETNP OMZ with ~ 610 yr and the NP OMZ is the oldest with a mean age
 373 of ~ 1150 yr.

3.2 Remineralization Pathways

374
 375 Traditional metrics such as True Oxygen Utilization (TOU) measure the path-integrated
 376 oxygen-deficit at a specific location, meaning that the signature of ocean circulation and
 377 oxygen utilization are convolved. The TMI directly constrains the generated oxygen-deficit
 378 in each interior location, q_i , from the tracer distribution (1). This allows us to determine
 379 whether the oxygen utilization occurs near the water formation regions, in the OMZ it-
 380 self, or on the path between the former and the latter. We call this the along-path oxy-
 381 gen utilization ($\overrightarrow{\Delta O_2}$ ($\mu\text{mol kg}^{-1}$); Section 2.2).

382 The vertically integrated distribution of $\overrightarrow{\Delta O_2}$ (Figure 7) is primarily dependent on
 383 the pathway that water masses follow from mixed layer to destination (Figure S3). In
 384 essence, \mathbf{v}_{tot} acts as a path selector (Holzer, 2022) for the global $\overrightarrow{\Delta O_2}$ pattern (Figure

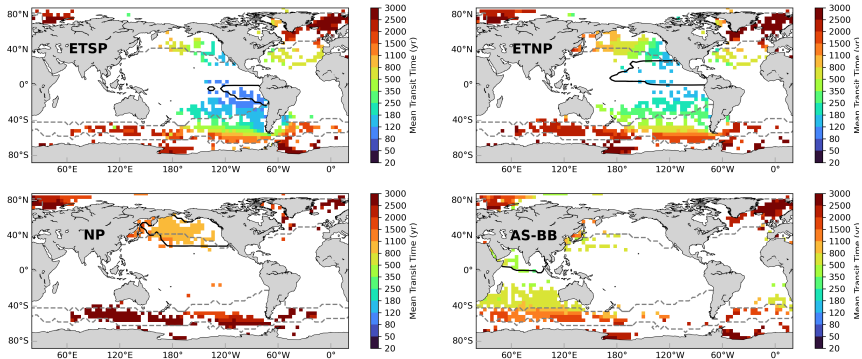


Figure 6. Mean transit time for the water from each mixed layer box to each of the OMZs. Black and grey contours represent the same as in Figure 4. The same mask as in Figure 3 is applied, so that mixed layer boxes that do not contribute significantly to the OMZ volume are white.

385 7), i.e., the larger the volume of water en route to an OMZ in a given grid cell the larger
 386 the contribution of remineralization in that grid cell to the oxygen-deficit of the OMZ.
 387 $\overline{\Delta O_2}$ also expresses the sensitivity of the OMZs to remineralization, i.e., how much would
 388 the oxygen-deficit in the OMZs change per unit of change in remineralization. As ex-
 389 pected, per area of ocean, the OMZs are most sensitive to the remineralization that oc-
 390 curs around the OMZs (highest $\overline{\Delta O_2}$; Figure 7), however, this is because the volume frac-
 391 tions of waters bound to reach the OMZs are largest in the vicinity of the OMZs, and
 392 not because of local export production resulting in unusually large oxygen sinks. The
 393 OMZs do not stand out as regions with high $\overline{\Delta O_2}$ nor are they distinguishable from the
 394 rest of the ocean when the global ocean is taken as destination Ω (Figure 7 - Global).
 395 The fact that OMZs are not regions of excessive oxygen utilization combined with the
 396 findings on the mixed layer sources (Section 3.1), suggests that the location of OMZs is
 397 governed by the geometry of the oceanic pathways, i.e., OMZs are located in regions where
 398 old and dense deep waters gain enough buoyancy to return to the upper ocean (Primeau
 399 & Holzer, 2006; De Lavergne et al., 2017; Holzer et al., 2021).

400 We further investigate the regional distribution of oxygen consumption, from each
 401 source region to each of the four OMZs investigated here (Figure 8). Most of the $\overline{\Delta O_2}$
 402 originates outside OMZs, with only less than a third occurring within. When the global
 403 ocean mixed layer is taken as a source, 17% of the oxygen-deficit within the ETSP is gen-
 404 erated within the ETSP OMZ. This fraction is 17% for the ETNP, 22% for the NP, and
 405 31% for the AS-BB. For the individual water mass pathways, the $\overline{\Delta O_2}$ generated within
 406 the OMZs is typically only around 10-30%, with the exception of the AS-BB OMZ where
 407 these values are between 20 and 63%. The water masses originating at high latitudes and
 408 characterized by longer transit times tend to have a smaller fraction of the oxygen-deficit
 409 generated inside the OMZs compared to those with shorter transit times. However, these
 410 differences are generally small and, for almost every pathway, most of the oxygen is con-
 411 sumed in three regions (when including OMZs): 1) in the water mass formation regions
 412 themselves, 2) in the subtropics and tropics, and 3) in the Subantarctic region. The depth
 413 of the pathway relative to the remineralization profile determines the oxygen consump-
 414 tion in each region.

415 It is well known that most of the remineralization occurs in the upper 1000 m of
 416 the water column, as organic particles sink. The most labile particles are rapidly rem-
 417 mineralized in the upper ocean, while only the most refractory particles reach the bottom
 418 (Martin et al., 1987; DeVries & Weber, 2017). This is reflected in the attenuation of par-
 419 ticulate carbon fluxes, that follow a power law distribution known as the Martin curve
 420 (Martin et al., 1987). When the global ocean is taken as destination Ω , the TMI con-
 421 forms to the general remineralization profile, having its largest oxygen sinks around 500
 422 m. About 39% of the global oxygen utilization, $\overline{\Delta O_2}$, occurs in the upper 1000 m, close
 423 to the 44% occurring at 1000-3000 m, with a substantial 17% taking place below 3000
 424 m (Figure S4), which is in excellent agreement with the 18% estimated by Holzer (2022).
 425 However, the shape of the curve is not identical in every region as a result of the rela-
 426 tionship between the remineralization rate and temperature and oxygen (DeVries & We-
 427 ber, 2017). As such, in colder regions, the remineralization rate is slower because of a
 428 lower metabolic index, and as a result, the curve is more gentle than in warmer regions
 429 (Marsay et al., 2015). Similarly, in regions where oxygen is not available, such as the OMZs,
 430 the metabolic index also decreases and the remineralization curve is more gentle (Devol
 431 & Hartnett, 2001). Cold and oxygen-depleted regions thus translate into high transfer
 432 efficiency, i.e., the fraction of particulate carbon export that survives remineralization
 433 above 1000 m (DeVries & Weber, 2017). The general remineralization profiles for the
 434 oxygen-deficit in the OMZs (the along-path oxygen utilization $\overline{\Delta O_2}$ when OMZs are Ω),
 435 also show the characteristic power law distribution from the Martin curve. Individual
 436 pathways, however, vary substantially. High latitude cold endmembers, such as the Antarc-
 437 tic and North Atlantic show a more depth-independent $\overline{\Delta O_2}$ profile. Conversely, in
 438 the tropical and subtropical pathways, remineralization occurs mostly in the upper ocean.
 439 Thus, the presence of colder waters allows a larger, deeper export of carbon and rem-
 440 ineralization.

441 Because most of the $\overline{\Delta O_2}$ occurs in the upper 1000 m, if the pathway for an en-
 442 dmember lies below the remineralization curve (Figure 9) the oxygen would be relatively
 443 preserved until resurfacing. This is the case for distant endmembers - e.g, the North At-
 444 lantic, where the largest concentration of $\overline{\Delta O_2}$ are at the OMZs (Figure S5, S6, S7 and
 445 S8). This preservation of oxygen reinforces the idea that, in steady-state, OMZs are pri-
 446 marily set by the geometry of the oceanic pathways that upwell old water with relatively
 447 low-oxygen concentrations to the OMZs, where the final remineralization and push to-
 448 wards suboxic ($<20 \mu\text{mol kg}^{-1}$) conditions occur.

449 4 Discussion

450 Our results agree well with other studies that use similar approaches to either de-
 451 termine the ventilation times-scales of OMZs or determine the fate of the oxygen in the
 452 ocean. Fu, Bardin, and Primeau (2018) used a transport matrix based on a General Cir-
 453 culation Model to determine the mixed layer ventilation regions of OMZs. While the gen-
 454 eral pattern of our results in terms of both volume and timescales agree with theirs, there
 455 are differences regarding the importance and formation regions of Antarctic Bottom Wa-
 456 ter. We estimate that more than 20% of the water in the ETSP and ETNP correspond
 457 to Antarctic endmembers while Fu, Bardin, and Primeau (2018) estimated that only 3.8%
 458 and 8.1%, respectively, was formed south of 55°S. The spatial pattern also differs. While
 459 the Antarctic Bottom Water formation in the TMI occurs in the Ross and Weddell Sea,
 460 in Fu, Bardin, and Primeau (2018) it occurs exclusively along the shelf. This difference
 461 might be due to an incomplete model spin-up (Fu, Bardin, & Primeau, 2018) but more
 462 generally it is likely also related to how the Antarctic Bottom Water is represented in
 463 models, as Earth System Models struggle to correctly represent the formation of Antarc-
 464 tic Bottom Water, and also North Atlantic Deep Water (Heuzé, 2017, 2021). In partic-
 465 ular, although the CESM model used to construct the transport matrix in Fu, Bardin,
 466 and Primeau (2018) correctly represents bottom water properties, its Pacific Meridional

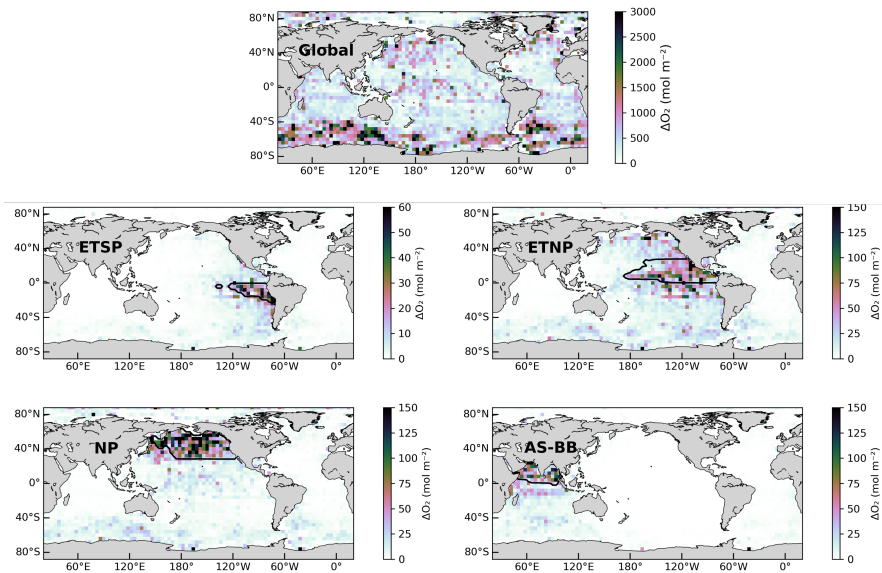


Figure 7. Vertically integrated $\overline{\Delta O_2}$ along the path that connects the global mixed layer with the global interior ocean and with each of the OMZs.

467 Overturning Circulation is too shallow (Supplementary Material in Cabré et al., 2015)
 468 compared to observations (Holzer et al., 2021). The TMI uses observations directly to
 469 constrain the advective-diffusive transport, and the ventilation pathways, and water mass
 470 fractions of both the Antarctic Bottom Water and the North Atlantic Deep Water are
 471 comparable to other observation-based estimates (DeVries & Primeau, 2011; Gebbie &
 472 Huybers, 2010; Holzer et al., 2021). In the NP OMZ, our estimates of the fractions of
 473 Antarctic Bottom Water and North Atlantic Deep Water agree well with the recent es-
 474 timates by Holzer et al. (2021), who argue that regions such as the Shadow Zone in the
 475 North Pacific to a large extent is ventilated by Antarctic Bottom Water and North At-
 476 lantic Deep Water and controlled by diffusion. Most importantly, Fu, Bardin, and Primeau
 477 (2018) quantified only the transport of volume, while here we also determine the trans-
 478 port of oxygen and oxygen-deficit.

479 The fate of the oxygen in the ocean was recently explored by Holzer (2022) who
 480 determined the origins of the oxygen-deficit in the interior ocean based on the OCIM2
 481 transport matrix (DeVries & Holzer, 2019). While some of their results are directly com-
 482 parable to ours, there are a few key differences that are worth pointing out. The TMI
 483 estimates the total oxygen-deficit in each interior location ($\overline{\Delta O_2}$) directly from the tracer
 484 distributions, whereas Holzer (2022) estimated $\overline{\Delta O_2}$ by tracing True Oxygen Utilization
 485 (TOU) back in time by reversing the advective-diffusive transport. Thus, both studies
 486 converge on the same solution but start at opposite ends. In addition, the biogeochem-
 487 ical model used by Holzer (2022) is parameterized with a Martin power law with a glob-
 488 ally uniform exponent and therefore there are no spatial variations in particle transfer
 489 efficiency. Our remineralization pathways and the along-path oxygen utilization presented
 490 in Section 3.2 are equivalent to Figure 5 in Holzer (2022). Both show a very similar pat-
 491 tern and magnitude. The strongest oxygen loss occurs in OMZs because the fraction of
 492 volume that would reach the OMZs is also higher. Contrarily, afar from the OMZs, the

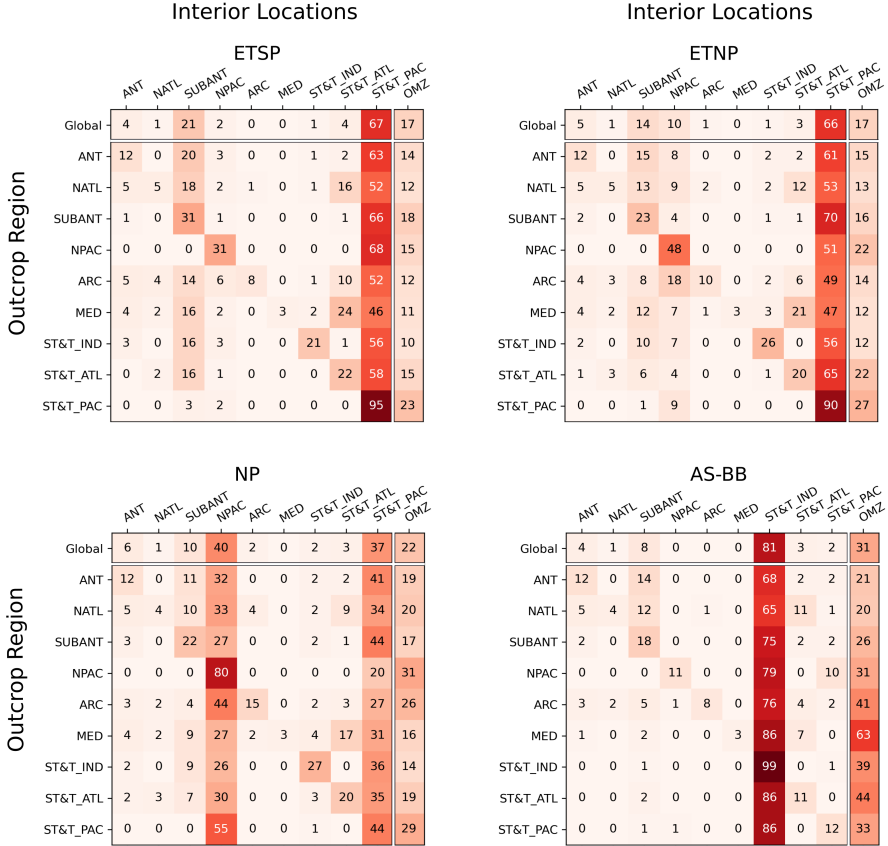


Figure 8. Regional oxygen consumption along the pathways from outcrop regions to each of the OMZs, $\Delta\bar{O}_2$, as a percentage of the total pathway integrated deficit. Every row sums to 100% (excluding rounding errors) and includes consumption within the OMZs. The percentage of the remineralization that occurs within the OMZs is added as an extra column. The selected outcrop regions are the Antarctic (ANT), North Atlantic (NATL), Subantarctic (SUBANT), North Pacific (NPAC), Arctic (ARC), Mediterranean Sea (MED), Subtropical and Tropical Indian (ST&T_IND), Subtropical and Tropical Atlantic (ST&T_ATL) and Subtropical and Tropical Pacific (ST&T_PAC).

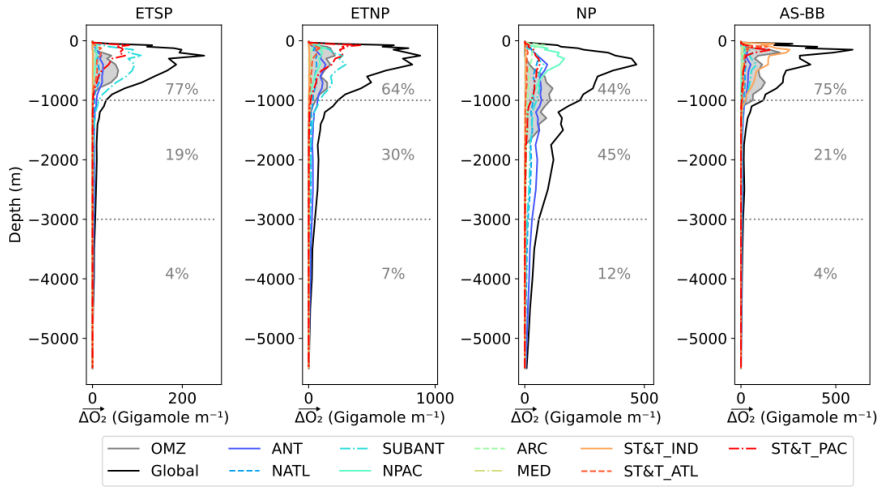


Figure 9. Along-path oxygen utilization ($\overrightarrow{\Delta O_2}$) per meter depth for each specific pathway for each endmember, globally integrated. The colours indicate the different endmembers and grey shading represents the $\overrightarrow{\Delta O_2}$ that occurs within the OMZ, while the numbers indicate the percentage of the total $\overrightarrow{\Delta O_2}$ originating at each of the depth intervals. The endmembers selected are the Antarctic (ANT), North Atlantic (NATL), Subantarctic (SUBANT), North Pacific (NPAC), Arctic (ARC), Mediterranean Sea (MED), Subtropical and Tropical Indian (ST&T_IND), Subtropical and Tropical Atlantic (ST&T_ATL) and Subtropical and Tropical Pacific (ST&T_PAC).

493 fraction of volume at each grid cell that reaches the OMZs is much lower (Figure S3) which
 494 results in a smaller ΔO_2 per grid cell. However, when this is integrated, the total amount
 495 of oxygen-deficit is larger than the one originating in the OMZs. Our results also show
 496 that, surprisingly, the North Atlantic and Arctic contribute substantially to the oxygen
 497 in the NP OMZ (Figure 4). This is also supported by Holzer (2022) who found substan-
 498 tial fluxes of atmospheric oxygen into the North Atlantic that is bound to be utilized within
 499 the North Pacific Hypoxic Zone.

500 While it is clear that OMZs are expanding (Stramma et al., 2010; Zhou et al., 2022),
 501 the driving mechanisms are still an area of active research. The warming of the surface
 502 ocean impacts the oxygen concentrations directly by decreasing the solubility of oxygen,
 503 and indirectly by increasing ocean stratification. Approximately 15% of the observed oxy-
 504 gen loss is explained by the warming of the mixed layer (Helm et al., 2011). The response
 505 of OMZs to warming must unfold on decadal to centennial timescales according their ven-
 506 tilation timescales identified here. This might be a reason why the changes in dissolved
 507 oxygen and temperature for the last decade are not correlated (Stramma & Schmidtko,
 508 2021), indicating that changes in biology and/or circulation dominate (Ito et al., 2016).
 509 As we show here, in steady-state, OMZs are most sensitive to changes in remineraliza-
 510 tion in the Subtropical and Tropical waters (Figure 7), but nevertheless, remote large-
 511 scale changes (especially in the Southern Ocean) would still impact greatly, albeit on longer
 512 timescales (Keller et al., 2016). This also has important implications as Subtropical gyres
 513 and the Southern Ocean are regions where iron fertilization is considered as a Carbon
 514 Dioxide Removal (CDR) strategy (Yoon et al., 2018; Oschlies et al., 2010). The increased
 515 remineralization resulting from fertilization would eventually increase the oxygen defi-
 516 ciency in the already oxygen-depleted OMZs.

517 While we believe the TMI gives an appropriate representation of the origins of OMZs,
 518 despite the differences in the modelled and observed OMZs, a number of improvements
 519 should be made to better fit the observations. Flexible stoichiometric ratios would al-
 520 low the TMI to constrain the impacts of remineralization in suboxic environments more
 521 accurately. Additionally, pointwise observations could be used instead of relying on al-
 522 ready gridded products that might transfer their own biases to the TMI. With enough
 523 observations, a higher resolution TMI could be constrained, which would also improve
 524 the pathways (Brakstad et al., 2023). In addition, the TMI is a steady-state approach
 525 and the findings presented here should be taken as such, i.e., no variability or feedbacks
 526 are accounted for. Constraining a seasonally varying TMI could allow primary produc-
 527 tion and water mass formation to co-vary, thus providing further insights on impacts of
 528 circulation and primary production on OMZs. Similarly, constraining circulation at decadal
 529 frequencies might enable investigations of these processes in the context of a changing
 530 climate. The global decadal repeat hydrography programme GO-SHIP, as well as the
 531 Biogeochemical Argo program, may provide the necessary observations for such a pur-
 532 pose. A special focus should be placed on deep measurements, as such observations are
 533 needed to shed further light on the old and cold remote origins of OMZs.

534 5 Conclusions

535 In this study, we show that the world’s OMZs are ventilated by mode, intermedi-
 536 ate and deep waters formed at high latitudes. Of particular importance are the Subantarctic
 537 region (by means of the Mode/Intermediate Waters) and the Antarctic region (via
 538 Antarctic Bottom Water; Table 1). These waters supply up to half of the volume for ev-
 539 ery OMZ in the Pacific (and to a lesser extent to the AS-BB OMZ). However, OMZs are
 540 mostly oxygenated by Subtropical and Tropical, Subantarctic Mode/Intermediate and
 541 North Pacific Intermediate waters, on decadal to centennial timescales, respectively. High-
 542 latitude endmembers, Antarctic regions and the North Atlantic ventilate OMZs on longer
 543 (millennial) timescales and most of the oxygen is utilized upon arrival to the subtrop-
 544 ical and tropical regions. These waters thus contribute to most of the volume and have

Table 1. Percent volume, oxygen and oxygen-deficit contributions to each OMZ from each source region: Antarctic Marginal Seas (ANT), North Atlantic (NATL), Subantarctic (SUBANT), North Pacific (NPAC), Arctic (ARC), Mediterranean (MED), Subtropics and Tropics (ST&T). ST&T is the sum of contributions from the Atlantic, Pacific and Indian Subtropical and Tropical basins.

Volume (%)	ETSP	ETNP	NP	AS-BB
ANT	17	24	31	17
NATL	8	11	16	9
SUBANT	46	30	15	16
NPAC	2	8	17	1
ARC	2	3	6	5
MED	0	1	1	4
ST&T	24	24	14	47

Oxygen (%)	ETSP	ETNP	NP	AS-BB
ANT	3	4	1	1
NATL	0	3	14	1
SUBANT	67	23	0	13
NPAC	1	30	50	2
ARC	0	3	17	29
MED	0	0	0	7
ST&T	28	38	18	57

Oxygen Utilized (%)	ETSP	ETNP	NP	AS-BB
ANT	20	27	35	20
NATL	10	13	18	12
SUBANT	45	30	16	18
NPAC	3	7	14	1
ARC	2	3	6	5
MED	0	0	1	4
ST&T	18	18	11	41

545 relatively low oxygen concentrations. Therefore they contribute strongly to the oxygen-
 546 deficit of OMZs. Our results are in agreement with earlier studies that suggested that
 547 OMZs are set by the transport of low-oxygen waters into OMZs (Olson et al., 1993; Czeschel
 548 et al., 2011; Sonnerup et al., 2019).

549 Here, we propose a mechanism that summarises the formation of the oxygen-deficit
 550 in the OMZs in steady-state (i.e., without changes in solubility or biology). Only a small
 551 quantity of oxygen is utilized in the formation regions at high latitudes, where waters
 552 are subducted. Due to the long pathways that pass through the deep ocean, the rela-
 553 tively low oxygen utilization adds up to about half of the oxygen-deficit before these wa-
 554 ters reach the Subtropical and Tropical regions. Here, in the Tropical and Subtropical
 555 regions, originates most of the oxygen-deficit, with the strongest oxygen utilization oc-
 556 ccurring within the OMZs upon upwelling. This is also the case for remote endmembers
 557 (e.g. North Atlantic) that preserve substantial amounts of oxygen that are only utilized
 558 when reaching the OMZs. Thus, our study highlights the delicate balance in oxygen loss
 559 that results in the OMZs, where the oxygen-deficit originating away from the OMZs is
 560 of similar magnitude to that originating around (subtropics and tropics) and within the
 561 OMZs. Our results suggest that the OMZs are set by the geometry of the ocean circula-
 562 tion pathways that upwell old and relatively low-oxygen waters, however, the presented
 563 pattern may change as a result of changes in solubility and biology due to the changing
 564 climate.

565 Acronyms

566 **OMZ** Oxygen Minimum Zone
 567 **ETSP** East Tropical South Pacific
 568 **ETNP** East Tropical North Pacific
 569 **NP** North Pacific
 570 **AS-BB** Arabian Sea - Bay of Bengal

571 Open Research Section

572 The TMI transport matrix as well as the tracers distributions that are used to gener-
 573 ate the results in this paper are available in GitHub (<https://github.com/ggebbie/TMI.jl>).

574 Acknowledgments

575 We thank three anonymous reviewers for their careful and constructive reviews. XD was
 576 supported by a PhD research fellowship from the University of Bergen. AO and SKL ap-
 577 preciate the support from the Research Council of Norway (ICOS-Norway, project num-
 578 ber 245972) and OceanICU, Improving Carbon Understanding funded by the Horizon
 579 Europe research and innovation program under grant agreement No 101083922. ELM
 580 was supported by UKRI grants Atlantic Biogeochemical (ABC) fluxes (ref no. NE/M005046/2)
 581 and TICTOC:Transient tracer-based Investigation of Circulation and Thermal Ocean
 582 Change (ref no. NE/P019293/2). AB was supported by the Trond Mohn Foundation un-
 583 der grant agreement BFS2016REK01. GG was supported by U.S. NSF Grant 88075300.

584 References

- 585 Anderson, L. A., & Sarmiento, J. L. (1994). Redfield ratios of remineralization deter-
 586 mined by nutrient data analysis. *Global Biogeochemical Cycles*, 8(1), 65–80.
 587 doi: <https://doi.org/10.1029/93GB03318>
- 588 Bianchi, D., Dunne, J. P., Sarmiento, J. L., & Galbraith, E. D. (2012). Data-based
 589 estimates of suboxia, denitrification, and N₂O production in the ocean and

- 590 their sensitivities to dissolved O₂. *Global Biogeochemical Cycles*, 26(March),
 591 1–13. doi: 10.1029/2011GB004209
- 592 Brakstad, A., Gebbie, G., Våge, K., Jeansson, E., & Ólafsdóttir, S. R. (2023,
 593 March). Formation and pathways of dense water in the Nordic Seas based
 594 on a regional inversion. *Progress in Oceanography*, 212, 102981. Retrieved
 595 2023-04-18, from [https://www.sciencedirect.com/science/article/pii/](https://www.sciencedirect.com/science/article/pii/S0079661123000241)
 596 S0079661123000241 doi: 10.1016/j.pocean.2023.102981
- 597 Busecke, J. J. M., Resplandy, L., Ditkovsky, S. J., & John, J. G. (2022). Diverging
 598 Fates of the Pacific Ocean Oxygen Minimum Zone and Its Core in a Warming
 599 World. *AGU Advances*, 3(6), e2021AV000470. Retrieved 2023-05-08, from
 600 <https://onlinelibrary.wiley.com/doi/abs/10.1029/2021AV000470> doi:
 601 10.1029/2021AV000470
- 602 Cabré, A., Marinov, I., Bernardello, R., & Bianchi, D. (2015). Oxygen mini-
 603 mum zones in the tropical Pacific across CMIP5 models: Mean state differ-
 604 ences and climate change trends. *Biogeosciences*, 12(18), 5429–5454. doi:
 605 10.5194/bg-12-5429-2015
- 606 Carter, B. R., Feely, R. A., Lauvset, S. K., Olsen, A., DeVries, T., & Sonnerup,
 607 R. (2021). Preformed Properties for Marine Organic Matter and Carbonate
 608 Mineral Cycling Quantification. *Global Biogeochemical Cycles*, 35(1). doi:
 609 10.1029/2020GB006623
- 610 Czeschel, R., Stramma, L., Schwarzkopf, F. U., Giese, B. S., Funk, A., &
 611 Karstensen, J. (2011). Middepth circulation of the eastern tropical South
 612 Pacific and its link to the oxygen minimum zone. *Journal of Geophysical*
 613 *Research: Oceans*, 116(1), 1–13. doi: 10.1029/2010JC006565
- 614 De Lavergne, C., Madec, G., Roquet, F., Holmes, R. M., & McDougall, T. J. (2017).
 615 Abyssal ocean overturning shaped by seafloor distribution. *Nature*, 551(7679),
 616 181–186. (Publisher: Nature Publishing Group) doi: 10.1038/nature24472
- 617 Deutsch, C., Brix, H., Ito, T., Frenzel, H., & Thompson, L. (2011). Climate-Forced
 618 Variability of Ocean Hypoxia. *Science*, 333(6040), 336–339. doi: 10.1126/
 619 science.1202422
- 620 Devol, A. H., & Hartnett, H. E. (2001). Role of the oxygen-deficient zone in trans-
 621 fer of organic carbon to the deep ocean. *Limnology and Oceanography*, 46(7),
 622 1684–1690. Retrieved 2023-03-30, from [https://onlinelibrary.wiley.com/](https://onlinelibrary.wiley.com/doi/abs/10.4319/lo.2001.46.7.1684)
 623 [doi/abs/10.4319/lo.2001.46.7.1684](https://onlinelibrary.wiley.com/doi/abs/10.4319/lo.2001.46.7.1684) doi: 10.4319/lo.2001.46.7.1684
- 624 DeVries, T., Deutsch, C., Primeau, F., Chang, B., & Devol, A. (2012). Global rates
 625 of water-column denitrification derived from nitrogen gas measurements. *Nature*
 626 *Geoscience*, 4(August), 547–550. (Publisher: Nature Publishing Group)
 627 doi: 10.1038/ngeo1515
- 628 DeVries, T., & Holzer, M. (2019). Radiocarbon and Helium Isotope Constraints on
 629 Deep Ocean Ventilation and Mantle-3He Sources. *Journal of Geophysical Re-*
 630 *search: Oceans*, 124(5), 3036–3057. doi: 10.1029/2018JC014716
- 631 DeVries, T., & Primeau, F. (2011). Dynamically and observationally constrained
 632 estimates of water-mass distributions and ages in the global ocean. *Journal of*
 633 *Physical Oceanography*, 41(12), 2381–2401. doi: 10.1175/JPO-D-10-05011.1
- 634 DeVries, T., & Weber, T. (2017). The export and fate of organic matter in the
 635 ocean: New constraints from combining satellite and oceanographic tracer
 636 observations. *Global Biogeochemical Cycles*, 31(3), 535–555. Retrieved
 637 2023-03-30, from [https://onlinelibrary.wiley.com/doi/abs/10.1002/](https://onlinelibrary.wiley.com/doi/abs/10.1002/2016GB005551)
 638 2016GB005551 doi: 10.1002/2016GB005551
- 639 Frölicher, T. L., Ashwanden, M. T., Gruber, N., Jaccard, S. L., Dunne, J. P., &
 640 Paynter, D. (2020). Contrasting Upper and Deep Ocean Oxygen Response
 641 to Protracted Global Warming. *Global Biogeochemical Cycles*, 34(8). doi:
 642 10.1029/2020GB006601
- 643 Fu, W., Bardin, A., & Primeau, F. (2018). Tracing ventilation source of tropical
 644 pacific oxygen minimum zones with an adjoint global ocean transport model.

- 645 *Deep-Sea Research Part I: Oceanographic Research Papers*, 139(November
646 2017), 95–103. (Publisher: Elsevier Ltd) doi: 10.1016/j.dsr.2018.07.017
- 647 Fu, W., Primeau, F., Keith Moore, J., Lindsay, K., & Randerson, J. T. (2018).
648 Reversal of Increasing Tropical Ocean Hypoxia Trends With Sustained
649 Climate Warming. *Global Biogeochemical Cycles*, 32(4), 551–564. doi:
650 10.1002/2017GB005788
- 651 Fuenzalida, R., Schneider, W., Garcés-Vargas, J., Bravo, L., & Lange, C. (2009).
652 Vertical and horizontal extension of the oxygen minimum zone in the eastern
653 South Pacific Ocean. *Deep Sea Research Part II: Topical Studies in Oceanogra-
654 phy*, 56(16), 992–1003. doi: <https://doi.org/10.1016/j.dsr2.2008.11.001>
- 655 Gebbie, G., & Huybers, P. (2010). Total Matrix Intercomparison: A Method for
656 Determining the Geometry of Water-Mass Pathways. *Journal of Physical
657 Oceanography*, 40(8), 1710–1728. doi: 10.1175/2010jpo4272.1
- 658 Gebbie, G., & Huybers, P. (2011). How is the ocean filled? *Geophysical Research
659 Letters*, 38(February), 1–5. doi: 10.1029/2011GL046769
- 660 Gebbie, G., & Huybers, P. (2012). The Mean Age of Ocean Waters Inferred from
661 Radiocarbon Observations: Sensitivity to Surface Sources and Accounting for
662 Mixing Histories. *Journal of Physical Oceanography*, 42(2), 291–305. doi:
663 10.1175/jpo-d-11-0043.1
- 664 Gouretski, V., & Koltermann, K. P. (2004). WOCE global hydrographic climatol-
665 ogy. *Berichte des Bundesamtes fu r Seeschifffahrt und Hydrographie Tech. Rep.
666 35, digital media.*
- 667 Gray, J. S., Wu, R. S. S., & Ying, Y. O. (2002). Effects of hypoxia and organic en-
668 richment on the coastal marine environment. *Marine Ecology Progress Series*,
669 238, 249–279. doi: 10.3354/meps238249
- 670 Haine, T. W., & Hall, T. M. (2002). A generalized transport theory: Water-mass
671 composition and age. *Journal of Physical Oceanography*, 32(6), 1932–1946.
672 doi: 10.1175/1520-0485(2002)032<1932:AGTTWM>2.0.CO;2
- 673 Helly, J. J., & Levin, L. A. (2004). Global distribution of naturally occurring ma-
674 rine hypoxia on continental margins. *Deep Sea Research Part I: Oceanographic
675 Research Papers*, 51(9), 1159–1168. doi: <https://doi.org/10.1016/j.dsr.2004.03>
676 .009
- 677 Helm, K. P., Bindoff, N. L., & Church, J. A. (2011). Observed decreases in oxygen
678 content of the global ocean. *Geophysical Research Letters*, 38(23), 1–6. doi: 10
679 .1029/2011GL049513
- 680 Heuzé, C. (2017). North Atlantic deep water formation and AMOC in CMIP5 mod-
681 els. *Ocean Science Discussions*, 1–22. doi: 10.5194/os-2017-2
- 682 Heuzé, C. (2021). Antarctic Bottom Water and North Atlantic Deep Water in
683 CMIP6 models. *Ocean Science*, 17(1), 59–90. doi: 10.5194/os-17-59-2021
- 684 Holzer, M. (2022). The Fate of Oxygen in the Ocean and Its Sensitivity to Local
685 Changes in Biological Production. *Journal of Geophysical Research: Oceans*,
686 127(8). doi: 10.1029/2022jc018802
- 687 Holzer, M., DeVries, T., & de Lavergne, C. (2021, July). Diffusion controls the ven-
688 tilation of a Pacific Shadow Zone above abyssal overturning. *Nature Commu-
689 nications*, 12(1), 4348. Retrieved 2023-03-27, from [https://www.nature.com/
690 articles/s41467-021-24648-x](https://www.nature.com/articles/s41467-021-24648-x) (Number: 1) doi: 10.1038/s41467-021-24648
691 -x
- 692 Ito, T., Follows, M. J., & Boyle, E. A. (2004). Is AOU a good measure of respira-
693 tion in the oceans? *Geophysical Research Letters*, 31(17), 1–4. doi: 10.1029/
694 2004GL020900
- 695 Ito, T., Nenes, A., Johnson, M. S., Meskhidze, N., & Deutsch, C. (2016). Accelera-
696 tion of oxygen decline in the tropical Pacific over the past decades by aerosol
697 pollutants. *Nature Geoscience*, 9(6), 443–447. doi: 10.1038/ngeo2717
- 698 Johnson, G. C. (2008). Quantifying Antarctic Bottom Water and North Atlantic
699 Deep Water volumes. *Journal of Geophysical Research: Oceans*, 113(C5). doi:

- 700 <https://doi.org/10.1029/2007JC004477>
- 701 Jones, D. C., Meijers, A. J. S., Shuckburgh, E., Sallée, J.-B., Haynes, P., McAufield,
702 E. K., & Mazloff, M. R. (2016, September). How does Subantarctic Mode
703 Water ventilate the Southern Hemisphere subtropics? *Journal of Geophysical*
704 *Research: Oceans*, *121*(9), 6558–6582. doi: 10.1002/2016JC011680
- 705 Kalvelage, T., Lavik, G., Lam, P., Contreras, S., Arteaga, L., Löscher, C. R., ...
706 Kuypers, M. M. M. (2013). Nitrogen cycling driven by organic matter export
707 in the South Pacific oxygen minimum zone. *Nature Geoscience*, *6*(February).
708 (Publisher: Nature Publishing Group) doi: 10.1038/ngeo1739
- 709 Karstensen, J., Stramma, L., & Visbeck, M. (2008). Oxygen minimum zones in the
710 eastern tropical Atlantic and Pacific oceans. *Progress in Oceanography*, *77*(4),
711 331–350. doi: 10.1016/j.pocean.2007.05.009
- 712 Keeling, R. F., & Garcia, H. E. (2002). The change in oceanic O₂ inventory associ-
713 ated with recent global warming. *Proceedings of the National Academy of Sci-*
714 *ences*, *99*(12), 7848–7853. doi: 10.1073/pnas.122154899
- 715 Keeling, R. F., Körtzinger, A., & Gruber, N. (2010). Ocean deoxygenation in a
716 warming world. *Annual Review of Marine Science*, *2*(1), 199–229. doi: 10.
717 .1146/annurev.marine.010908.163855
- 718 Keller, D. P., Kriest, I., Koeve, W., & Oschlies, A. (2016). Southern Ocean bio-
719 logical impacts on global ocean oxygen. *Geophysical Research Letters*, *43*(12),
720 6469–6477. doi: 10.1002/2016GL069630
- 721 Key, R. M., Kozyr, A., Sabine, C. L., Lee, K., Wanninkhof, R., Bullister, J. L., ...
722 Peng, T. H. (2004). A global ocean carbon climatology: Results from Global
723 Data Analysis Project (GLODAP). *Global Biogeochemical Cycles*, *18*(4), 1–23.
724 doi: 10.1029/2004GB002247
- 725 Luyten, J. R., Pedlosky, J., & Stommel, H. (1983). The Ventilated Ther-
726mocline. *Journal of Physical Oceanography*, *13*(2), 292–309. (Pub-
727 lisher: American Meteorological Society Place: Boston MA, USA) doi:
728 10.1175/1520-0485(1983)013<0292:TVT>2.0.CO;2
- 729 Marsay, C. M., Sanders, R. J., Henson, S. A., Pabortsava, K., Achterberg, E. P.,
730 & Lampitt, R. S. (2015, January). Attenuation of sinking particulate
731 organic carbon flux through the mesopelagic ocean. *Proceedings of the*
732 *National Academy of Sciences*, *112*(4), 1089–1094. Retrieved 2023-03-
733 31, from <https://www.pnas.org/doi/10.1073/pnas.1415311112> doi:
734 10.1073/pnas.1415311112
- 735 Martin, J. H., Knauer, G. A., Karl, D. M., & Broenkow, W. W. (1987). VERTEX:
736 carbon cycling in the north east Pacific. *Deep-Sea Res.*, *34*(2), 267–285.
- 737 Olson, D. B., Hitchcock, G. L., Fine, R. A., & Warren, B. A. (1993). Maintenance
738 of the low-oxygen layer in the central Arabian Sea. *Deep-Sea Research Part II*,
739 *40*(3), 673–685. doi: 10.1016/0967-0645(93)90051-N
- 740 Oschlies, A., Koeve, W., Rickels, W., & Rehdanz, K. (2010, December). Side ef-
741 fects and accounting aspects of hypothetical large-scale Southern Ocean iron
742 fertilization. *Biogeosciences*, *7*(12), 4017–4035. Retrieved 2023-04-24, from
743 <https://bg.copernicus.org/articles/7/4017/2010/bg-7-4017-2010.html>
744 doi: 10.5194/bg-7-4017-2010
- 745 Paulmier, A., & Ruiz-Pino, D. (2009, March). Oxygen minimum zones (OMZs) in
746 the modern ocean. *Progress in Oceanography*, *80*(3-4), 113–128. (Publisher:
747 Pergamon) doi: 10.1016/j.pocean.2008.08.001
- 748 Primeau, F., & Holzer, M. (2006). The Ocean’s Memory of the Atmosphere :
749 Residence-Time and Ventilation-Rate Distributions of Water Masses. *Journal*
750 *of Physical Oceanography*, 1439–1456. doi: [https://doi.org/10.1175/](https://doi.org/10.1175/JPO2919.1)
751 [JPO2919.1](https://doi.org/10.1175/JPO2919.1)
- 752 Shimizu, Y., Iwao, T., Yasuda, I., Ito, S. I., Watanabe, T., Uehara, K., ... Nakano,
753 T. (2004). Formation process of North Pacific Intermediate Water revealed by
754 profiling floats set to drift on 26.7 σ_{θ} isopycnal surface. *Journal of Oceanogra-*

- 755 *phy*, 60(2), 453–462. doi: 10.1023/B:JOCE.0000038061.55914.eb
- 756 Sloyan, B. M., Talley, L. D., Chereskin, T. K., Fine, R., & Holte, J. (2010). Antarctic
757 Intermediate Water and Subantarctic Mode Water Formation in the South-
758 east Pacific: The Role of Turbulent Mixing. *Journal of Physical Oceanography*,
759 40(7), 1558–1574. (Publisher: American Meteorological Society Place: Boston
760 MA, USA) doi: 10.1175/2010JPO4114.1
- 761 Smethie, W. M. (1987). Nutrient regeneration and denitrification in low oxygen
762 fjords. *Deep Sea Research Part A, Oceanographic Research Papers*, 34(5-6),
763 983–1006. doi: 10.1016/0198-0149(87)90049-5
- 764 Sonnerup, R. E., Chang, B. X., Warner, M. J., & Mordy, C. W. (2019). Timescales
765 of ventilation and consumption of oxygen and fixed nitrogen in the eastern
766 tropical South Pacific oxygen deficient zone from transient tracers. *Deep-Sea
767 Research Part I: Oceanographic Research Papers*, 151(July), 103080. (Pub-
768 lisher: Elsevier Ltd) doi: 10.1016/j.dsr.2019.103080
- 769 Stramma, L., Johnson, G. C., Firing, E., & Schmidtko, S. (2010). Eastern Pacific
770 oxygen minimum zones: Supply paths and multidecadal changes. *Journal of
771 Geophysical Research: Oceans*, 115(9), 1–12. doi: 10.1029/2009JC005976
- 772 Stramma, L., & Schmidtko, S. (2021). Tropical deoxygenation sites revisited to in-
773 vestigate oxygen and nutrient trends. *Ocean Science*, 17(3), 833–847. doi: 10
774 .5194/os-17-833-2021
- 775 Teng, Y.-C., Primeau, F. W., Moore, J. K., Lomas, M. W., & Martiny, A. C.
776 (2014). Global-scale variations of the ratios of carbon to phosphorus in ex-
777 ported marine organic matter. *Nature Geoscience*, 7(12), 895–898. doi:
778 10.1038/ngeo2303
- 779 Yoon, J.-E., Yoo, K.-C., Macdonald, A. M., Yoon, H.-I., Park, K.-T., Yang, E. J., . . .
780 Kim, I.-N. (2018, October). Reviews and syntheses: Ocean iron fertilization
781 experiments – past, present, and future looking to a future Korean Iron Fertil-
782 ization Experiment in the Southern Ocean (KIFES) project. *Biogeosciences*,
783 15(19), 5847–5889. Retrieved 2023-04-24, from [https://bg.copernicus.org/
784 articles/15/5847/2018/](https://bg.copernicus.org/articles/15/5847/2018/) doi: 10.5194/bg-15-5847-2018
- 785 Zhou, Y., Gong, H., & Zhou, F. (2022). Responses of Horizontally Expanding
786 Oceanic Oxygen Minimum Zones to Climate Change Based on Observations.
787 *Geophysical Research Letters*, 49(6), 1–11. doi: 10.1029/2022GL097724

Supporting Information for "On the Origins of Open Ocean Oxygen Minimum Zones"

Xabier Davila^{1,2}, Are Olsen^{1,2}, Siv K. Lauvset^{3,2}, Elaine L. McDonagh^{3,2,4},

Ailin Brakstad^{1,2}, Geoffrey Gebbie⁵

¹Geophysical Institute, University of Bergen, Norway.

²Bjerknes Centre for Climate Research, Bergen, Norway.

³NORCE Norwegian Research Centre, Bergen, Norway.

⁴National Oceanography Centre, Southampton, UK.

⁵Department of Physical Oceanography, Woods Hole Oceanographic Institution, Woods Hole, MA 02543, USA.

Introduction

Here we expand the information about the mismatch between the observed and modelled oxygen distributions, and the deficit of oxygen generated in each interior grid cell \mathbf{q} . We also further develop the analysis regarding the remineralization pathways $\overrightarrow{\Delta O_2}$, offering a more global perspective and showing the spatial pattern of each of the individual pathways that contribute to the oxygen-deficit in the Oxygen Minimum Zones (OMZs).

Oxygen Distributions

The interior oxygen distributions (Section 2.3) can be obtained through Equation 1 by prescribing a surface boundary condition \mathbf{c}_b of oxygen at the surface boxes s , and given the interior concentrations of utilized oxygen \mathbf{q} estimated by Gebbie and Huybers

(2010). The deficit of oxygen generated in each grid cell \mathbf{q} is constrained by relating the non-conservative tracers (PO_4^{3-} , NO_3^- and O_2) to a single interior remineralization source through a global fixed stoichiometric ratio of P:N:O = 1:15.5:-170 (Anderson & Sarmiento, 1994). The highest \mathbf{q} is located immediately below the mixed layer and mostly just below the subtropical gyres. While the amount of utilized oxygen decreases with depth, according to Martin et al. (1987), in some regions such as the Atlantic sector of the Southern Ocean and North Pacific there are large amounts of oxygen being consumed. Such a pattern likely results from the enhanced transfer efficiency in cold waters and oxygen-depleted waters (Marsay et al., 2015; Devol & Hartnett, 2001; DeVries & Weber, 2017).

The modelled and observed oxygen climatological distributions are comparable, but the modelled concentrations are generally lower than observed (Figure S2). The TMI constrains the circulation flow field and \mathbf{q} within the observational of the climatological data from Gouretski and Koltermann (2004). Deviations from the uncertainty would penalise more the model, however, these can still exist as there is a trade-off between the local and global fit. The misfit between the modelled and the observations are normalized by the observational error and is represented by the z-score (Figure S2). Z-score shows how many times the misfit deviates from the observational error. For the upper ocean, the mismatch is well within observational error but increases with depth. The OMZs, located at 200-1000 m, do not have a particularly large z-score.

Remineralization Pathways

The horizontal pattern of the remineralization pathways, $\overrightarrow{\Delta\text{O}_2}$ in Figure 7, highly depends on the geometry of the ocean -i.e., pathways that different water masses follow en

route to the OMZs (Figure S3). In the cases where the destination is set in an OMZs, \mathbf{v}_{tot} in Equation 6 acts as a path-selector from the total global $\overrightarrow{\Delta O_2}$ (Figure S4).

Global $\overrightarrow{\Delta O_2}$ represents the along-path oxygen utilization from the global surface to anywhere in the ocean. For the global ocean, most of the oxygen is utilized in the Southern Ocean, and to a lesser extent, the North Atlantic, North Pacific and Equatorial Pacific. This pattern is in good agreement with that estimated by Holzer (2022) Yet, our results suggest larger oxygen sinks in the Southern Ocean and smaller in the North Atlantic. Within the first 1000 m, a large fraction of the global $\overrightarrow{\Delta O_2}$ occurs (39%), similar to the levels between 1000 - 3000 m (44%). A significant fraction occurs also in abyssal waters, 18%, which is identical with the 18% estimated by Holzer (2022). However, our results suggest larger oxygen utilization around 2000 m depth, which might be due to larger utilization in the Southern Ocean where the transfer efficiency below 1000 m is high (DeVries & Weber, 2017).

An important note in the global pattern of $\overrightarrow{\Delta O_2}$ is that the OMZs are indistinguishable from the rest of the ocean. Thus, the OMZs result from the geometry of the pathways (Figure S3) rather than the oxygen utilization pattern (Figure S4). This is evident when looking individually at the remineralization pathways from each end-member to each OMZ (Figures S5, S6, S7 and S8). Distant regions such as the North Atlantic preserve a substantial amount of oxygen until reaching the OMZs, where a large fraction of it is utilized upon upwelling at <1000 m.

References

- Anderson, L. A., & Sarmiento, J. L. (1994). Redfield ratios of remineralization determined by nutrient data analysis. *Global Biogeochemical Cycles*, *8*(1), 65–80. doi: <https://doi.org/10.1029/93GB03318>
- Devol, A. H., & Hartnett, H. E. (2001). Role of the oxygen-deficient zone in transfer of organic carbon to the deep ocean. *Limnology and Oceanography*, *46*(7), 1684–1690. Retrieved 2023-03-30, from <https://onlinelibrary.wiley.com/doi/abs/10.4319/lo.2001.46.7.1684> doi: 10.4319/lo.2001.46.7.1684
- DeVries, T., & Weber, T. (2017). The export and fate of organic matter in the ocean: New constraints from combining satellite and oceanographic tracer observations. *Global Biogeochemical Cycles*, *31*(3), 535–555. Retrieved 2023-03-30, from <https://onlinelibrary.wiley.com/doi/abs/10.1002/2016GB005551> doi: 10.1002/2016GB005551
- Gebbie, G., & Huybers, P. (2010). Total Matrix Intercomparison: A Method for Determining the Geometry of Water-Mass Pathways. *Journal of Physical Oceanography*, *40*(8), 1710–1728. doi: 10.1175/2010jpo4272.1
- Gouretski, V., & Koltermann, K. P. (2004). WOCE global hydrographic climatology. *Berichte des Bundesamtes fu r Seeschifffahrt und Hydrographie Tech. Rep. 35, digital media.*
- Holzer, M. (2022). The Fate of Oxygen in the Ocean and Its Sensitivity to Local Changes in Biological Production. *Journal of Geophysical Research: Oceans*, *127*(8). doi: 10.1029/2022jc018802
- Marsay, C. M., Sanders, R. J., Henson, S. A., Pabortsava, K., Achterberg, E. P., &

- Lampitt, R. S. (2015, January). Attenuation of sinking particulate organic carbon flux through the mesopelagic ocean. *Proceedings of the National Academy of Sciences*, *112*(4), 1089–1094. Retrieved 2023-03-31, from <https://www.pnas.org/doi/10.1073/pnas.1415311112> doi: 10.1073/pnas.1415311112
- Martin, J. H., Knauer, G. A., Karl, D. M., & Broenkow, W. W. (1987). VERTEX: carbon cycling in the north east Pacific. *Deep-Sea Res.*, *34*(2), 267–285.

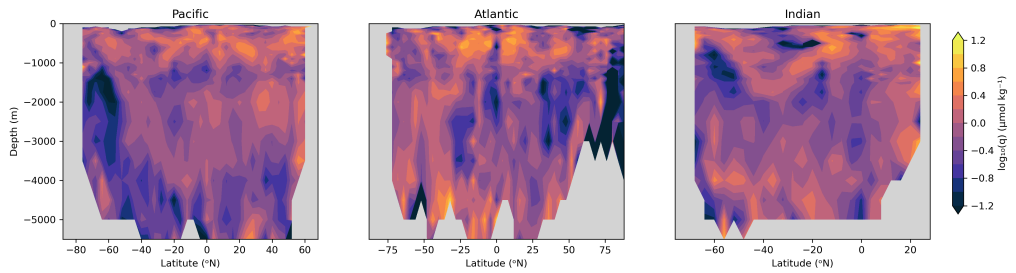


Figure S1. Latitudinally averaged sections for the Pacific, Atlantic and Indian basins for the interior concentrations of utilized oxygen q estimated by Gebbie and Huybers (2010). Note the logarithmic color scale for q .

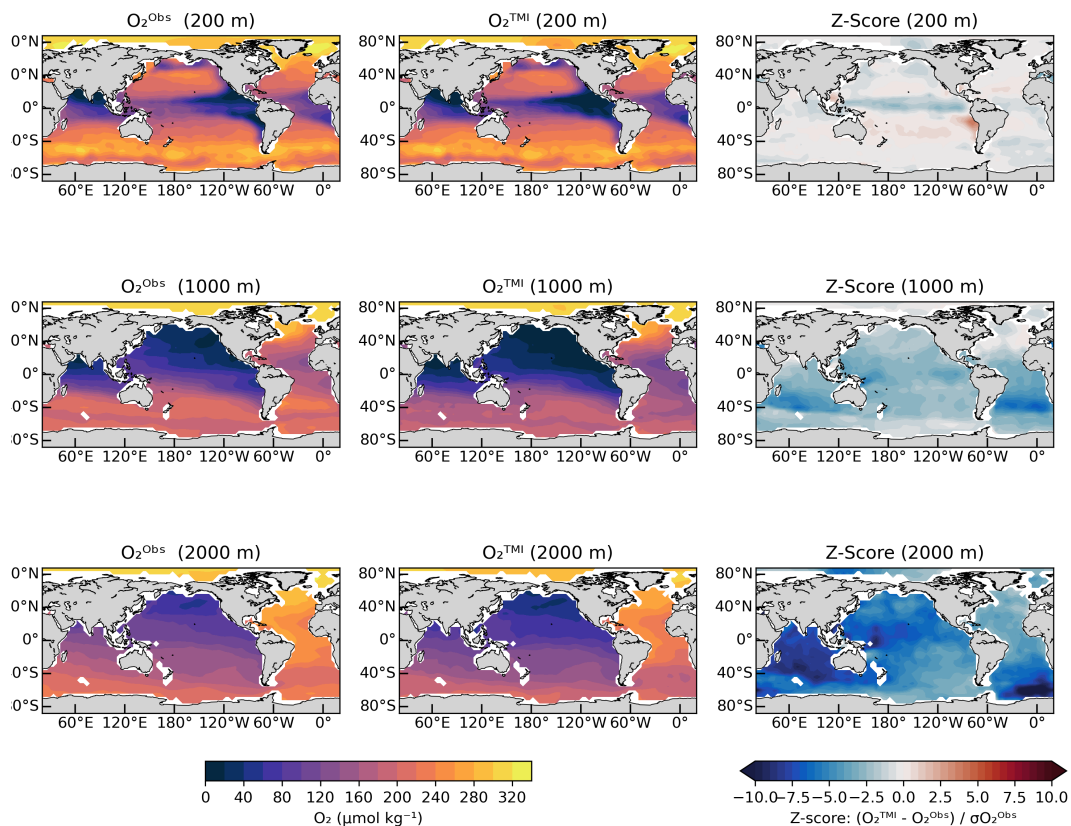


Figure S2. Oxygen concentrations at 200, 1000 and 2000 m from observations (left column) and the TMI (middle column), and their misfit normalized by the uncertainty in the observations (right column; z-score). Z-score shows how many times the mismatch deviates from the uncertainty. The modelled TMI distribution is calculated with equation 1 and assuming a fixed stoichiometric ratio of P:O = 1:-170.

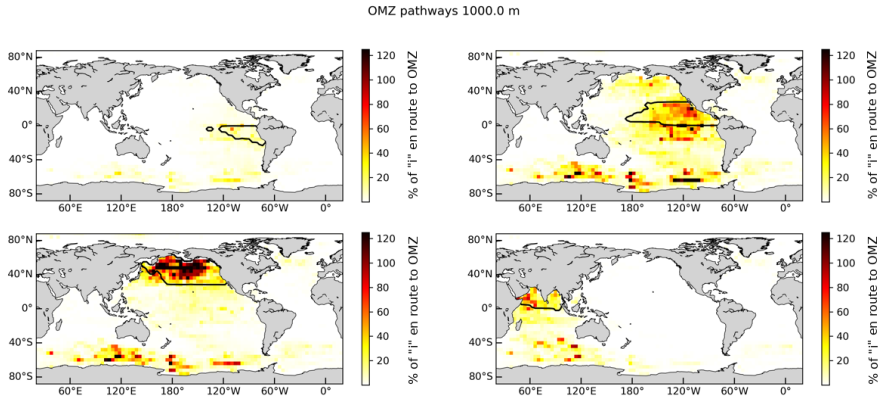


Figure S3. Pathways between the surface and OMZs at 1000 m are calculated as Equation 3. Colorbar indicates the amount of waters that transit a location i in % of volume of i , from the global mixed-layer to the OMZ.

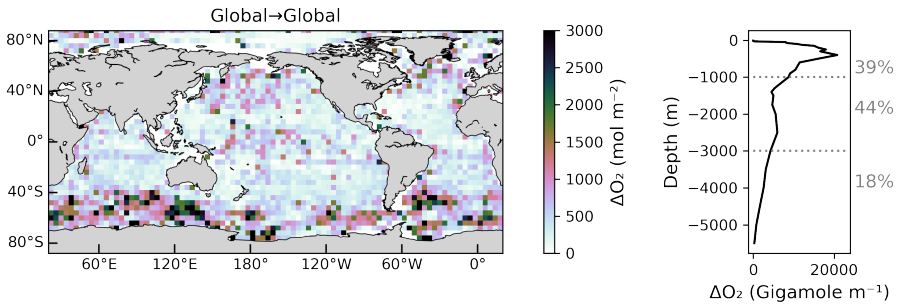


Figure S4. Vertically integrated along-path oxygen utilization for every pathway that connects the surface with every location in the global ocean (left). Vertical profile for the globally integrated along-path oxygen utilization (right), where the numbers indicate the % of the global oxygen-deficit that originates in the each of the levels.

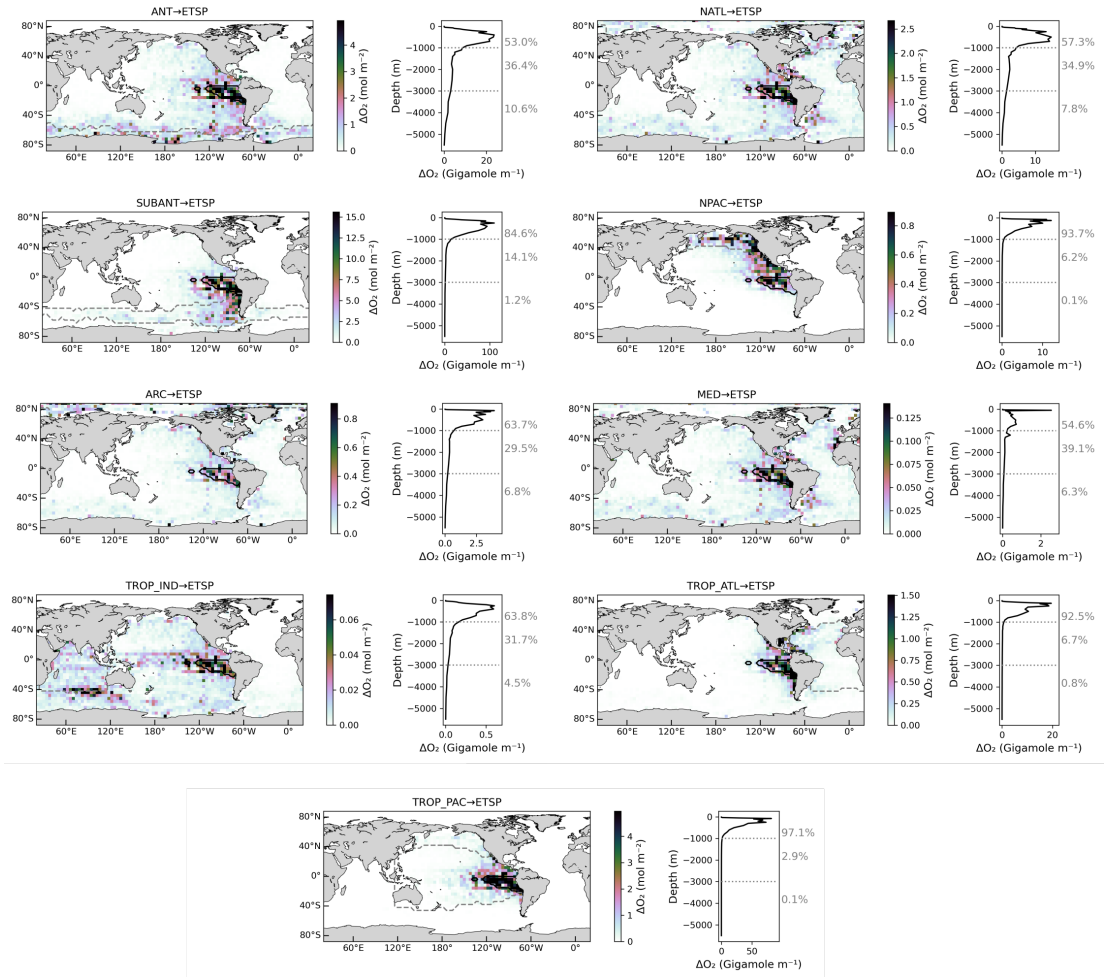


Figure S5. Individual remineralization pathways for each surface region to the Eastern Tropical South Pacific (ETSP) Oxygen Minimum Zone (OMZ) and the globally integrated along-path oxygen utilization profile. The black line indicates the location of the OMZ and the grey dashed line indicate the surface origin of the pathway.

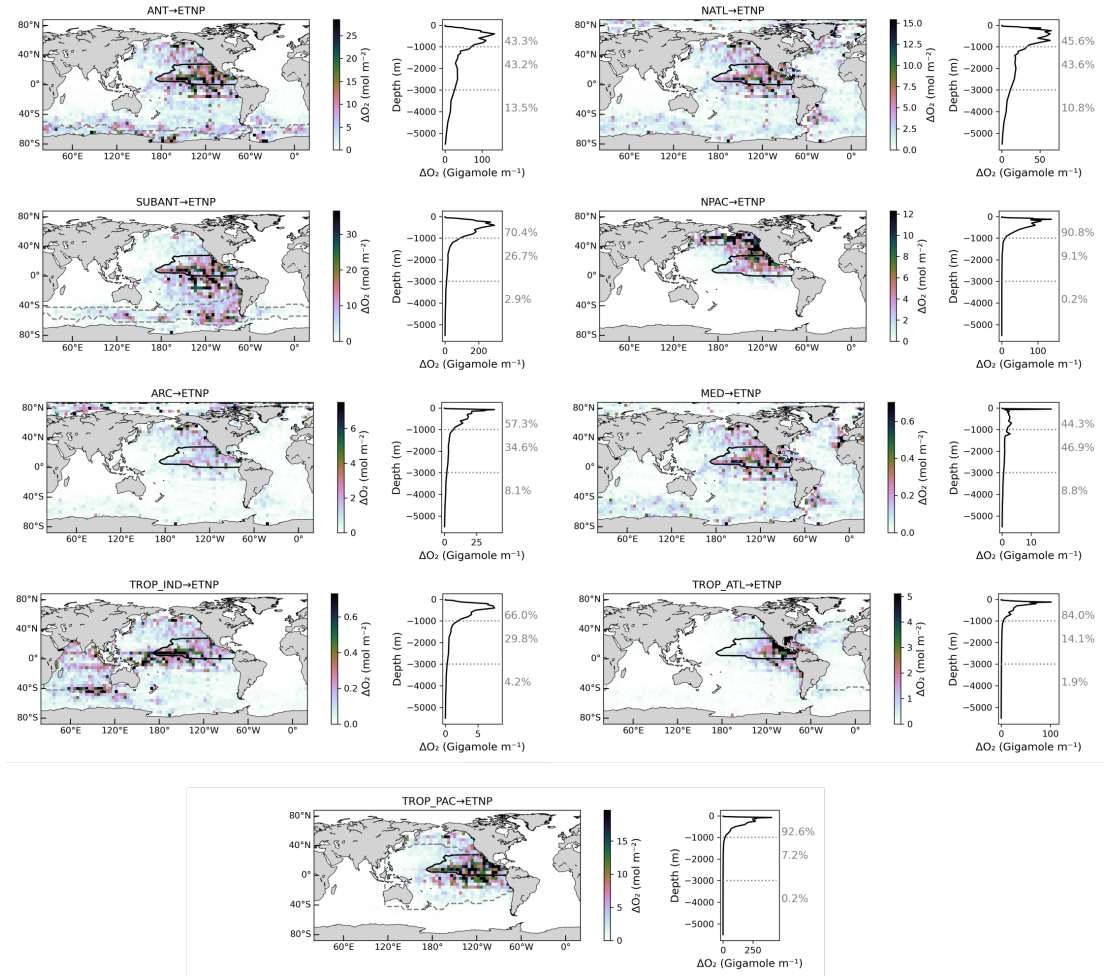


Figure S6. Same as Figure S6 but for Easter Tropical North Pacific (ETNP) Oxygen Minimum Zone.

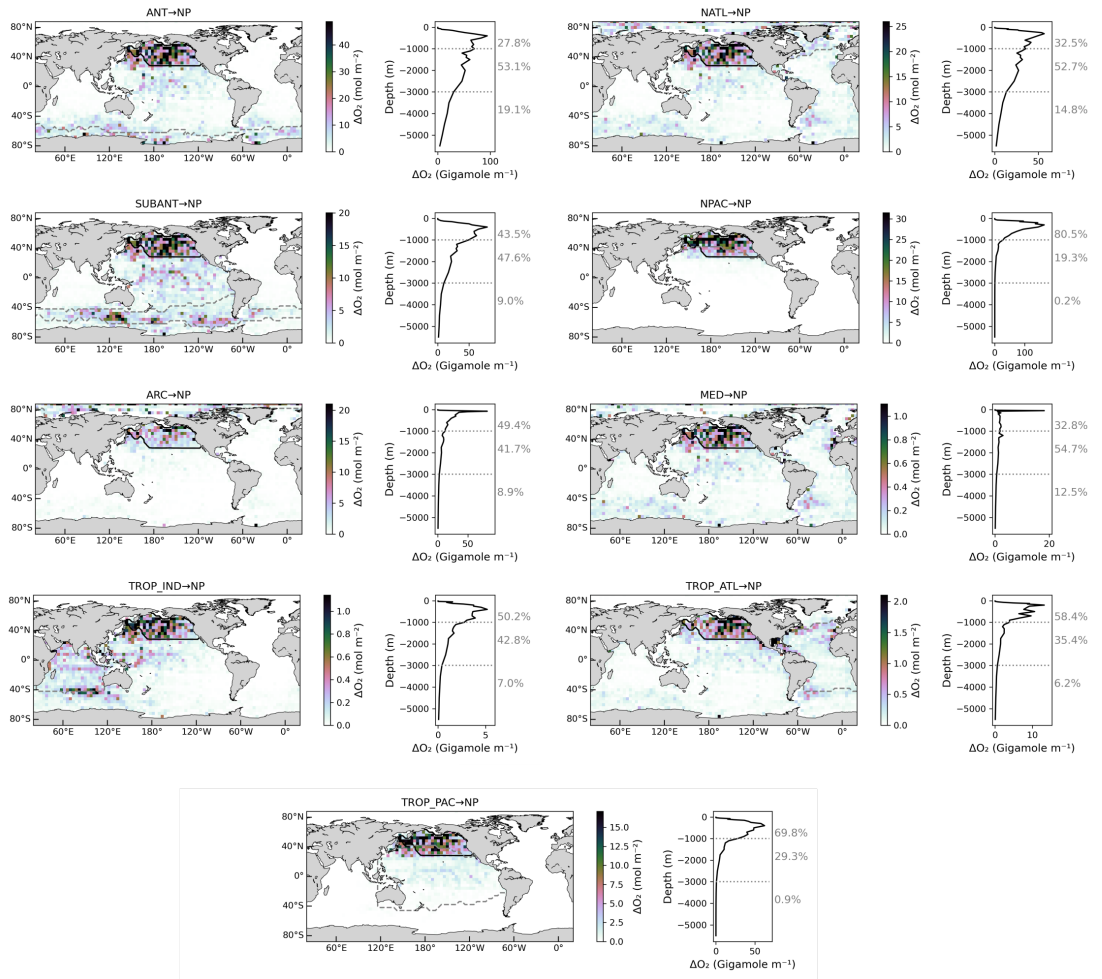


Figure S7. Same as Figure S6 but for North Pacific (NP) Oxygen Minimum Zone.

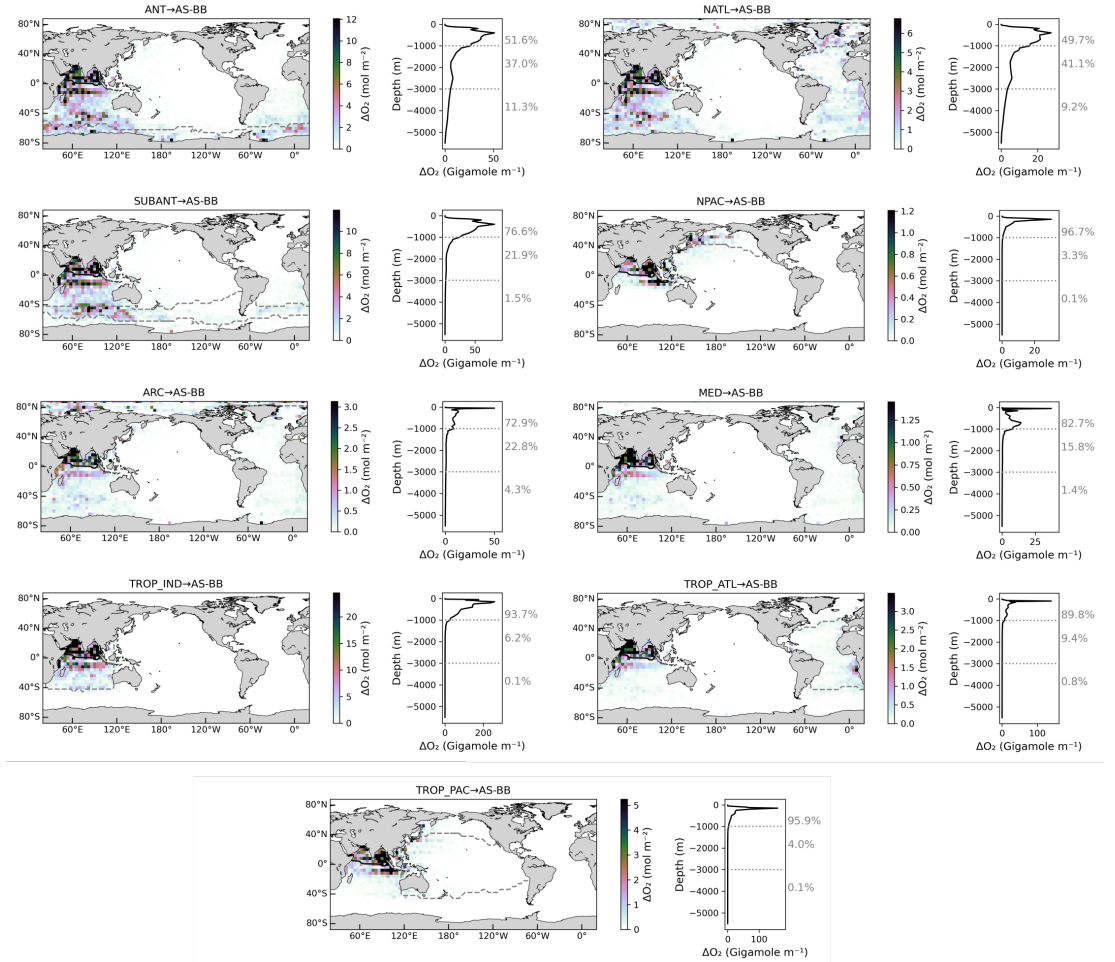


Figure S8. Same as Figure S6 but for Arabian Sea - Bay of Bengal (AS-BB) Oxygen Minimum Zone.

Bibliography

- Anderson, L. A., and J. L. Sarmiento (1994), Redfield ratios of remineralization determined by nutrient data analysis, *Global Biogeochemical Cycles*, 8(1), 65–80, doi:<https://doi.org/10.1029/93GB03318>. 13
- Archer, D., H. Kheshgi, and E. Maier-Reimer (1997), Multiple timescales for the neutralization of fossil fuel CO₂, 24, 405–408. 10
- Bach, L. T., S. J. Gill, R. E. M. Rickaby, S. Gore, and P. Renforth (2019), CO₂ Removal With Enhanced Weathering and Ocean Alkalinity Enhancement: Potential Risks and Co-benefits for Marine Pelagic Ecosystems, *Frontiers in Climate*, 1. 30
- Bakker, D. C., B. Pfeil, C. S. Landa, N. Metzl, K. M. O’Brien, A. Olsen, K. Smith, C. Cosca, S. Harasawa, S. D. Jones, S. I. Nakaoka, Y. Nojiri, U. Schuster, T. Steinhoff, C. Sweeney, T. Takahashi, B. Tilbrook, C. Wada, R. Wanninkhof, S. R. Alin, C. F. Balestrini, L. Barbero, N. R. Bates, A. A. Bianchi, F. Bonou, J. Boutin, Y. Bozec, E. F. Burger, W. J. Cai, R. D. Castle, L. Chen, M. Chierici, K. Currie, W. Evans, C. Featherstone, R. A. Feely, A. Fransson, C. Goyet, N. Greenwood, L. Gregor, S. Hankin, N. J. Hardman-Mountford, J. Harlay, J. Hauck, M. Hoppema, M. P. Humphreys, C. W. Hunt, B. Huss, J. S. P. Ibáñez, T. Johannessen, R. Keeling, V. Kitidis, A. Körtzinger, A. Kozyr, E. Krasakopoulou, A. Kuwata, P. Landschützer, S. K. Lauvset, N. Lefèvre, C. Lo Monaco, A. Manke, J. T. Mathis, L. Merlivat, F. J. Millero, P. M. Monteiro, D. R. Munro, A. Murata, T. Newberger, A. M. Omar, T. Ono, K. Paterson, D. Pearce, D. Pierrot, L. L. Robbins, S. Saito, J. Salisbury, R. Schlitzer, B. Schneider, R. Schweitzer, R. Sieger, I. Skjelvan, K. F. Sullivan, S. C. Sutherland, A. J. Sutton, K. Tadokoro, M. Telszewski, M. Tuma, S. M. Van Heuven, D. Vandemark, B. Ward, A. J. Watson, and S. Xu (2016), A multi-decade record of high-quality fCO₂ data in version 3 of the Surface Ocean CO₂ Atlas (SO-CAT), *Earth System Science Data*, 8(2), 383–413, doi:10.5194/essd-8-383-2016. 2, 31
- Berger, M., L. Kwiatkowski, D. T. Ho, and L. Bopp (2023), Ocean dynamics and biological feedbacks limit the potential of macroalgae carbon dioxide removal, *Environmental Research Letters*, 18(2), 024,039, doi:10.1088/1748-9326/acb06e. 30, 31
- Bopp, L., M. Lévy, L. Resplandy, and J. B. Sallée (2015), Pathways of anthropogenic carbon subduction in the global ocean, *Geophysical Research Letters*, 42(15), 6416–6423, doi:10.1002/2015GL065073. 11, 12, 32

- Brakstad, A., K. Våge, L. Håvik, and G. W. MOORE (2019), Water mass transformation in the Greenland sea during the period 1986-2016, *Journal of Physical Oceanography*, *49*(1), 121–140, doi:10.1175/JPO-D-17-0273.1. 20
- Brakstad, A., G. Gebbie, K. Våge, E. Jeansson, and S. R. Ólafsdóttir (2023), Formation and pathways of dense water in the Nordic Seas based on a regional inversion, *Progress in Oceanography*, *212*, 102,981, doi:10.1016/j.pocean.2023.102981. 19, 20, 21, 22, 29
- Broecker, W. S. (1974), "NO", a conservative water-mass tracer, *Earth and Planetary Science Letters*, *23*(1), 100–107, doi:10.1016/0012-821X(74)90036-3. 7
- Broecker, W. S., and T.-H. Peng (1982), *Tracers in the Sea*, Lamont- Doherty Earth Observatory of Columbia University. 6, 13
- Broecker, W. S., T. Takahashi, and T. Takahashi (1985), Sources and flow patterns of deep-ocean waters as deduced from potential temperature, salinity, and initial phosphate concentration, *Journal of Geophysical Research*, *90*, 6925–6939, doi:10.1029/JC090iC04p06925. 7
- Cabré, A., I. Marinov, R. Bernardello, and D. Bianchi (2015), Oxygen minimum zones in the tropical Pacific across CMIP5 models: Mean state differences and climate change trends, *Biogeosciences*, *12*(18), 5429–5454, doi:10.5194/bg-12-5429-2015. 15
- Carter, B. R., R. A. Feely, S. K. Lauvset, A. Olsen, T. DeVries, and R. Sonnerup (2021), Preformed Properties for Marine Organic Matter and Carbonate Mineral Cycling Quantification, *Global Biogeochemical Cycles*, *35*(1), doi:10.1029/2020GB006623. 14
- Chafik, L., and T. Rossby (2019), Volume, Heat, and Freshwater Divergences in the Subpolar North Atlantic Suggest the Nordic Seas as Key to the State of the Meridional Overturning Circulation, *Geophysical Research Letters*, *46*(9), 4799–4808, doi:10.1029/2019GL082110. 30, 31
- De Lavergne, C., J. B. Palter, E. D. Galbraith, R. Bernardello, and I. Marinov (2014), Cessation of deep convection in the open Southern Ocean under anthropogenic climate change, *Nature Climate Change*, *4*(4), 278–282, doi:10.1038/nclimate2132. 1
- Defant, A. (1929), *Stabile Lagerung ozeanischer Wasserkörper und dazugehörige Stromsysteme*, pp. 1–32. 6
- DeVries, T. (2014), The oceanic anthropogenic CO₂ sink: Storage, air-sea fluxes, and transports over the industrial era, *Global Biogeochemical Cycles*, *28*(7), 631–647, doi:10.1002/2013GB004739. 1, 2, 8, 10, 11
- DeVries, T., and M. Holzer (2019), Radiocarbon and Helium Isotope Constraints on Deep Ocean Ventilation and Mantle-³He Sources, *Journal of Geophysical Research: Oceans*, *124*(5), 3036–3057, doi:10.1029/2018JC014716. 17

- DeVries, T., and F. Primeau (2011), Dynamically and observationally constrained estimates of water-mass distributions and ages in the global ocean, *Journal of Physical Oceanography*, *41*(12), 2381–2401, doi:10.1175/JPO-D-10-05011.1. 19
- DeVries, T., C. Deutsch, F. Primeau, B. Chang, and A. Devol (2012), Global rates of water-column denitrification derived from nitrogen gas measurements, *Nature Geoscience*, *4*(August), 547–550, doi:10.1038/ngeo1515, publisher: Nature Publishing Group. 17
- DeVries, T., M. Holzer, and F. Primeau (2017), Recent increase in oceanic carbon uptake driven by weaker upper-ocean overturning, *Nature*, *542*(7640), 215–218, doi:10.1038/nature21068, publisher: Nature Publishing Group. 32
- Doney, S. C., and W. J. Jenkins (1988), The effect of boundary-conditions on tracer estimates of thermocline ventilation rates, *Journal of Marine Research*, *46*, 947–965. 22
- Durack, P. J., P. J. Gleckler, S. G. Purkey, G. C. Johnson, J. M. Lyman, and T. P. Boyer (2018), Ocean warming from the surface to the deep in observations and models, *Oceanography*, *31*(2 Special Issue), 41–51, doi:10.5670/oceanog.2018.227. 1
- England, M. H. (1995), The Age of Water and Ventilation Timescales in a Global Ocean Model, *Journal of Physical Oceanography*, *25*, 2756–2777. 22
- Feely, R. A., C. L. Sabine, R. Schlitzer, J. L. Bullister, S. Mecking, and D. Greeley (2004), Oxygen utilization and organic carbon remineralization in the upper water column of the Pacific Ocean, *Journal of Oceanography*, *60*(1), 45–52, doi:10.1023/B:JOCE.0000038317.01279.aa. 14
- Fransner, F., A. Olsen, M. Årthun, F. Counillon, J. Tjiputra, A. Samuelsen, and N. Keenlyside (2023), Phytoplankton abundance in the Barents Sea is predictable up to five years in advance, *Communications Earth & Environment*, *4*(1), 1–9, doi:10.1038/s43247-023-00791-9. 31
- Friedlingstein, P., M. O’Sullivan, M. W. Jones, R. M. Andrew, L. Gregor, J. Hauck, C. Le Quéré, I. T. Lujckx, A. Olsen, G. P. Peters, W. Peters, J. Pongratz, C. Schwingshackl, S. Sitch, J. G. Canadell, P. Ciais, R. B. Jackson, S. R. Alin, R. Alkama, A. Arneeth, V. K. Arora, N. R. Bates, M. Becker, N. Bellouin, H. C. Bittig, L. Bopp, F. Chevallier, L. P. Chini, M. Cronin, W. Evans, S. Falk, R. A. Feely, T. Gasser, M. Gehlen, T. Gkritzalis, L. Gloege, G. Grassi, N. Gruber, Gürses, I. Harris, M. Hefner, R. A. Houghton, G. C. Hurtt, Y. Iida, T. Ilyina, A. K. Jain, A. Jersild, K. Kadono, E. Kato, D. Kennedy, K. Klein Goldewijk, J. Knauer, J. I. Korsbakken, P. Landschützer, N. Lefèvre, K. Lindsay, J. Liu, Z. Liu, G. Marland, N. Mayot, M. J. McGrath, N. Metzl, N. M. Monacci, D. R. Munro, S.-I. Nakaoka, Y. Niwa, K. O’Brien, T. Ono, P. I. Palmer, N. Pan, D. Pierrot, K. Pocock, B. Poulter, L. Resplandy, E. Robertson, C. Rödenbeck, C. Rodriguez, T. M. Rosan, J. Schwinger, R. Séférian, J. D. Shutler, I. Skjelvan, T. Steinhoff, Q. Sun, A. J. Sutton, C. Sweeney, S. Takao, T. Tanhua, P. P. Tans, X. Tian, H. Tian, B. Tilbrook, H. Tsujino, F. Tubiello, G. R. van der

- Werf, A. P. Walker, R. Wanninkhof, C. Whitehead, A. Willstrand Wranne, R. Wright, W. Yuan, C. Yue, X. Yue, S. Zaehle, J. Zeng, and B. Zheng (2022), Global Carbon Budget 2022, *Earth System Science Data*, 14(11), 4811–4900, doi:10.5194/essd-14-4811-2022. 1, 2, 8
- Fu, W., A. Bardin, and F. Primeau (2018), Tracing ventilation source of tropical pacific oxygen minimum zones with an adjoint global ocean transport model, *Deep-Sea Research Part I: Oceanographic Research Papers*, 139(November 2017), 95–103, doi:10.1016/j.dsr.2018.07.017, publisher: Elsevier Ltd. 16
- Gao, Y., H. Drange, M. Bentsen, and O. M. Johannessen (2005), Tracer-derived transit time of the waters in the eastern Nordic Seas, 57(4), 332, doi:10.3402/tellusb.v57i4.16553. 31
- Gebbie, G. (2012), Tracer transport timescales and the observed Atlantic-Pacific lag in the timing of the Last Termination, *Paleoceanography*, 27(3), 1–14, doi:10.1029/2011PA002273. 31
- Gebbie, G., and P. Huybers (2010), Total Matrix Intercomparison: A Method for Determining the Geometry of Water-Mass Pathways, *Journal of Physical Oceanography*, 40(8), 1710–1728, doi:10.1175/2010jpo4272.1. 7, 20
- Gebbie, G., and P. Huybers (2011), How is the ocean filled ?, *Geophysical Research Letters*, 38(February), 1–5, doi:10.1029/2011GL046769. 8, 24
- Gebbie, G., and P. Huybers (2012), The Mean Age of Ocean Waters Inferred from Radiocarbon Observations: Sensitivity to Surface Sources and Accounting for Mixing Histories, *Journal of Physical Oceanography*, 42(2), 291–305, doi:10.1175/jpo-d-11-043.1. 19, 20, 21, 29
- Gouretski, V., and K. P. Koltermann (2004), WOCE global hydrographic climatology, *Berichte des Bundesamtes fu r Seeschifffahrt und Hydrographie Tech. Rep. 35, digital media*. 20
- Graven, H. D., N. Gruber, R. Key, S. Khatiwala, and X. Giraud (2012), Changing controls on oceanic radiocarbon: New insights on shallow-to-deep ocean exchange and anthropogenic CO₂ uptake, *Journal of Geophysical Research: Oceans*, 117(10), 1–16, doi:10.1029/2012JC008074. 9
- Gray, J. S., R. S. S. Wu, and Y. O. Ying (2002), Effects of hypoxia and organic enrichment on the coastal marine environment, *Marine Ecology Progress Series*, 238, 249–279, doi:10.3354/meps238249. 3, 15
- Gruber, N., J. L. Sarmiento, and T. F. Stocker (1996), An improved method for detecting anthropogenic CO₂ in the oceans, *Global Biogeochemical Cycles*, 10(4), 809–837, doi:10.1029/96GB01608. 10
- Gruber, N., D. Clement, B. R. Carter, R. A. Feely, S. V. Heuven, M. Hoppema, M. Ishii, and R. M. Key (2019), The oceanic sink for anthropogenic CO₂ from 1994 to 2007, *Science*, 363, 1193–1199. 2, 32

- Haine, T. W., and T. M. Hall (2002), A generalized transport theory: Water-mass composition and age, *Journal of Physical Oceanography*, *32*(6), 1932–1946, doi:10.1175/1520-0485(2002)032<1932:AGTTWM>2.0.CO;2. 7
- Hall, T. M., T. W. N. Haine, and D. W. Waugh (2002), Inferring the concentration of anthropogenic carbon in the ocean from tracers, *Global Biogeochemical Cycles*, *16*(4), 78–1–78–15, doi:10.1029/2001gb001835. 11
- Heimbach, P., C. Hill, and R. Giering (2005), An efficient exact adjoint of the parallel MIT General Circulation Model, generated via automatic differentiation, *Future Generation Computer Systems*, *21*(8), 1356–1371, doi:10.1016/j.future.2004.11.010. 31
- Helland-Hansen, B. (1916), Nogen hydrografiske metoder, *Forb. Skand. Naturforsker Møte*, *16*, 357–359. 6
- Helly, J. J., and L. A. Levin (2004), Global distribution of naturally occurring marine hypoxia on continental margins, *Deep Sea Research Part I: Oceanographic Research Papers*, *51*(9), 1159–1168, doi:https://doi.org/10.1016/j.dsr.2004.03.009. 16
- Helm, K. P., N. L. Bindoff, and J. A. Church (2011), Observed decreases in oxygen content of the global ocean, *Geophysical Research Letters*, *38*(23), 1–6, doi:10.1029/2011GL049513. 3
- Henry, W. (1803), Experiments on the quantity of gases absorbed by water, at different temperatures, and under different pressures, (93), 29–274. 12
- Hill, C., V. Bugnion, M. Follows, and J. Marshall (2004), Evaluating carbon sequestration efficiency in an ocean circulation model by adjoint sensitivity analysis, *Journal of Geophysical Research: Oceans*, *109*(C11), doi:10.1029/2002JC001598. 31
- Holzer, M. (2022), The Fate of Oxygen in the Ocean and Its Sensitivity to Local Changes in Biological Production, *Journal of Geophysical Research: Oceans*, *127*(8), doi:10.1029/2022jc018802. 3, 15, 17, 30
- Holzer, M., and T. M. Hall (2000), Transit-time and tracer-age distributions in geophysical flows, *Journal of the Atmospheric Sciences*, *57*(21), 3539–3558, doi:10.1175/1520-0469(2000)057<3539:TTATAD>2.0.CO;2. 11, 21
- IPCC (2021), *Climate Change 2021: The Physical Science Basis. Contribution of Working Group I to the Sixth Assessment Report of the Intergovernmental Panel on Climate Change*, vol. In Press, Cambridge University Press, Cambridge, United Kingdom and New York, NY, USA, doi:10.1017/9781009157896. 1, 30
- Ito, T., M. J. Follows, and E. A. Boyle (2004), Is AOU a good measure of respiration in the oceans?, *Geophysical Research Letters*, *31*(17), 1–4, doi:10.1029/2004GL020900. 13, 14

- Ito, T., A. Nenes, M. S. Johnson, N. Meskhidze, and C. Deutsch (2016), Acceleration of oxygen decline in the tropical Pacific over the past decades by aerosol pollutants, *Nature Geoscience*, *9*(6), 443–447, doi:10.1038/ngeo2717. 3
- Jacobsen, J. (1927), Eine graphische Methode zur Bestimmung des Vermischungskoeffizienten im Meer, *16*, 404–412. 6
- Jeansson, E., A. Olsen, T. Eldevik, I. Skjelvan, A. M. Omar, S. K. Lauvset, J. E. Nilsen, R. G. Bellerby, T. Johannessen, and E. Falck (2011), The Nordic Seas carbon budget: Sources, sinks, and uncertainties, *Global Biogeochemical Cycles*, *25*(4), 1–16, doi:10.1029/2010GB003961. 3
- Jeansson, E., R. Steinfeldt, and T. Tanhua (2021), Water mass ages based on GLODAPv2 data product (NCEI Accession 0226793), *NOAA National Centers for Environmental Information. Dataset.*, doi:10.25921/xp33-q351. 22, 23
- Jeansson, E., T. Tanhua, A. Olsen, W. M. Smethie Jr., B. Rajasakaren, S. R. Ólafsdóttir, and J. Ólafsson (2023), Decadal Changes in Ventilation and Anthropogenic Carbon in the Nordic Seas, *Journal of Geophysical Research: Oceans*, *128*(3), e2022JC019318, doi:10.1029/2022JC019318. 22
- Jenkins, W. J. (1998), Studying subtropical thermocline ventilation and circulation using tritium and ^3He , *Journal of Geophysical Research: Oceans*, *103*(C8), 15,817–15,831, doi:https://doi.org/10.1029/98JC00141. 14
- Jones, D. C., T. Ito, Y. Takano, and W.-C. Hsu (2014), Spatial and seasonal variability of the air-sea equilibration timescale of carbon dioxide, *Global Biogeochemical Cycles*, *28*(11), 1163–1178, doi:10.1002/2014GB004813. 32
- Joos, F., and R. Spahni (2008), Rates of change in natural and anthropogenic radiative forcing over the past 20,000 years, *Proceedings of the National Academy of Sciences*, *105*(5), 1425–1430, doi:10.1073/pnas.0707386105. 1
- Kalvelage, T., G. Lavik, P. Lam, S. Contreras, L. Arteaga, C. R. Löscher, A. Oschlies, A. Paulmier, L. Stramma, and M. M. M. Kuypers (2013), Nitrogen cycling driven by organic matter export in the South Pacific oxygen minimum zone, *Nature Geoscience*, *6*(February), doi:10.1038/ngeo1739, publisher: Nature Publishing Group. 16
- Karstensen, J., and M. Tomczak (1998), Age determination of mixed water masses using CFC and oxygen data, *Journal of Geophysical Research: Oceans*, *103*(C9), 18,599–18,609, doi:10.1029/98JC00889. 7
- Karstensen, J., L. Stramma, and M. Visbeck (2008), Oxygen minimum zones in the eastern tropical Atlantic and Pacific oceans, *Progress in Oceanography*, *77*(4), 331–350, doi:10.1016/j.pocean.2007.05.009. 15
- Keeling, R. F., and H. E. Garcia (2002), The change in oceanic O₂ inventory associated with recent global warming, *Proceedings of the National Academy of Sciences*, *99*(12), 7848–7853, doi:10.1073/pnas.122154899. 15

- Keeling, R. F., A. Körtzinger, and N. Gruber (2010), Ocean deoxygenation in a warming world, *Annual Review of Marine Science*, *2*(1), 199–229, doi:10.1146/annurev.marine.010908.163855. 1, 3, 14, 15
- Keller, D. P., I. Kriest, W. Koeve, and A. Oschlies (2016), Southern Ocean biological impacts on global ocean oxygen, *Geophysical Research Letters*, *43*(12), 6469–6477, doi:10.1002/2016GL069630. 3
- Khatiwala, S. (2007), A computational framework for simulation of biogeochemical tracers in the ocean, *21*(May), 1–14, doi:10.1029/2007GB002923. 7
- Khatiwala, S., M. Visbeck, and M. A. Cane (2005), Accelerated simulation of passive tracers in ocean circulation models, *Ocean Modelling*, *9*(1), 51–69, doi:10.1016/j.ocemod.2004.04.002. 19
- Khatiwala, S., F. Primeau, and T. Hall (2009), Reconstruction of the history of anthropogenic CO₂ concentrations in the ocean, *Nature*, *462*(7271), 346–349, doi:10.1038/nature08526, publisher: Nature Publishing Group. 1, 2, 11
- Khatiwala, S., T. Tanhua, S. Mikaloff Fletcher, M. Gerber, S. C. Doney, H. D. Graven, N. Gruber, G. A. McKinley, A. Murata, A. F. Ríos, and C. L. Sabine (2013), Global ocean storage of anthropogenic carbon, *Biogeosciences*, *10*(4), 2169–2191, doi:10.5194/bg-10-2169-2013. 8, 11
- Koelling, J., D. W. R. Wallace, U. Send, and J. Karstensen (2017), Intense oceanic uptake of oxygen during 2014/2015 winter convection in the Labrador Sea, *Geophysical Research Letters*, *44*(15), 7855–7864, doi:10.1002/2017GL073933. 32
- Lauvset, S. K., R. M. Key, A. Olsen, S. Van Heuven, A. Velo, X. Lin, C. Schirnick, A. Kozyr, T. Tanhua, M. Hoppema, S. Jutterström, R. Steinfeldt, E. Jeansson, M. Ishii, F. F. Perez, T. Suzuki, and S. Watelet (2016), A new global interior ocean mapped climatology: The 1st CE 1st GLODAP version 2, *Earth System Science Data*, *8*(2), 325–340, doi:10.5194/essd-8-325-2016. 2
- Lauvset, S. K., A. Brakstad, K. Våge, A. Olsen, E. Jeansson, and K. A. Mork (2018), Continued warming, salinification and oxygenation of the Greenland Sea gyre, *Tellus A: Dynamic Meteorology and Oceanography*, *70*(1), 1–9, doi:10.1080/16000870.2018.1476434. 30
- Lauvset, S. K., N. Lange, T. Tanhua, H. C. Bittig, A. Olsen, A. Kozyr, S. Alin, M. Álvarez, K. Azetsu-Scott, L. Barbero, S. Becker, P. J. Brown, B. R. Carter, L. C. da Cunha, R. A. Feely, M. Hoppema, M. P. Humphreys, M. Ishii, E. Jeansson, L.-Q. Jiang, S. D. Jones, C. Lo Monaco, A. Murata, J. D. Müller, F. F. Pérez, B. Pfeil, C. Schirnick, R. Steinfeldt, T. Suzuki, B. Tilbrook, A. Ulfsbo, A. Velo, R. J. Woosley, and R. M. Key (2022), GLODAPv2.2022: the latest version of the global interior ocean biogeochemical data product, *Earth System Science Data*, *14*(12), 5543–5572, doi:10.5194/essd-14-5543-2022. 2, 31
- Leffanue, H., and M. Tomczak (2004), Using OMP analysis to observe temporal variability in water mass distribution, *Journal of Marine Systems*, *48*(1), 3–14, doi:10.1016/j.jmarsys.2003.07.004. 7

- Li, G., L. Cheng, J. Zhu, K. E. Trenberth, M. E. Mann, and J. P. Abraham (2020), Increasing ocean stratification over the past half-century, *Nature Climate Change*, *10*(12), 1116–1123, doi:10.1038/s41558-020-00918-2. 1
- Loose, N., and P. Heimbach (2021), Leveraging Uncertainty Quantification to Design Ocean Climate Observing Systems, *Journal of Advances in Modeling Earth Systems*, *13*(4), e2020MS002,386, doi:10.1029/2020MS002386. 32
- Lozier, M. S., F. Li, S. Bacon, F. Bahr, A. S. Bower, S. A. Cunningham, M. F. De Jong, L. De Steur, B. DeYoung, J. Fischer, S. F. Gary, B. J. Greenan, N. P. Holliday, A. Houk, L. Houpert, M. E. Inall, W. E. Johns, H. L. Johnson, C. Johnson, J. Karstensen, G. Koman, I. A. Le Bras, X. Lin, N. Mackay, D. P. Marshall, H. Mercier, M. Oltmanns, R. S. Pickart, A. L. Ramsey, D. Rayner, F. Straneo, V. Thierry, D. J. Torres, R. G. Williams, C. Wilson, J. Yang, I. Yashayaev, and J. Zhao (2019), A sea change in our view of overturning in the subpolar North Atlantic, *Science*, *363*(6426), 516–521, doi:10.1126/science.aau6592. 30
- Luyten, J. R., J. Pedlosky, and H. Stommel (1983), The Ventilated Thermocline, *Journal of Physical Oceanography*, *13*(2), 292–309, doi:10.1175/1520-0485(1983)013<0292:TVT>2.0.CO;2, publisher: American Meteorological Society Place: Boston MA, USA. 16
- MacGilchrist, G. A., H. L. Johnson, C. Lique, and D. P. Marshall (2021), Demons in the North Atlantic: Variability of Deep Ocean Ventilation, *Geophysical Research Letters*, *48*(9), e2020GL092,340, doi:10.1029/2020GL092340. 32
- Maier-Reimer, E., and K. Hasselmann (1987), Transport and storage of co2 in the ocean., *Climate Dynamics*, *2*(2), 63–90, doi:10.1007/BF01054491. 8
- Marnela, M., B. Rudels, K. A. Olsson, L. G. Anderson, E. Jeansson, D. J. Torres, M.-J. Messias, J. H. Swift, and A. J. Watson (2008), Transports of Nordic Seas water masses and excess SF6 through Fram Strait to the Arctic Ocean, *Progress in Oceanography*, *78*(1), 1–11, doi:10.1016/j.pocean.2007.06.004. 31
- Marotzke, J., R. Giering, K. Q. Zhang, D. Stammer, C. Hill, and T. Lee (1999), Construction of the adjoint MIT ocean general circulation model and application to Atlantic heat transport sensitivity, *Journal of Geophysical Research: Oceans*, *104*(C12), 29,529–29,547, doi:10.1029/1999JC900236. 31
- Martin, J. H., G. A. Knauer, D. M. Karl, and W. W. Broenkow (1987), VERTEX: carbon cycling in the north east Pacific, *Deep-Sea Res.*, *34*(2), 267–285. 14
- McKenna, C., B. Berx, and W. E. N. Austin (2016), The decomposition of the Faroe-Shetland Channel water masses using Parametric Optimum Multi-Parameter analysis, *Deep Sea Research Part I: Oceanographic Research Papers*, *107*, 9–21, doi:https://doi.org/10.1016/j.dsr.2015.10.013. 7
- McNeil, B. I., R. J. Matear, R. M. Key, J. L. Bullister, and J. L. Sarmiento (2003), Anthropogenic CO2 uptake by the ocean based on the global chlorofluorocarbon data set, *Science*, *299*(5604), 235–239, doi:10.1126/science.1077429. 1

- Messias, M. J., A. J. Watson, T. Johannessen, K. I. C. Oliver, K. A. Olsson, E. Fogelqvist, J. Olafsson, S. Bacon, J. Balle, N. Bergman, G. Budéus, M. Danielsen, J. C. Gascard, E. Jeansson, S. R. Olafsdottir, K. Simonsen, T. Tanhua, K. Van Scoy, and J. R. Ledwell (2008), The Greenland Sea tracer experiment 19962002: Horizontal mixing and transport of Greenland Sea Intermediate Water, *Progress in Oceanography*, 78(1), 85–105, doi:10.1016/j.pocean.2007.06.005. 31
- Middelburg, J. J., K. Soetaert, and M. Hagens (2020), Ocean Alkalinity, Buffering and Biogeochemical Processes, *Reviews of Geophysics*, 58(3), doi:10.1029/2019RG000681. 9
- Müller, J. D., N. Gruber, B. R. Carter, R. A. Feely, M. Ishii, N. Lange, S. K. Lauvset, A. M. Murata, A. Olsen, F. F. Pérez, C. L. Sabine, T. Tanhua, R. Wanninkhof, and D. Zhu (2023), Decadal Trends in the Oceanic Storage of Anthropogenic Carbon from 1994 to 2014, *ESS Open Archive*, doi:10.22541/essoar.167525217.76035050/v1. 32
- Olsen, A., A. M. Omar, E. Jeansson, L. G. Anderson, and R. G. J. Bellerby (2010), Nordic seas transit time distributions and anthropogenic CO₂, *Journal of Geophysical Research: Oceans*, 115(C5), doi:10.1029/2009JC005488. 22
- Olsen, A., R. M. Key, S. Van Heuven, S. K. Lauvset, A. Velo, X. Lin, C. Schirnick, A. Kozyr, T. Tanhua, M. Hoppema, S. Jutterström, R. Steinfeldt, E. Jeansson, M. Ishii, F. F. Pérez, and T. Suzuki (2016), The global ocean data analysis project version 2 (GLODAPv2) - An internally consistent data product for the world ocean, *Earth System Science Data*, 8(2), 297–323, doi:10.5194/essd-8-297-2016. 22
- Olson, D. B., G. L. Hitchcock, R. A. Fine, and B. A. Warren (1993), Maintenance of the low-oxygen layer in the central Arabian Sea, *Deep-Sea Research Part II*, 40(3), 673–685, doi:10.1016/0967-0645(93)90051-N. 16
- Palter, J. B., and D. S. Trossman (2018), The Sensitivity of Future Ocean Oxygen to Changes in Ocean Circulation, *Global Biogeochemical Cycles*, 32(5), 738–751, doi:10.1002/2017GB005777. 3
- Peacock, S., and M. Maltrud (2006), Transit-Time Distributions in a Global Ocean Model, *Journal of Physical Oceanography*, 36(3), 474 – 495, doi:https://doi.org/10.1175/JPO2860.1. 22
- Primeau, F., and M. Holzer (2006), The Oceans Memory of the Atmosphere : Residence-Time and Ventilation-Rate Distributions of Water Masses, *Journal of Physical Oceanography*, pp. 1439–1456, doi:https://doi.org/10.1175/JPO2919.1. 29
- Primeau, F., M. Holzer, and T. DeVries (2013), Southern Ocean nutrient trapping and the efficiency of the biological pump, *Journal of Geophysical Research: Oceans*, 118, 2547–2564, doi:doi:10.1002/jgrc.20181. 3

- Primeau, F. W. (2005), Characterizing transport between the surface mixed layer and the ocean interior with a forward and adjoint global ocean transport model, *Journal of Physical Oceanography*, 35(4), 545–564, doi:10.1175/JPO2699.1. 7
- Rajasakaren, B., E. Jeansson, A. Olsen, T. Tanhua, T. Johannessen, and W. M. Smethie (2019), Trends in anthropogenic carbon in the Arctic Ocean, *Progress in Oceanography*, 178(May 2018), 102,177, doi:10.1016/j.pocean.2019.102177, publisher: Elsevier. 22
- Redfield, A., B. Ketchum, and F. Richards (1963), The influence of organism on the composition of sea water, 2, 22–77. 6
- Revelle, R., and H. E. Suess (1957), Carbon Dioxide Exchange Between Atmosphere and Ocean and the Question of an Increase of Atmospheric CO₂ during the Past Decades, *Tellus*, 9(1), 18–27, doi:10.3402/tellusa.v9i1.9075, publisher: Taylor & Francis. 9
- Richardson, P. L. (2008), On the history of meridional overturning circulation schematic diagrams, *Progress in Oceanography*, 76(4), 466–486, doi:10.1016/j.pocean.2008.01.005. 6
- Rumford, B. C. (1798), Of the propagation of heat in fluids, *Essays, Political, Economical, and Philosophical*, pp. 199–313. 6
- Sabine, C. L., R. A. Feely, N. Gruber, R. M. Key, K. Lee, J. L. Bullister, R. Wanninkhof, C. S. Wong, D. W. R. Wallace, B. Tilbrook, F. J. Millero, T.-h. Peng, and A. Kozyr (2004), The Oceanic Sink for Anthropogenic CO₂, *Science*, 305(July), 367–372, doi:10.1126/science.1097403. 1, 2, 10
- Sallée, J. B., R. J. Matear, S. R. Rintoul, and A. Lenton (2012), Localized subduction of anthropogenic carbon dioxide in the Southern Hemisphere oceans, *Nature Geoscience*, 5(8), 579–584, doi:10.1038/ngeo1523, publisher: Nature Publishing Group. 32
- Sarmiento, J. L., and N. Gruber (2002), Sinks for anthropogenic carbon, *Physics Today*, 55(8), 30, doi:10.1063/1.1510279. 8
- Sarmiento, J. L., J. C. Orr, and U. Siegenthaler (1992), A perturbation simulation of CO₂ uptake in an ocean general circulation model, *Journal of Geophysical Research*, 97(C3), 3621–3645, doi:10.1029/91JC02849. 1, 9, 32
- Schmidtko, S., L. Stramma, and M. Visbeck (2017), Decline in global oceanic oxygen content during the past five decades, *Nature*, 542(7641), 335–339, doi:10.1038/nature21399, publisher: Nature Publishing Group. 3
- Siegel, D. A., T. Devries, S. C. Doney, and T. Bell (2021), Assessing the sequestration time scales of some ocean-based carbon dioxide reduction strategies OPEN ACCESS Assessing the sequestration time scales of some ocean-based carbon dioxide reduction strategies, *Environmental Research Letters*, 16. 29, 31

- Smethie, W. M. (1987), Nutrient regeneration and denitrification in low oxygen fjords, *Deep Sea Research Part A, Oceanographic Research Papers*, 34(5-6), 983–1006, doi:10.1016/0198-0149(87)90049-5. 3, 15
- Sonnerup, R. E., B. X. Chang, M. J. Warner, and C. W. Mordy (2019), Timescales of ventilation and consumption of oxygen and fixed nitrogen in the eastern tropical South Pacific oxygen deficient zone from transient tracers, *Deep-Sea Research Part I: Oceanographic Research Papers*, 151(July), 103,080, doi:10.1016/j.dsr.2019.103080, publisher: Elsevier Ltd. 14, 16
- Stendardo, I., and N. Gruber (2012), Oxygen trends over five decades in the North Atlantic, *Journal of Geophysical Research: Oceans*, 117(C11), doi:10.1029/2012JC007909. 30
- Stommel, H. (1957), A survey of ocean current theory, *Deep Sea Research*, 4, 149–184. 6
- Stommel, H. (1958), The abyssal circulation, *Deep Sea Research*, 5, 80–82. 6, 7
- Stommel, H. (1979), Determination of water mass properties of water pumped down from the Ekman layer to the geostrophic flow below, *Proceedings of the National Academy of Sciences*, 76(7), 3051–3055, doi:10.1073/pnas.76.7.3051. 32
- Stramma, L., and S. Schmidtko (2021), Tropical deoxygenation sites revisited to investigate oxygen and nutrient trends, *Ocean Science*, 17(3), 833–847, doi:10.5194/os-17-833-2021. 16
- Stramma, L., G. C. Johnson, E. Firing, and S. Schmidtko (2010), Eastern Pacific oxygen minimum zones: Supply paths and multidecadal changes, *Journal of Geophysical Research: Oceans*, 115(9), 1–12, doi:10.1029/2009JC005976. 3, 16
- Stöven, T., and T. Tanhua (2014), Ventilation of the Mediterranean Sea constrained by multiple transient tracer measurements, *Ocean Science*, 10(3), 439–457, doi:10.5194/os-10-439-2014. 22
- Terhaar, J., T. Tanhua, T. Stöven, J. C. Orr, and L. Bopp (2020), Evaluation of databased estimates of anthropogenic carbon in the Arctic Ocean, *Journal of Geophysical Research: Oceans*, pp. 1–29, doi:10.1029/2020jc016124. 22
- Tomczak, M. (1981), A multi-parameter extension of temperature/salinity diagram techniques for the analysis of non-isopycnal mixing, *Progress in Oceanography*, 10(3), 147–171, doi:10.1016/0079-6611(81)90010-0. 6, 7
- Tomczak, M., and D. G. B. Large (1989), Optimum multiparameter analysis of mixing in the thermocline of the eastern Indian Ocean, *Journal of Geophysical Research: Oceans*, 94(C11), 16,141–16,149, doi:10.1029/JC094iC11p16141. 7
- Wallace, D. W. R., and J. R. N. Lazier (1988), Anthropogenic chlorofluoromethanes in newly formed Labrador Sea Water, *Nature*, 332(6159), 61–63, doi:10.1038/332061a0. 22

- Waugh, D. W., T. W. N. Haine, and T. M. Hall (2004), Transport times and anthropogenic carbon in the subpolar North Atlantic Ocean, *Deep-Sea Research Part I: Oceanographic Research Papers*, 51, 1475–1491, doi:10.1016/j.dsr.2004.06.011. 11, 22
- Waugh, D. W., T. M. Hall, B. I. McNeil, R. Key, and R. J. Matear (2006), Anthropogenic CO₂ in the oceans estimated using transit time distributions, *Tellus, Series B: Chemical and Physical Meteorology*, 58(5), 376–389, doi:10.1111/j.1600-0889.2006.00222.x. 2, 11, 22
- Williams, R. G., J. C. Marshall, and M. A. Spall (1995), Does Stommel’s Mixed Layer Demon Work?, *Journal of Physical Oceanography*, 25(12), 3089–3102, doi:10.1175/1520-0485(1995)025<3089:DSMLW>2.0.CO;2. 32
- Wüst, G. (1935), Schichtung und Zirkulation des Atlantischen Ozeans. Die Stratosphäre, *Wissenschaftliche Ergebnisse der Deutschen Atlantischen Expedition auf dem Forschungs- und Vermessungsschiff Meteor 1925/1927*, 6 (first part), 180. 6
- Wüst, G. (1964), The major deep-sea expeditions and research vessels 1873–1960. A contribution to the history of oceanography, *Progress in Oceanography*, 2(C), doi:10.1016/0079-6611(64)90002-3. 5
- Yamaguchi, R., and T. Suga (2019), Trend and Variability in Global Upper-Ocean Stratification Since the 1960s, *Journal of Geophysical Research: Oceans*, 124(12), 8933–8948, doi:https://doi.org/10.1029/2019JC015439. 1
- Zhou, Y., H. Gong, and F. Zhou (2022), Responses of Horizontally Expanding Oceanic Oxygen Minimum Zones to Climate Change Based on Observations, *Geophysical Research Letters*, 49(6), 1–11, doi:10.1029/2022GL097724. 3, 16
- Årthun, M., T. Eldevik, E. Viste, H. Drange, T. Furevik, H. L. Johnson, and N. S. Keenlyside (2017), Skillful prediction of northern climate provided by the ocean, *Nature Communications*, 8(1), 15,875, doi:10.1038/ncomms15875. 31
- Østerhus, S., R. Woodgate, H. Valdimarsson, B. Turrell, L. De Steur, D. Quadfasel, S. M. Olsen, M. Moritz, C. M. Lee, K. M. H. Larsen, S. Jónsson, C. Johnson, K. Jochumsen, B. Hansen, B. Curry, S. Cunningham, and B. Berx (2019), Arctic Mediterranean exchanges: a consistent volume budget and trends in transports from two decades of observations, *Ocean Science*, 15(2), 379–399, doi:10.5194/os-15-379-2019. 30, 31



Graphic design: Communication Division, UIB / Print: Skjipes Kommunikasjon AS



uib.no

ISBN: 9788230841129 (print)
9788230860632 (PDF)